Ph.D. Dissertation

Study on an LED and SU-8 waveguide coupled silicon optrode with enhanced coupling efficiency

LED와 SU-8 광 도파관을 결합한 광 효율을 증가시킨 실리콘 옵트로드에 관한 연구

August 2022

Graduate School
Seoul National University
Electrical & Computer Engineering

Daeho Ryu

Study on an LED and SU-8 waveguide coupled silicon optrode with enhanced coupling efficiency

Supervisor: Prof. Yong-Kweon Kim

Submitting a Ph.D. Dissertation of Engineering

August 2022

Graduate School
Seoul National University
Electrical & Computer Engineering

Daeho Ryu

Confirming the Ph.D. Dissertation written by Daeho Ryu

August 2022

Chair	서종모	(Seal)
Vice-Chair	김용권	(Seal)
Examiner	이종호	(Seal)
Examiner	지창현	(Seal)
Examiner	조일주	(Seal)

Abstract

A laser-optical fiber-coupled optogenetic neurostimulation system is generally chosen for the light delivering method in optogenetics which stimulates photosensitive neurons using light. However, due to the high-power consumption and bulkiness of the laser control system, wireless optogenetics neuromodulation systems have difficulties in equipping laser modules. To achieve the wireless capability of optical stimulation, optrodes with μLEDs (micro light-emitting diode) were reported. One huge drawback of μLEDs is the thermal damage of neuronal cells due to the heat generated by μLEDs.

In this study, an LED and SU-8 waveguide coupled silicon optrode array is presented, which is compatible with a wireless system and avoids heat damage to neuronal cells. The major problem of the suggested scheme is the large beam dispersion angle of LED and the low coupling efficiency of the source and waveguide. To increase the light irradiance at the SU-8 waveguide tip, an LED and polymer waveguide coupled silicon optrode with lenses has been presented.

Since three-dimensional lens MEMS fabrication is very hard to make, two MEMS compatible lenses were employed to focus light in the vertical and lateral directions. The unique polymer lens pattern and cylindrical lens were placed between a conventional LED and SU-8 waveguide to enhance the light coupling efficiency. The roles of cylindrical lens and SU-8 plano-convex lens are light focus on vertical direction and lateral direction, respectively.

Throughout the study, the MEMS silicon optrode fabrication process was stabilized successfully. The SU-8 transmittance degradation issue at the silicon

etching process is defined for the first time, which is caused by ultraviolet light while silicon plasma etching. Optimizing the fabrication step solved the issue effectively. The unique solution of achieving precise alignment of cylindrical lens was also provided. At last, bonding a flexible printed circuit board and a custom three-dimensional housing structure reduced the size of the silicon optrode device.

Power measurement of the light at the optrode tip showed significant improvement of the light coupling efficiency through the suggested lenses. Measured coupling efficiency increased by the cylindrical lens and the SU-8 plano-convex lens were 6.7 dB and 6.6 dB respectively. The theoretical light coupling efficiency enhancement of the cylindrical lens and the SU-8 plano-convex lens were 6.1 dB and 7 dB, respectively. The theoretical calculation of cylindrical lens efficiency was lower than the measurement, due to the assumption that the portion of meridional rays were much less than the portion of skew rays at the SU-8 waveguide. Since LED has wide dispersion angle and the lenses used in the device make the rays precipitously, the above assumption was established.

When 50 mA current was applied to the 470 nm wavelength LED, the light irradiance of 2.7 mW/mm^2 was measured at the SU-8 waveguide tip. The light irradiance above the electrodes has been analyzed using geometrical dispersion equation by MATLAB code. It showed that all locations above the electrodes have light irradiance greater than 0.5 mW/mm^2.

The silicon optrode is consist of 1x4 optrode shank array, and each optrode contains four recording electrodes and one optical waveguide. Recording electrodes were iridium oxide electroplated to lower the impedance and improve the signal to noise ratio. The average impedance dropped from 2.57 MΩ to 43.6 kΩ. The silicon optrode was inserted into transgenic rat hippocampus CA1 and CA2 region. The

recorded neural spikes were synchronized successfully to the optical stimulation. *In-vivo* experiment proved the optogenetics feasibility and wireless compatibility of the suggested LED and SU-8 waveguide coupled silicon optrode.

Keyword : Silicon optrode, Optogenetics, MEMS, LED, SU-8 waveguide, Wireless neural interface
Student Number : 2018-38246

Table of Contents

Table of figures

Table of tables

1. Introduction

1.1. Background

1.1.1. Optogenetics

Studying brain has always been very difficult to understand its function and mechanism, since there are billions of neurons and trillion synapses entangled together to perform complex functionalities [1]. Fortunately, in these days, neuroscientists are now a few steps closer to observe brain functions through optogenetics. Optogenetics, a study of stimulating neurons through light, widens its field rapidly since Karl Deisseroth introduced the concept in 2006 [2], [3]. It utilizes light sensitive proteins called opsins stimulated by specific light wavelength. The optogenetics became so popular that it received "Method of the Year" by Nature Methods in 2010 [4]. Thanks to the optogenetics, many neuroscientists have revealed the brain connection from single neuron to multiple neurons, and various optogenetic stimulation methods has been newly developed.

Several advantages of optogenetics such as stimulation of specific neurons, and multi-function modulation with multi-wavelength light sources provide very unique and powerful tools over the conventional electrical stimulation methods [5]–[7]. These advantages are not provided by any conventional electrical stimulation methods and many neuroscientists use optogenetics more often than the conventional method. Figure 1 shows the concept of multiple wavelength illumination to induce the various functionality of the neuronal cells.

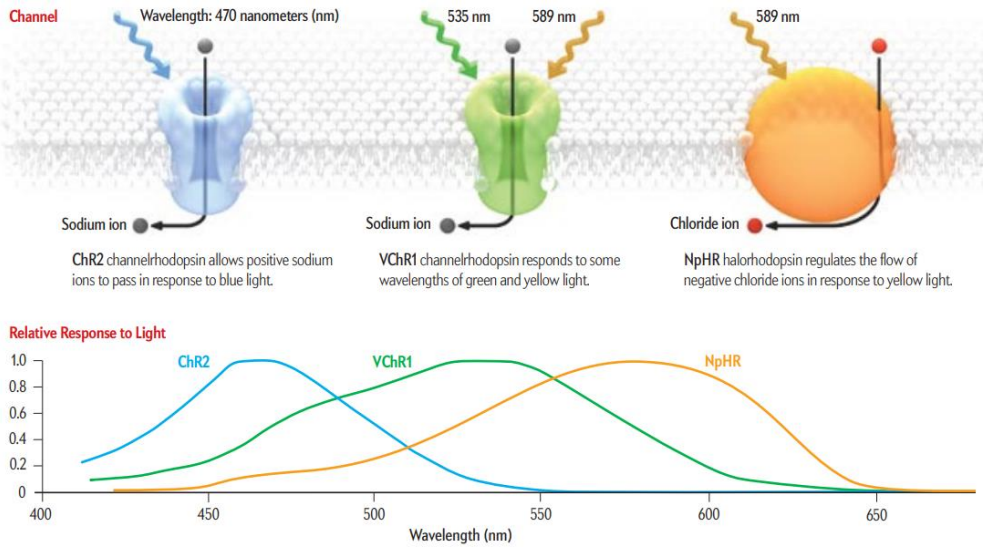

Figure 1. Optogenetic exciting and inhibiting neurons through multi-wavelength illumination [8].

1.1.2. Theory

Optogenetics utilizes special protein called opsins. These opsins respond to light energy and acts as light-gated ion channels. Once opsins are illuminated by light source, the light gates are opened and pass certain ions through. When these ions rapidly move into the cell membrane, the electrical spikes called as action potential are generated, and the signal spreads through the nerve cells like chain reaction. There are many different opsins stimulated by various light wavelength as described in table 1. In general, blue (470 nm) wavelength stimulates the opsin called channelrhodopsin (ChR2) which makes cellular depolarization and conducting H^+, Na^+, K^+, and $Ca2^+$ ions, while yellow (589 nm) wavelength stimulates the opsin called halorhodopsin (NpHR) which makes cellular hyperpolarization and conduction Cl^- ions. Unlike the conventional electrical manipulation of neurons, exciting and inhibiting the function of each nerve cell have

become possible through optogenetics.

Table 1. The common optogenetic proteins for neural activity modulation [9].

Opsin tools	ChR2	NpHR	ReaChR	Chrimson	VChR1	iC1C2
Action	Activator	Inhibitor	Activator	Activator	Activator	Inhibitor
Channel/pump	Cation channel	Chloride pump	Cation channel	Cation channel	Cation channel	Chloride pump
Wavelength (nm)	400-500	550-620	590-630	600	500-550	450-500

Another well-known advantage of optogenetics is capability of cell specific control. Neuroscientists now can investigate the unique function of certain neurons. To place opsins in specific neuron cells, promoters such as synapsin or camKIIα are combined with opsin genes and packaged together in an engineered virus as described in figure 2. Then the virus is delivered to the targeted nerve system by local injection using stereotactic surgery. Within several weeks, opsins are expressed in the neurons to function as light responding ion channels and finally the neurons can be controlled by light. Then, fiber optics and electrodes are implanted to stimulate and monitor the brain activities.

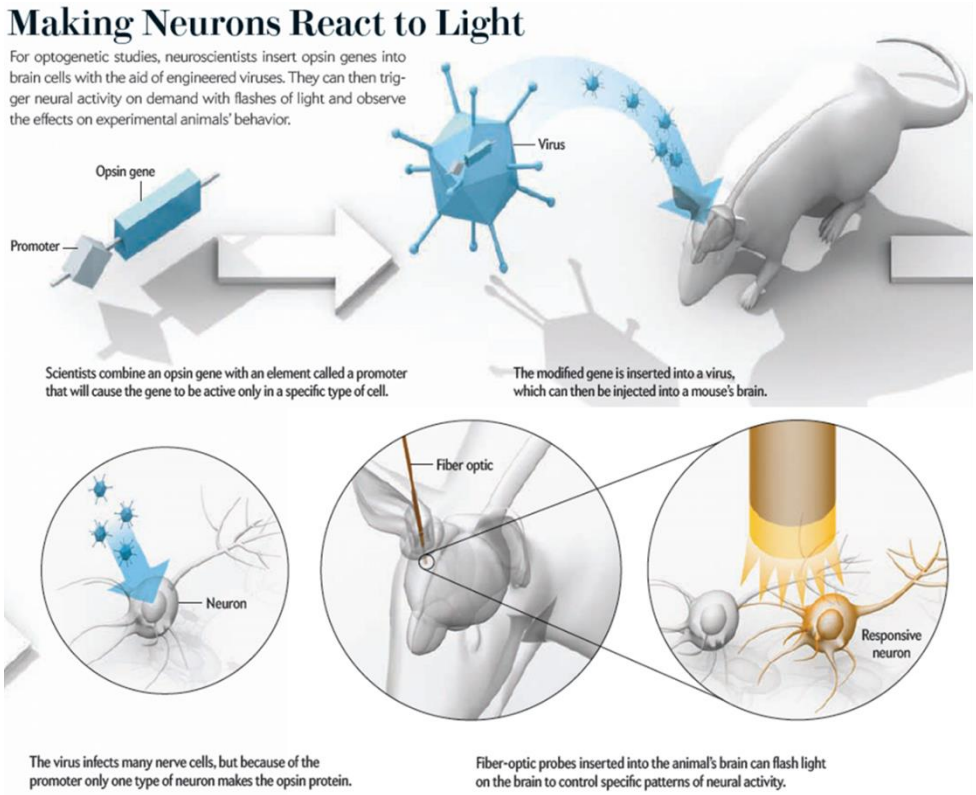

Figure 2. Opsin gene and promoter packaged by engineered virus [8].

1.2. Conventional optogenetics device

1.2.1. Early optogenetics device

In early optogenetics experiments, laser light source coupled optical fibers were used and implanted through stereotactic surgery. Since the minimum irradiance of activating ChR2 expressing neurons is 1 mW/mm^2, the laser source with 470 nm wavelength can achieve this threshold easily [10], [11]. Figure 3 shows an optical fiber inserted into a mice brain at Karl Deisseroth lab, Stanford University. It became a common experiment setup in most optogenetics research and still used until now.

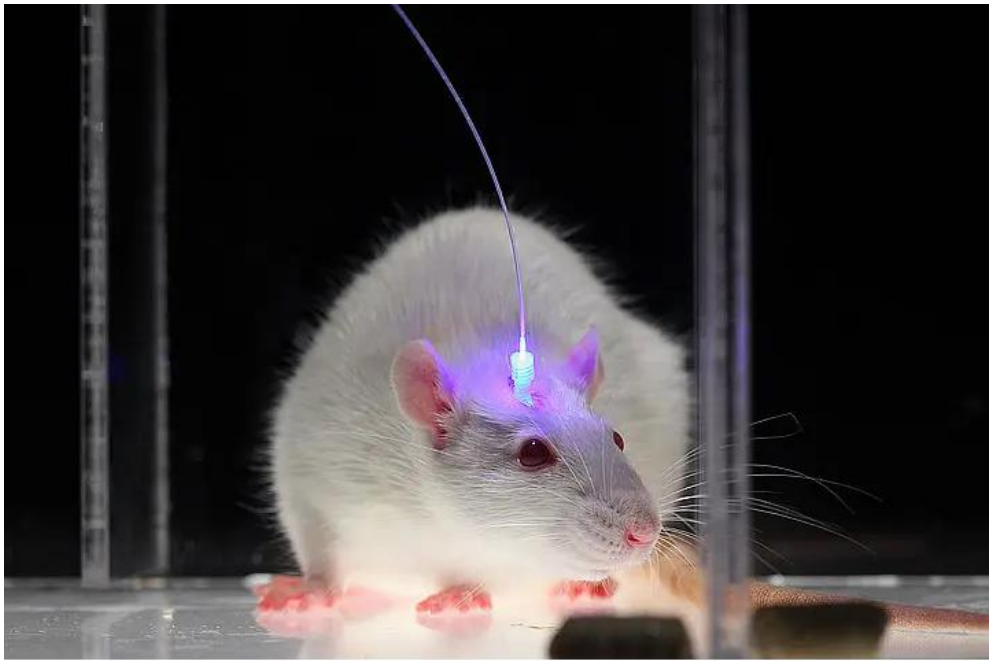

Figure 3. Optogenetics, tested in rodents, can control electrical activity in a few carefully selected neurons [12].

As neuroscientists wanted to explore the roles of brain through optogenetics, they started inserting the fibers into various brain regions such as motor cortex, pre-

frontal cortex, hippocampus etc. For the motor cortex experiment, researchers could observe the behavioral changes of animals within the excitement and inhibition of neurons. However, some regions such as hippocampus couldn't feedback the visible information of how neural circuit works. To read out the neuronal response accurately, electrical wires which sense action potentials were installed together at the vicinity of the optical fibers. Figure 4 shows the schematics of early optrode configuration.

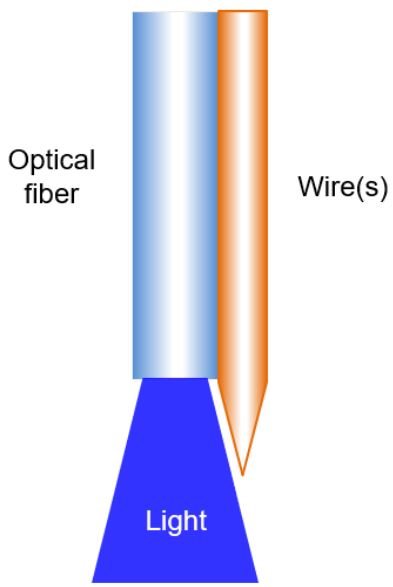

Figure 4. Conventional optrode providing optical stimulation and electrical recording functions.

The early optrode scheme could provide basic functionalities to observe neuronal activities, however, it was not ideal for monitoring dozens of neurons at the same time, because the size expands as the number of recording wires increase. Since neurons are activated as a group, engineers have been focused on integrating dozens of wires in small footprint. The small dimension of optrode can minimize the brain damage while performing stereotaxic surgery. For these reasons, Micro Electro-

Mechanical Systems (MEMS) based silicon optrodes which combines optical waveguide and recording electrodes in small size have been developed.

1.2.2. Laser-based MEMS optrode

Most silicon optrodes use laser light source coupled with various waveguide materials such as SU-8 or silicon oxynitride (SiON) to deliver light to neurons in deep brain region [13]–[26]. The above waveguide materials are MEMS compatible materials. Throughout the MEMS fabrication process, dozens of electrodes can be easily fabricated by metal deposition process within a few microns dimension. MEMS silicon optrodes can provide both optical and electrical properties in small footprints. Figure 5 shows an example of laser-based MEMS silicon optrode from Dr. Euisik Yoon's lab at University of Michigan which successfully delivers 9,400 mW/mm^2 irradiance. The waveguide material is made of SiON and the measured coupling and transmittance loss at the probe tip is -10.5 dB at 473 nm wavelength. The coupling loss is occurred by mismatch of waveguide dimension, and the transmittance loss is affected by the Fresnel reflection and the absorbance of waveguide material. The loss will be discussed more in the later sections to enhance the light delivery efficiency. The silicon probe successfully stimulated and recorded ChR2 expressing neurons with 51 mW/mm^2 irradiance. The author insists that the MEMS silicon optrode can integrate the optics and 8 electrodes monolithically in precision manner to provide the minimal invasion while deep brain stimulation setup and high neuronal density probing functions. The laser-based MEMS silicon optrode demonstrated the capability of optogenetic usage.

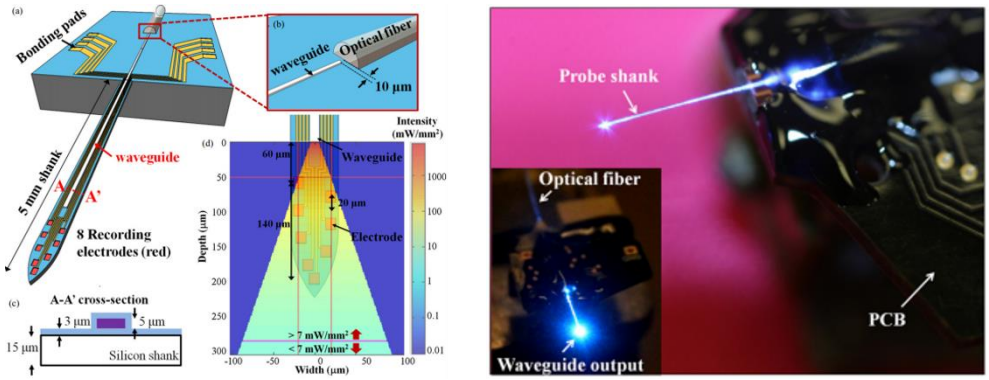

Figure 5. Combination of laser and MEMS silicon optrode [16].

These MEMS device improved the optrode in another level, however, there was another inconvenience that arose in *in-vivo* animal experiment. In this configuration, animals were still tethered to the laser source and their movements were limited. Since laser-based silicon optrode implanted animals were raised one by one per a cage for preventing entanglement of optical fiber, social behavior and interaction research were limited. To overcome the tethering system issue, developing a wireless optogenetics interfaces could be a substitutable option. However, the bulkiness and high-power consumption of laser-light source didn't meet the requirement of wireless specifications. Then, the engineers have come up with different approach of lighting system.

1.2.3. μLED-based MEMS optrode

μLEDs based silicon optrodes which have small dimension and low power consumption are close to the wireless feasibility. Also, tiny light sources could be located at any depth of the silicon optrode and individually turned on. These are huge advantages that the laser-based illumination system couldn't do and many μLEDs based optrodes have been developed [27]–[39]. Figure 6 shows μLEDs based MEMS

silicon optrodes from Dr. Euisik Yoon's lab at University of Michigan. The μLEDs were made up of InGaN which produces 460 nm wavelength light with maximum irradiance of 353 mW/mm^2. The fabricated probe also recorded action potential from in-vivo experiment by stimulating ChR2 proteins.

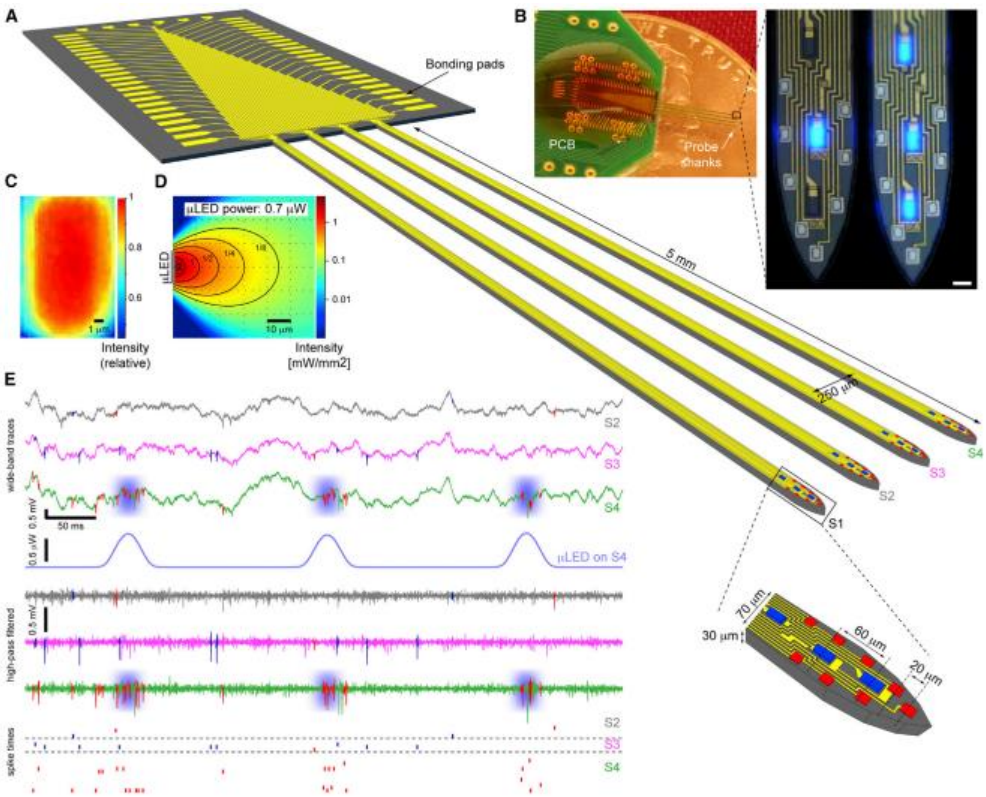

Figure 6. μLED probe drives localized spiking in freely moving mice [30].

Even though, the μLED-based MEMS silicon optrode proved its spatial compactness and low power consumption, the author mentioned that temperature rises due to the μLEDs. The rising temperature can damage the near cells and deteriorates the brain condition. Temperature could reach up to 39.5 °C by increasing the μLED voltage which is very harsh condition to the brain. Figure 7 shows that temperature rises as the applied time goes on. Possible solutions to minimize the heat

can be enhancing the electric to light conversion efficiency of LED, and installing heat sink properly. LED light conversion efficiency plays very critical role of heat generation, and up to 50 % of energy conversion efficiency is attainable at best so far. There have been many efforts to draw the efficiency up, the limit is almost saturated at that level. Also heat sinking design can minimize the heat elevation, however, this can't be the main solution either.

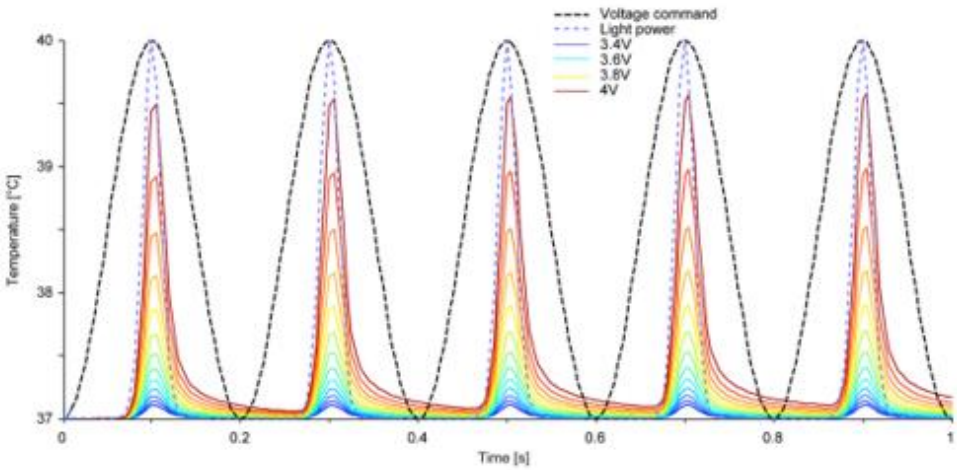

Figure 7. Temperature variation of μLED based silicon optrode [30].

Another issue observed in μLED-based optrode is electrical crosstalk [1]. Measuring action potential which is up to several hundreds of microvolts is very difficult procedure, and any electrical noise that interrupts the signal line easily dominates the signal from neural spikes. To monitor the brain signal successfully, the surrounding environment of *in-vivo* experiment must be maintained extremely clean in terms of electrics. Since μLEDs power rails and the electrode recording lines are laid close to each other, significant noise is induced by the large current that flow into and out of μLEDs.

1.2.4. LED and waveguide coupled optrode

To overcome the issues that are mentioned in laser-based and μLED-based optrodes, LED and waveguide coupled optrodes have been developed [11], [40]–[42]. Using LEDs instead of laser light source can provide compact light providing setup which leads to wireless neural interface feasibility. Also maintaining the waveguide can avoid the heat damage of tissues by light source and EMI crosstalk. Figure 8 shows LED and optical fiber coupled optrode array. LEDs were precisely aligned with optical fibers which is tapered sharply for smooth insertion. The optrode successfully delivered the light and the irradiance was more than 1 mW/mm^2.

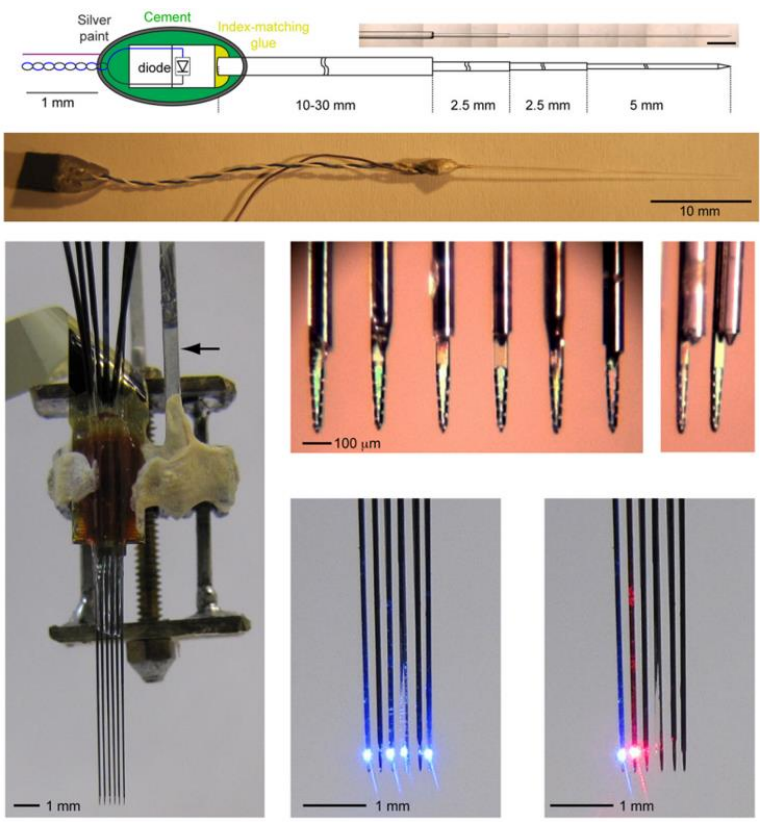

Figure 8. LEDs and optical fiber coupled optrode array [11].

The LED-waveguide optrode system, however, avoided heat damage and EMI crosstalk by indirect illumination system, integrating electrodes in a compact size was difficult. Also, the irradiance at the optical fiber tip is a lot lower than the laser-based system and μLED system. Low coupling efficiency is the severe problem that other LED coupled waveguide goes through due to large size of LED emitters compare to the optical fiber diameter. The LED-waveguide optrode developed by Bernstein et al in MIT draws 500 mA current through the LED, and the heat generated by LED was handled with water cooling pipes around the light source [41]. Eventually, the hole system had to be tethered by the water tubes and the wireless feasibility became uneasy. Figure 9 shows the optrode array developed by MIT.

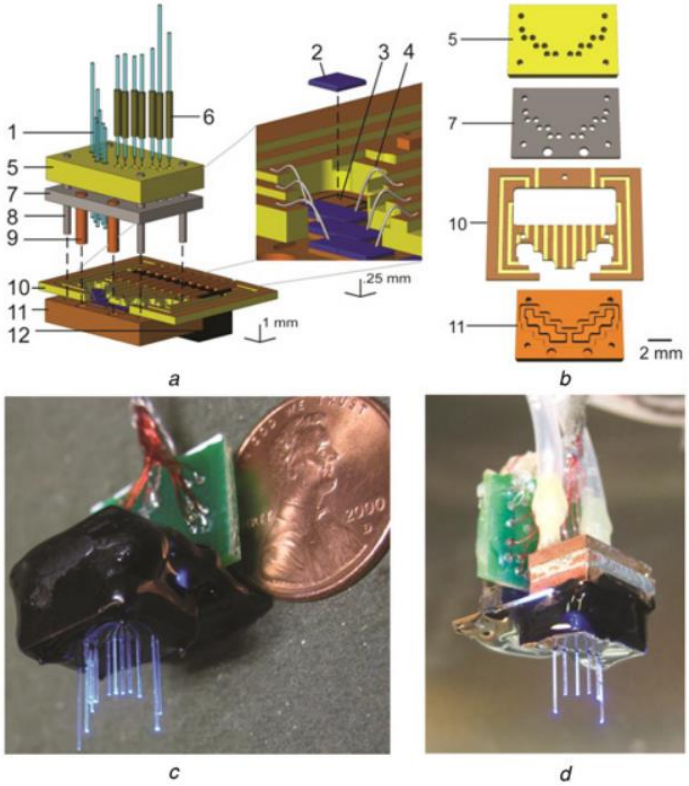

Figure 9. LED and optical fiber coupled optrode with heat sink water pipes developed by MIT media lab [41].

There was an attempt to solve the low irradiance issue of LED-waveguide based optrode system from Seoul National University [43]. Since LED light is wasted due to mismatch of the size of LED and optical fiber diameter, microlens array was applied to enhance the coupling efficiency of the LED and waveguide. By placing microlens array between the LED and waveguide as shown in figure 10, the coupling efficiency was increased by 3.13 dB. Within the same power of LED, higher irradiance could be achieved. Applying microlens showed the improvement of power consumption in wireless neural interfaces. However, integrating electrode in compact size is remained unsolved still.

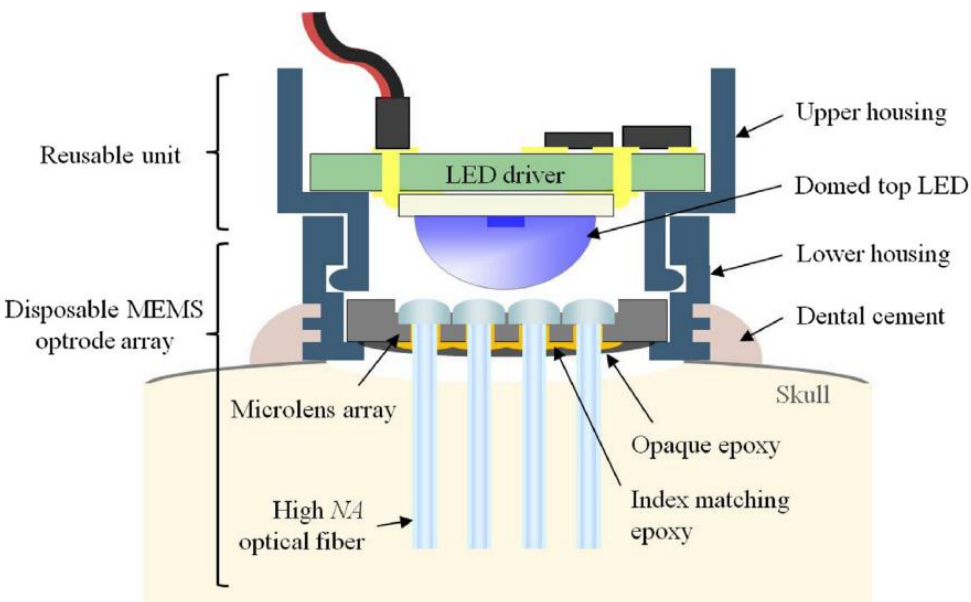

Figure 10. LED and optical fiber coupled optrode array with enhanced coupling efficiency by microlens installation [43].

1.2.5. Summary of conventional methods

By dividing illumination method in conventional optrodes, three categories which are laser-waveguide MEMS optrode, μLED MEMS optrode and LED-

waveguide optrode exist.

The laser-waveguide MEMS optrodes have high irradiance to stimulate the neurons and immune to the EMI crosstalk and heat damage of tissues by light source. However, the laser source is tethered to the light source which keeps animals one by one in the cage. In that reason, research fields such as social behavior and interaction etc. are limited.

μLED based MEMS optrodes also have high irradiance and variable depth specific control is possible. Also, due to the compact size of light source, wireless system feasibility is very high. However, low light energy conversion efficiency generates heat and cause brain tissue damage. Also adding μLEDs to the silicon optrode is very challenging process. The current flows through the μLED power rail generates the EMI crosstalk and deteriorates noise of the recording signal line which decreases the signal to noise ratio.

LED-waveguide optrodes show the wireless feasibility due to the compact light source size, and immune to the heat. However, due to the light source dimension and waveguide inlet facet mismatch, low coupling efficiency induces low irradiance. Even there was a microlens array applied to LED-optical fiber optrode to enhance the light efficiency, the light irradiance barely met the minimum value to stimulate the ChR2 expressing neurons. Also, integrating electrodes in compact size is very challenging process. Table 2 contains the summary of advantages and disadvantages of conventional optogenetics devices. The conventional optogenetics optrodes improved the experiment environment remarkably and provided a lot of conveniences, however, each lighting method goes through its difficulties. In this research, the optrode that avoids issues mentioned above will be discussed.

Table 2. Conventional optogenetics devices summary.

	Laser-waveguide MEMS optrode	μLED MEMS optrode	LED-waveguide optrode
Advantage	• High irradiance • Low EMI • Heat safety	• High irradiance • Variable depth stimulation control • Wireless compatible • Compact size	• Wireless capability • Compact size • Heat safety
Disadvantage	• Wired system (Research limit)	• Heat damage • Hard fabrication • EMI crosstalk	• Low irradiance • Difficult electrode integration

1.3. Research objectives

From the summary of conventional optogenetics devices, the functions demanded by the neuroscientists and how to achieve its function are addressed at the table 3.

Table 3. Neuroscientists' demands and approaches.

Demand	Approaches
● Enough irradiance to stimulate opsins	⇨ Use laser source, μLEDs or adopting lenses
● Multi-channel electrodes recording	⇨ MEMS fabrication process
● Wireless compatibility	⇨ Use LEDs or μLEDs
● Compact size	⇨ MEMS fabrication process
● Heat safety device	⇨ Use waveguide
● Low EMI crosstalk	⇨ Use waveguide

To fabricate the optrode that contains the above functions, LED and waveguide coupled MEMS optrode can meet the requirements except for the enough irradiance to stimulate opsin. However, there was research about coupling efficiency enhancement by adopting microlens which can solve the low irradiance due to the low coupling efficiency of LED and waveguide.

The objective of the research is fabricating an LED and SU-8 waveguide coupled silicon optrode with enhanced coupling efficiency by using MEMS fabrication compatible lenses. The challenging part of making suggested device is how the lens will be fabricated and how much the coupling efficiency can be increased.

Objective of this research:

- Fabricating an LED and SU-8 waveguide coupled silicon optrode with enhanced coupling efficiency by using MEMS fabrication compatible lenses.

Key questions for research approach:

- How the MEMS compatible lens will be made?
- How much coupling efficiency can be increased?

1.4. Research proposal

For the MEMS compatible waveguide materials, SU-8 or SiON waveguides are mostly chosen [15]–[17], [40], [44]. SiON waveguide thickness is limited because stress increases as deposition thickness increases and coupling the light into narrow core is inefficient. On the other hand, SU-8 waveguide thickness is varied by several μm to several hundred μm. Also, the SU-8 fabrication process which is done by single step photolithography process is simpler than deposition and etching of SiON. Any flat lens shape can be easily fabricated by SU-8 photolithography.

SU-8 advantages:

- Simple fabrication process: formed by photolithography
- Easy thickness control from sub microns to several hundreds of microns for light source coupling process

In this study, lenses are employed to increase the light coupling efficiency between an LED and SU-8 waveguide. Since precise three-dimensional lens shape is hard to fabricate in MEMS fabrication process, two two-dimensional lenses, SU-8 lens, and cylindrical lens are installed to focus light on lateral and vertical direction. The SU-8 plano-convex lens focuses light on lateral direction and the cylindrical lens focuses light on vertical direction.

Division of lateral and vertical focusing lenses for MEMS fabrication capability:

- SU-8 plano-convex lens ➔ lateral focus
- Cylindrical lens ➔ vertical focus

There are 4 silicon shanks array with monolithically integrated SU-8 waveguide and 16 recording electrodes. Each shank has 4 electrodes and electroplated with IrOx to lower the impedance. Figure 11 shows the conceptual image of proposed optrode.

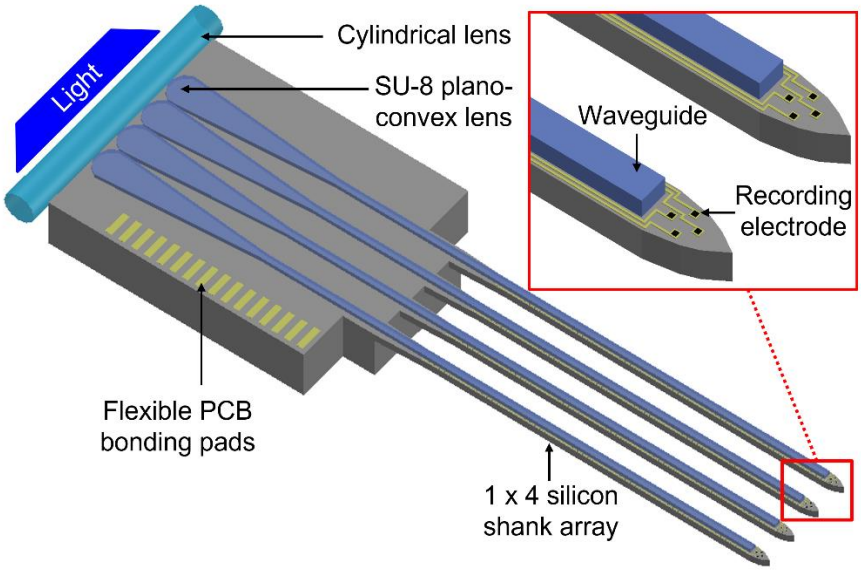

Figure 11. Conceptual image of an LED and SU-8 waveguide coupled MEMS silicon optrode with lenses.

Unlike the conventional PCB (Printed Circuit Board) wire-bonded silicon optrode, the signal lines of recording electrodes will be bonded to flexible PCB for the compact optrode package size. This will provide the convenience of the replacement of used optrode.

Additional feature:

- 16 channel recording electrodes
- FPCB connection

2. Design

2.1. Optical part design

2.1.1. Optical properties

The optical part consists of 470 nm LED, cylindrical lens and SU-8 waveguide as shown in figure 12. The SU-8 waveguide has plano-convex lens shape located nearby cylindrical lens for lateral light focus and the cylindrical lens is proposed for vertical light focus on the SU-8 plano-convex lens. Since the LED light emitting area size is bigger than the coupled area of lenses, light coupling efficiency is very low. To utilize the portion of wasted light from an LED, array of 4 optical waveguides is suggested.

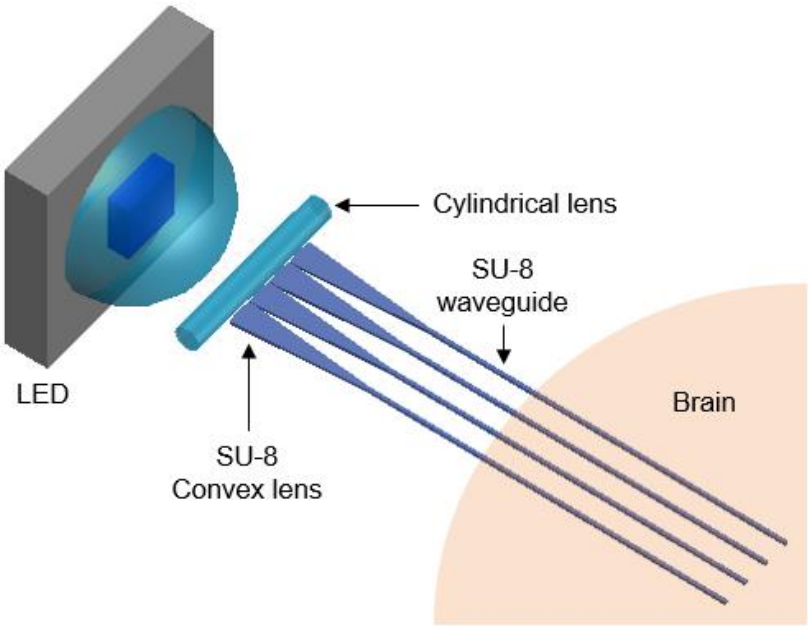

Figure 12. Drawing of optical components of the silicon optrode.

For the optical parts theoretical analysis, the refractive index is important parameter. It can be used for calculating many optical parameters such as reflectance, transmittance, lens focal distance, numerical aperture etc. The refractive index of materials used in this study are listed on the table 4 based on 470 nm wavelength. These values will be used for calculating transmittance and numerical aperture in the next sections.

Table 4. Refractive index of optical components (λ = 470 nm).

Material	Refractive index
Air (n_{air})	1.00
Borosilicate glass ($n_{bk\text{-}7}$)	1.52
SU-8 ($n_{SU\text{-}8}$)	1.61
TEOS oxide (n_{SiOx})	1.55
Brain tissue (n_{tissue})	1.36

2.1.2. Vertical focusing lens design

The cylindrical lens is made of borosilicate glass which refractive index $n_{bk\text{-}7}$ is 1.52 at 470 nm wavelength. The cylindrical lens has 320 μm diameter D and its effective focal length, $EFL_{bk\text{-}7}$, 234 μm is given from the equation 1. The effective focal length is the distance from the principal point to the focal point and is important parameter to match the effective distance between the cylindrical lens and SU-8 waveguide inlet. Figure 13 cross-sectional view shows the vertical light focus into the SU-8 waveguide via cylindrical lens.

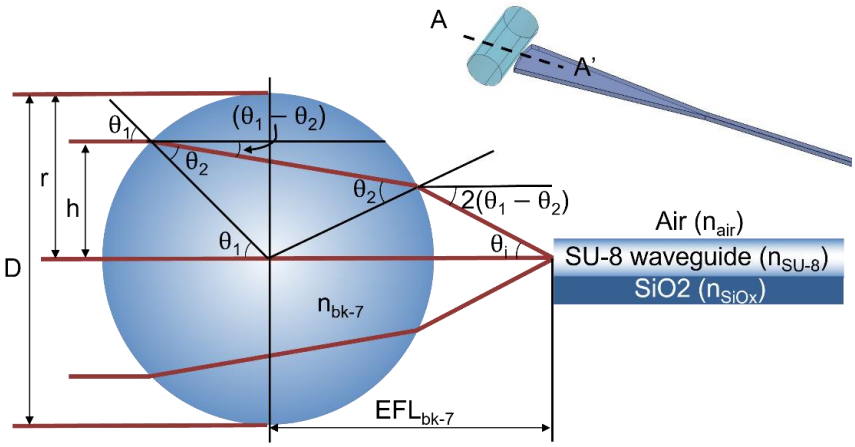

Figure 13. Cylindrical lens light focusing on the SU-8 waveguide in vertical direction.

Supposing the light rays from the light source travel parallel to the waveguide in longitudinal direction, the incident angle and the refracted angle are differed by the height of the cylindrical lens. The incidence angle (θ_1) and the refracted angle (θ_2) are obtained by the equation 2 and Snell's law in equation 3 where h and r are the height and the radius of the cylindrical lens, respectively.

$$EFL = \frac{n_{bk-7} \cdot D}{4(n_{bk-7} - 1)} \quad (1)$$

$$\theta_i = \text{arcsine}\frac{h}{r} \quad (2)$$

$$n_1 \sin\theta_1 = n_2 sin\theta_2 \quad (3)$$

Then the transmittance and reflectance value can be calculated by Fresnel equation. Using the incidents angle and the refracted angle values calculated from equation 2 and 3, the reflectance of s polarization (R_s) and p polarization (R_p) are given by equations 4 and 5. Then the effective reflectance (R_{eff}) is given by equation

6.

$$R_s = \left|\frac{n_1 \cos\theta_1 - n_2 \cos\theta_2}{n_1 \cos\theta_1 + n_2 \cos\theta_2}\right|^2 \quad (4)$$

$$R_p = \left|\frac{n_1 \cos\theta_2 - n_2 \cos\theta_1}{n_1 \cos\theta_2 + n_2 \cos\theta_1}\right|^2 \quad (5)$$

$$R_{eff} = \frac{R_s + R_p}{2} \quad (6)$$

$$T = (1 - R_{eff})^2 \quad (7)$$

Figure 14 shows the transmittance (T) of light passing through the cylindrical lens calculated from equation 7. The transmittance drops quickly when the height and radius ratio exceeds 80% and the cylindrical lens efficiency is lowered. The effective height of the cylindrical lens which depends on the transmittance and the numerical aperture of the SU-8 waveguide must be considered thoroughly. When the SU-8 waveguide cannot accept the rays greater than the total internal reflection angle of the waveguide, the cylindrical lens efficiency decreases. The total internal reflection is determined by the incident angle of the rays lower than the critical angle of waveguide numerical aperture.

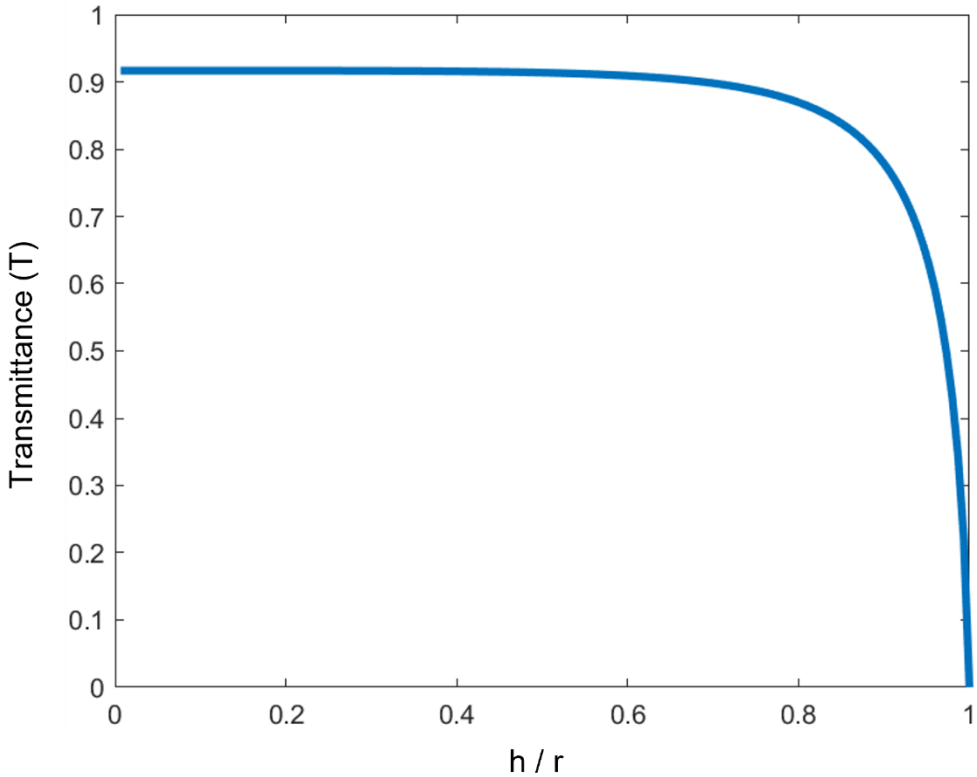

Figure 14. Transmittance of cylindrical lens versus the height and radius ratio.

The effective height of the cylindrical lens is determined by the numerical aperture of the SU-8 waveguide. Since the SU-8 waveguide has TEOS SiO_x cladding layer at the bottom and is surrounded by air at the rest of the surface, skew rays in the SU-8 waveguide escape to the higher refractive index material which is SiO_x rather than to the air. The acceptance angle of the SU-8 waveguide is determined by the refractive index of the SU-8 core and the SiO_x layer, which effectively acts as a bottom cladding layer.

The *NA* of the SU-8 waveguide is 0.435 according to the equation 8 [45], where the refractive index of SU-8 ($n_{SU\text{-}8}$) is 1.61 and the refractive index of SiO_x (n_{SiOx}) is 1.55. Using the equation 9, the acceptance angle (θ_i) of 26° can be obtained at the air and SU-8 interface.

$$NA = (n_{SU-8}{}^2 - n_{SiOx}{}^2)^2 \quad (8)$$

$$A = n_{air} \cdot sin\theta_{air} \quad (9)$$

The acceptance angle of the SU-8 waveguide decides the effective height h_{eff} of the cylindrical lens. Figure 15 shows the *NA* versus *h / r*. From this graph, *NA* of 0.435 gives *h / r* of 0.58. When the cylindrical lens with radius *r* of 160 μm is used, the light rays within the range of the effective height (h_{eff}) of 93 μm are delivered to the SU-8 waveguide outlet.

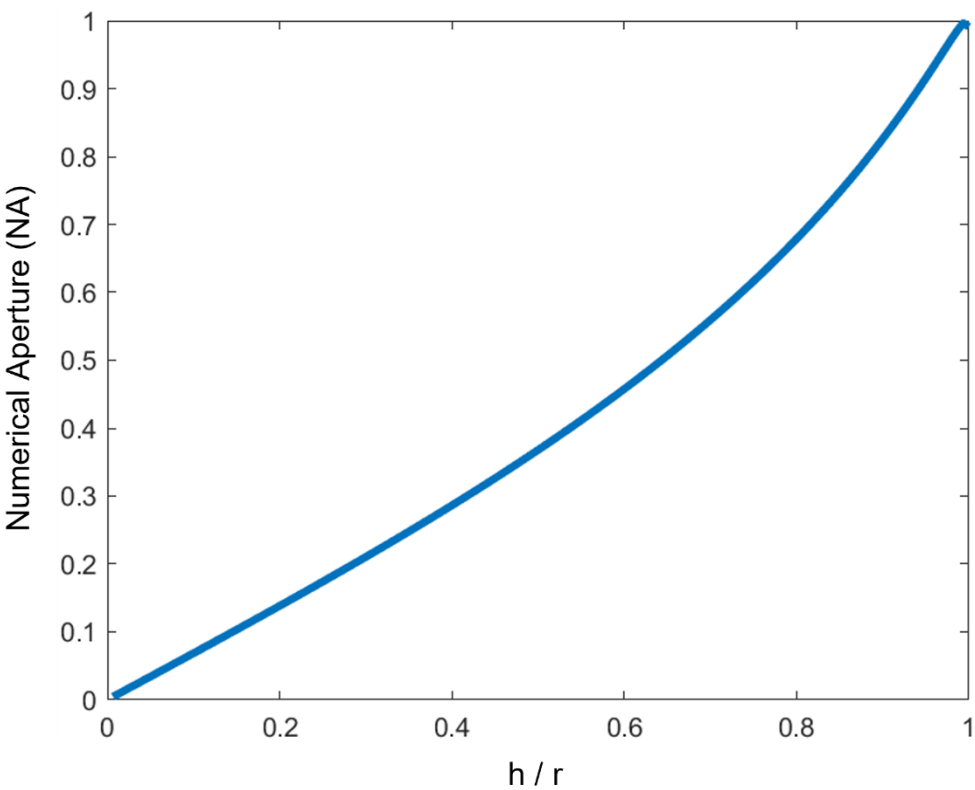

Figure 15. Numerical aperture of cylindrical lens versus the height and radius ratio.

For the SU-8 waveguide height of 40 μm, the cylindrical lens can increase the

light coupling efficiency by 6.7 dB. The transmittance at the air-glass interface is 95.4 %, and the transmittance at the glass-air interface is 91 %. Considering both the transmittance and cylindrical lens efficiency, the total light coupling efficiency enhancement of 6.1 dB can be obtained. The meridional rays with $NA = (n_{SU\text{-}8}^2 - n_{tissue}^2)^{1/2} = 0.87$ will increase the coupling efficiency even though the portion of meridional rays is relatively small compared to the skew rays. The ratio of meridional and skew rays is affected by the LED characteristics, such as beam dispersion angle, incident angle and light emitting area. The reason that the meridional rays are much less than skew rays are because of large LED beam dispersion angle and the cylindrical lens focusing angle. The 6.1 dB light coupling efficiency enhancement of the cylindrical lens is only based on skew rays and the effect of the meridional rays will be considered after the empirical data measurement.

2.1.3. Lateral focusing lens design

For the SU-8 convex lens design, the radius of curvature R = 572.5 μm gives the effective focal length (EFL) at 1500 μm. Within the larger R, the lesser spherical aberration occurs, and figure 16 SU-8 convex lens ray trajectories shows the focusing rays at 1500 μm from the lens entrance facet. The designed lens which has 300 μm width at the light entrance refracts the rays into the final 60 μm width of SU-8 waveguide which increases the coupling efficiency by 7 dB. Figure 17 shows the 2D ray tracing result of the SU-8 convex lens. The designed radius of curvature successfully focused light on the waveguide without any loss with the parallel rays.

The transmittance of the SU-8 waveguide is provided in the other research [46], [47]. According to the reference, -7 dB transmittance is obtained at 11 mm

waveguide length in 470 nm wavelength. Considering the lens efficiency, the expected total coupling efficiency through the SU-8 waveguide is 0 dB.

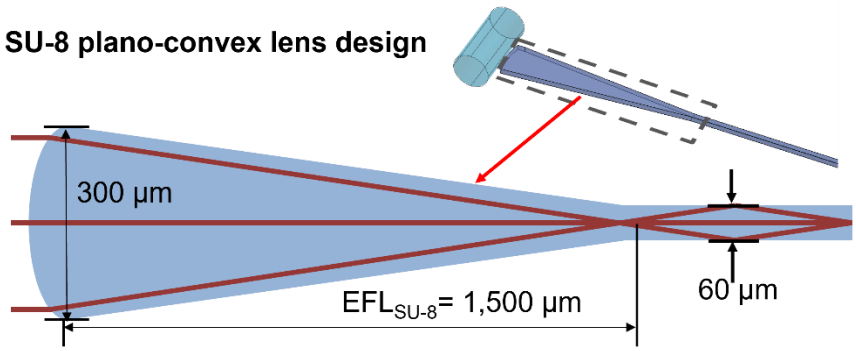

Figure 16. SU-8 convex lens light focusing on the 60 µm width waveguide.

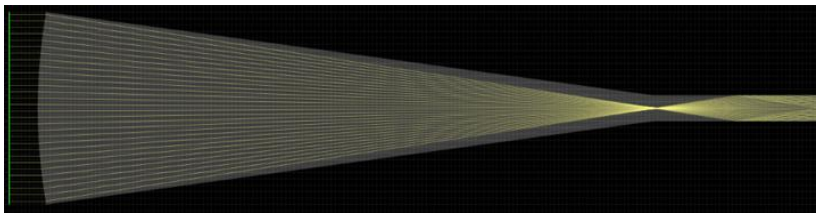

Figure 17. Simulation result of lateral beam focusing using SU-8 convex lens.

To check the cylindrical lens and the SU-8 plano-convex lens validity, COMSOL multiphysics ray tracing simulation has been done. Rays within the effective height of the cylindrical lens are generated and verified the successful light focus on the SU-8 waveguide and delivered the rays at the waveguide outlet as designed. The expected coupling efficiency of the cylindrical lens and SU-8 lens are 6.1 dB and 7 dB, respectively. Figure 18 shows the COMSOL ray trajectories simulation of the designed optical lenses.

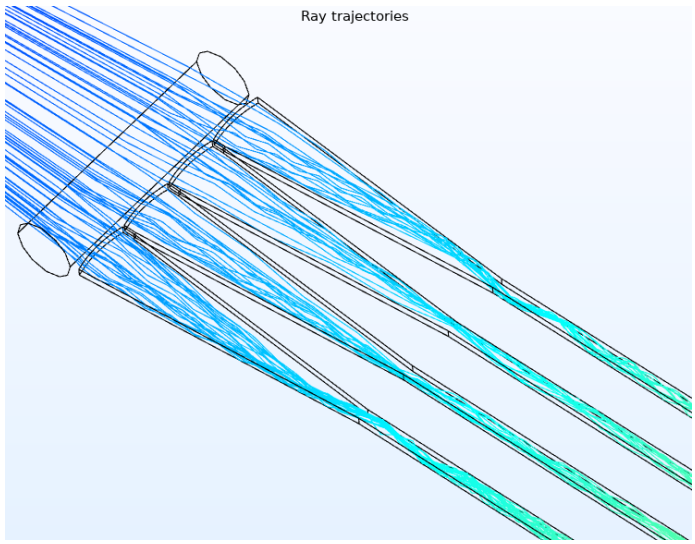

Figure 18. COMSOL ray trajectories result of cylindrical and SU-8 lenses.

2.1.4. LED choice

For the light source, a high-power dome type LED from OSRAM® has been used. Figure 19 shows the image of the LED, and its specifications are listed on the table 5. The blue LED has 470 nm wavelength which is proper to stimulate the ChR2. For the high irradiance at the SU-8 waveguide tip, three categories of LED were considered which are beam dispersion angle, the maximum LED forward current, and luminous flux.

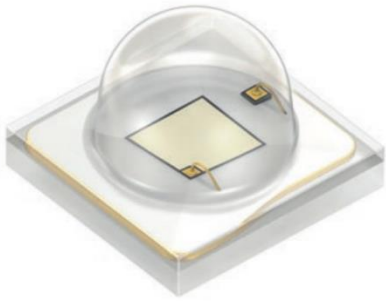

Figure 19. GB QSSPA1.13-HYJX-35-1, dome type 470 nm high power LED.

The beam dispersion angle indicates how much light spreads out as the distance of source gets farther. The lower the beam angle, the higher coupling efficiency can be achieved in the source and waveguide scheme. Among the high power 470 nm wavelength LEDs, GB QSSPA1.13-HYJX-35-1 provides the lowest beam angle. The forward current and luminous flux determines the brightness of the light source and these values showed very similar in the high-power LEDs category. In conclusion, GB QSSPA1.13-HYJX-35-1 dome type 470 nm high power LED is suitable for this research.

Table 5. GB QSSPA1.13-HYJX-35-1 LED specifications.

Product name	GB QSSPA1.13-HYJX-35-1
Wavelength	470 nm
Dispersion angle	80˚
Luminous flux	59 lumens (I_f = 350 mA)
Forward current (Max)	1000 mA
Manufacturer	OSRAM
Size	3 x 3 mm^2

2.1.5. Expected coupling efficiency at the waveguide outlet

Since the optical part selection and design is ready, the source and waveguide maximum coupling efficiency can be calculated by equation 10, where A_{WG} is the cross-sectional area of the waveguide, A_{Source} is the light-emitting area of an LED and c is an empirical correction factor for Fresnel and skew ray compensation [1], [11].

The source-coupled waveguide scheme causes light coupling loss from comparably large LED dimension and small optical fiber cross-sectional area, and a larger beam dispersion angle of LED than that of the laser source is another main cause of light coupling loss. Since the light-emitting area of the LED is Φ2 mm, A_{Source} is 3.14 mm^2, A_{WG} is 0.0096 mm^2, and η_{max} is equal to -36.5 dB. Since the cylindrical lens and the SU-8 plano-convex lens increases the efficiency by 6.1 dB and 7 dB respectively, the coupling efficiency of -23.4 dB is expected.

$$\eta_{max} = \frac{A_{WG} \cdot NA^2}{A_{Source} \cdot {n_{SU-8}}^2} \cdot c \qquad (10)$$

2.2. Silicon shank and body design

2.2.1. Substrate selection

There are various materials are available for the neural probes. Substrates can be classified as inorganic (for example, silicon titanium [48], diamond [49], zinc oxide [50], and silicon carbide [51]) or organic (for example, carbon fiber [52], perylene [53], [54], SU-8 [55], [56], polyimide [57], [58], and silicone [59]) [1]. These materials can be divided by the elastic modulus and the usages are a little different. Figure 20 shows the elastic modulus of often used materials for neuroscience. For the materials, elastic modulus less than 10 GPa are typically used as flexible probes in terms of minimizing brain insertion damage. However, these substrates are too flexible to insert in the deep brain region. When other substrates are deposited onto the low elastic modulus material, device are easily bended. Materials that have elastic modulus greater than 100 GPa has no insertion problem with certain aspect ratio. Typically, silicon probe with high aspect ratio is used for deep brain insertion. Many silicon probes that have about 100 μm width, 5,000 μm length, and 50 μm thickness have been reported deep brain optogenetic stimulation successfully [17], [19], [21], [29]. The silicon material seems reasonable choice for the deep brain stimulation.

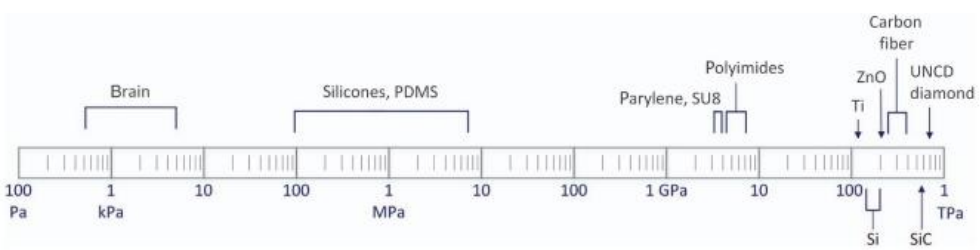

Figure 20. Elastic modulus for many substrates used in implantable arrays [1].

2.2.2. Silicon optrode dimension design

Silicon optrode dimension is very important for optogenetics experiment. Many silicon optrodes have length about several millimeters for rat in-vivo experiment. They are mostly targeting hippocampus, motor cortex, pre-frontal cortex etc. To perform experiment in comprehensive region of rat brain, the designed shank length is about 6,300 μm. The length is longer than other typical silicon optrodes. Since the silicon optrode shanks are brittle structure, the thickness of the shank is designed to be 70 μm, which is thicker than other typical silicon optrodes. Also, the width of the shank is designed to be 100 μm to keep 4 recording electrodes and SU-8 waveguide arranged on the shank. Each recording electrode area is 10 x 10 μm^2, and the signal lines are 4 μm width. Each recording electrode is 40 μm apart from adjacent electrodes.

There are bond pads at the silicon probe body to wire out to the flexible printed circuit board (FPCB). Each FPCB bond pad has 80 x 400 μm^2 area which size is feasible for anisotropic conductive film (ACF) bonding. The bond pad pitch is 200 μm and total 16 bond pads array gives 3,300 μm length. Adding extra space of 1,000 μm gives the silicon body length to 4,300 μm length.

The most vulnerable part of the silicon optrode array is where the shanks and the silicon body meet. Since shanks are easily breakable from the external force, the shank width near the silicon body is 200 μm and decreases its dimension gradually to the tip width which is 100 μm. Figure 21 describes the dimension of suggested optrode.

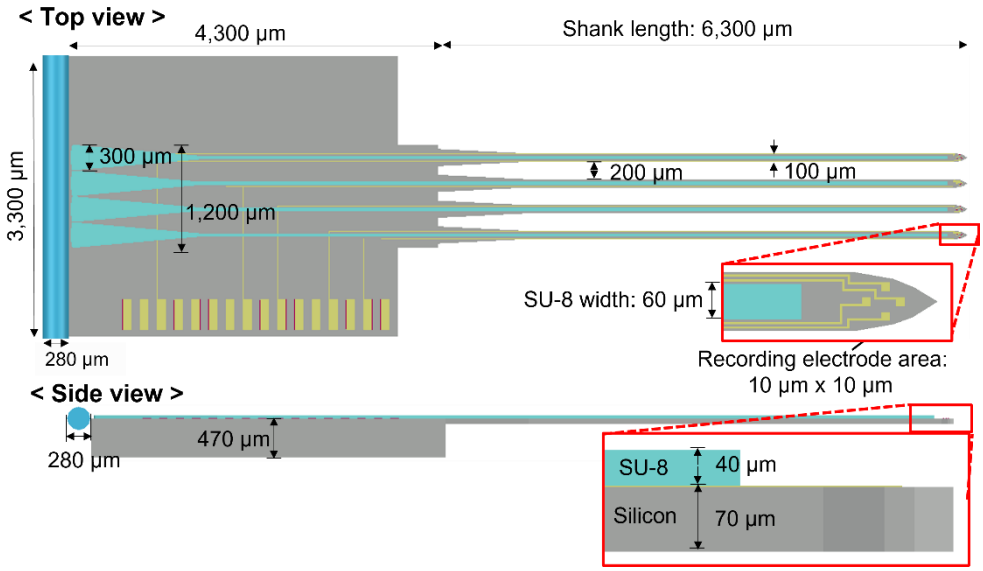

Figure 21. Silicon shanks, body, and optical part dimension.

3. Device fabrication

3.1. MEMS silicon optrode fabrication process

3.1.1. Substrate preparation and insulation layer deposition

Figure 22 describes the MEMS fabrication process. Silicon optrode fabrication process is based on a silicon on insulator (SOI) wafer with 70 μm device layer, 1 μm buried oxide, and 400 μm handling layer. The buried oxide layer performs as etch stop layer in the later silicon etch process which provides the uniform thickness of the silicon shanks. The device layer with low resistivity (< 0.005 Ω·cm) is used for light induced artifact reduction [60]. The 400 μm handling layer thickness enables the short etch time of silicon optrode and offers rigid mechanical body. 15 minutes sulfuric peroxide mix (SPM) clean process removes any organic material on the SOI wafer.

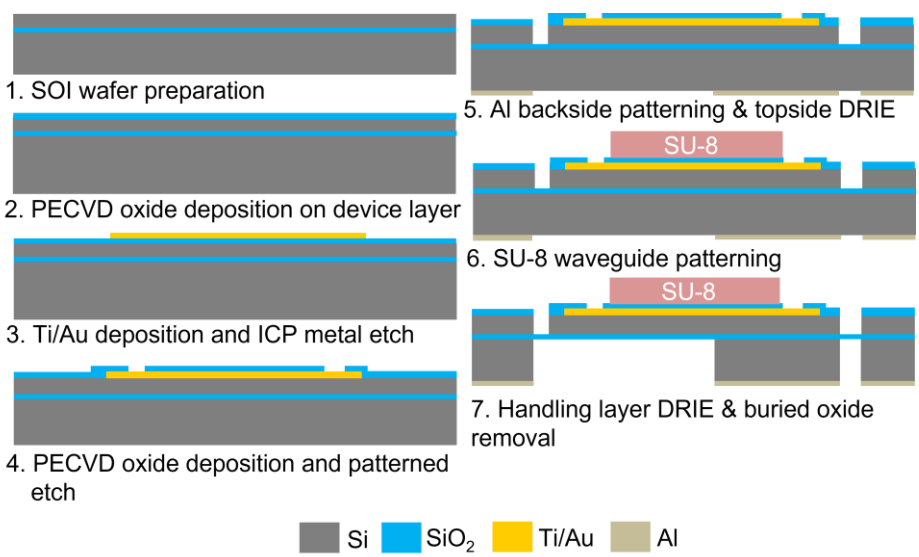

Figure 22. Fabrication process of silicon optrode.

Deposition of 300 nm thickness oxide using plasma enhanced chemical vapor deposition (PECVD) forms insulation layer of electrodes on the device layer. The instrument used to perform PECVD is PlasmaPro System100 from Oxford instruments. The oxide deposition recipe is offered by ISRC (Inter-university Semiconductor Research Center), and the deposition rate is 67 nm/s. There are two deposition rate options 67 nm/s and 300 nm/s. The slower deposition rate provides the denser material characteristics. For the 300 nm oxide deposition, process running time is 4.5 minutes. The 300 nm oxide layer deposition separates the electrical connection from the device layer and the gold layer from the next stage. Figure 23 shows the image of substrate after oxide insulator deposition.

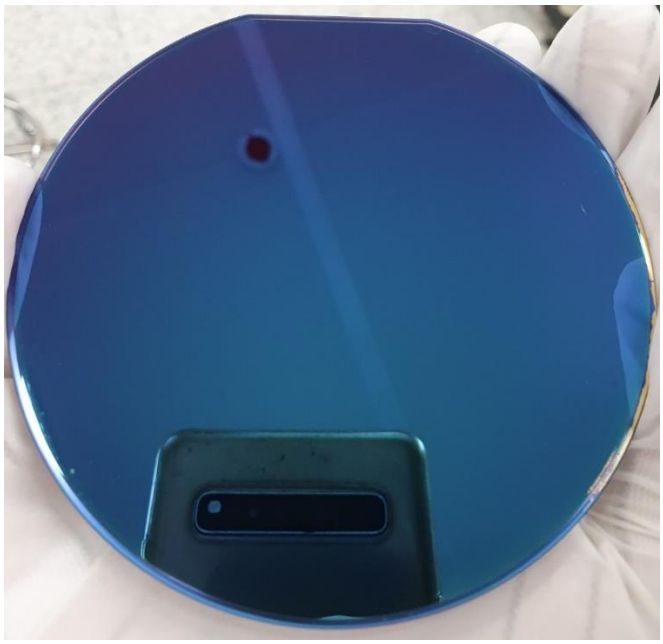

Figure 23. After 300 nm oxide insulator deposition.

3.1.2. Gold electrode patterning

15 nm thickness titanium and 250 nm thickness gold layers (Ti/Au) are

deposited using Maestech electron-gun evaporator and figure 24 shows the image after gold deposition. 15 nm titanium layer is very important not only for adhesion of gold metal but also piranha solution etch resistivity at later fabrication stage. If the thickness is smaller than 15 nm, the adhesion property of gold and titanium is not sufficient, and if the thickness is thicker than 15 nm, the piranha solution can easily invade into the titanium. When the titanium meets the piranha solution, it is etched away, and gold electrode patterns above the titanium are lost.

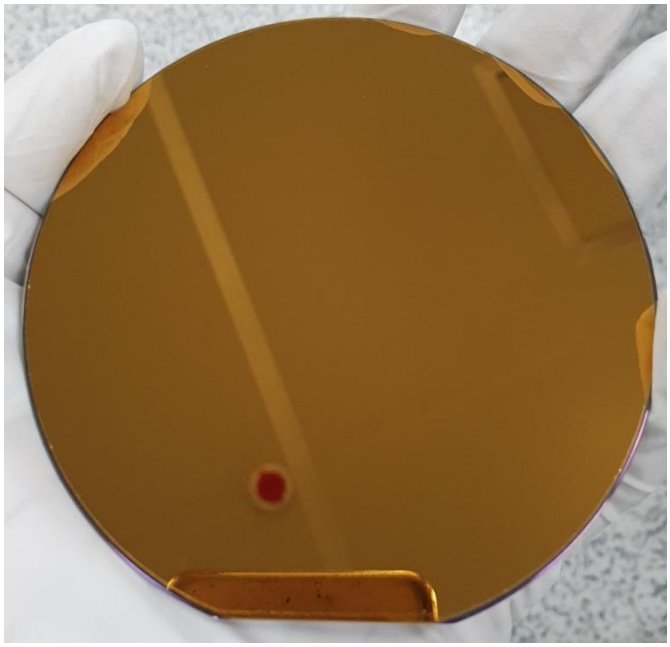

Figure 24. Ti/Au deposition using e-gun evaporator.

For the metal etch mask, 4.5 μm thickness AZ4330 positive photoresist (AZ4330, Microchemicals GmbH, Germany) is patterned. Since the etch selectivity of gold and photoresist is very low, the thickness of photoresist gets thinner and damaged significantly after the inductive coupled plasma (ICP) etch process. When the photoresist layer gets severely damaged, it is hard to remove the resist by piranha

solution, and possible pattern loss can occur. AZ4330 photoresist with 4.5 μm thickness recipe provides the safe fabrication process of 250 nm gold and 15 nm titanium layer. The detailed photolithography process is described in Table 6.

Table 6. AZ4330 photolithography recipe, 4.5 μm thickness

Parameter	Value
Spin coating	4000 RPM – 40 s
Soft bake	110 ℃ – 60 s
Exposure	400 mJ/cm^2
Develop	AZ300 – 210 s

Usually, the easy method of patterning metal layer is using lift-off process since it provides simple fabrication that does not require etch process. The acetone ultrasonication process is a lot easier process. However, the lift-off process is not appropriate for the metal patterning process for silicon optrode fabrication, because of the non-uniform thickness of metal sidewall edge crown. The edge crown disrupts the uniform insulation layer of oxide at the later deposition process. This can cause exposing the metal lines at unwanted area.

Next, the ICP dry etch (PlasmaPro System100 Cobra, Oxford instruments) is carried out to eliminate the metal layer. Chloride gas (Cl_2) are used to perform the etch process. Then, photoresist layer is hardened and become hard to remove. There are three choices to remove the plasma hardened photoresist: O_2 plasma, PR stripper, and piranha (SPM) cleaning. Because the O_2 plasma can generate the unwanted composition of metal oxide layer, and PR stripper takes long time to process, the best option to eliminate the photoresist is using SPM clean process. The SPM clean time

should be minimized after metal deposition, since titanium is etched by the SPM solution. This makes the metal pattern loss. However, up to 3 minutes cleaning process is allowed without losing metal lines. Figure 25 shows the gold electrode after etch process.

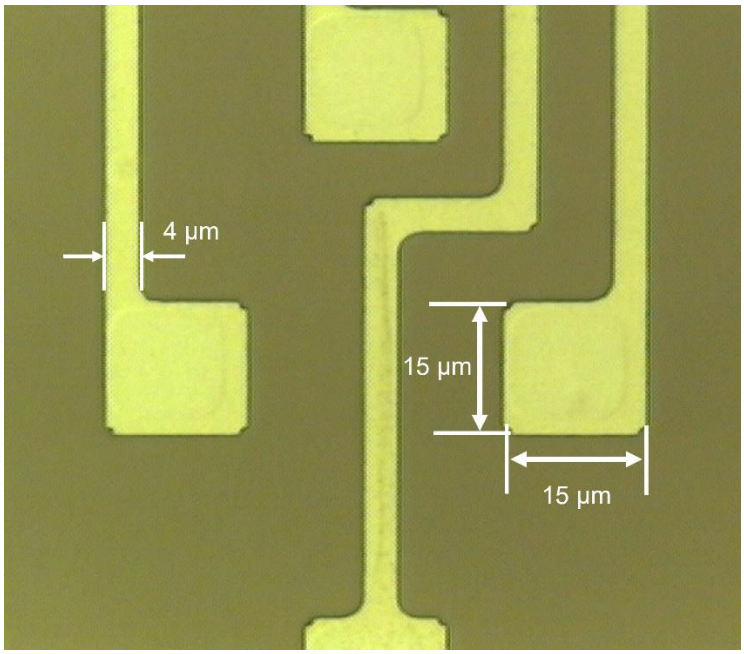

Figure 25. Image of recording electrodes on silicon shank tip.

3.1.3. 2nd insulation deposition and etch

To insulate the metal line, 700 nm thickness oxide using PECVD for is carried out. The insulation layer deposition step is the same process as described in 1st oxide deposition section except the thickness. The 700 nm thick oxide is important parameter to cover all the device layer of SOI waver, even there is thickness difference caused by 250 nm thick metal layer. Then, DNR L300-40 (DONGJIN SEMICHEM Co., Ltd., South Korea) 6.5 μm thickness negative photoresist layer is patterned above the insulation layer. Table 7 contains the detailed recipe to form the

resist pattern.

Table 7. DNR L300-40 negative photoresist recipe, 6.5 µm thickness.

Parameter	Value
Spin coating (HMDS)	2500 RPM – 7 s
Spin coating (PR)	2000 RPM – 40 s
Soft bake	90 °C – 90 s
Exposure	186 mJ/cm^2
Post exposure bake	110 °C – 90 s
Develop	AZ300 – 60 s

To etch the insulation layer, there are two options which are dry etch and wet etch. Usually, dry etch keeps the clean etch profile of the sidewall, and preferred most cases, however it can attack the metal surface and etch the metal layer too. Also, photoresist hardening due to plasma makes the difficulty of removing the photoresist after etch process. Due to these problems, wet etch of oxide layer is carried out. For the oxide etch material, 6:1 buffered oxide etchant (BOE) is used. The etchant provides the proper etch rate for this application around 30 nm/min and does not attack the DNR L300-40 photoresist. To remove the photoresist after etch process, acetone is used. Figure 26 shows the etched region of oxide above the recording electrode. The recording electrode insulation etch area is 10 x 10 µm^2.

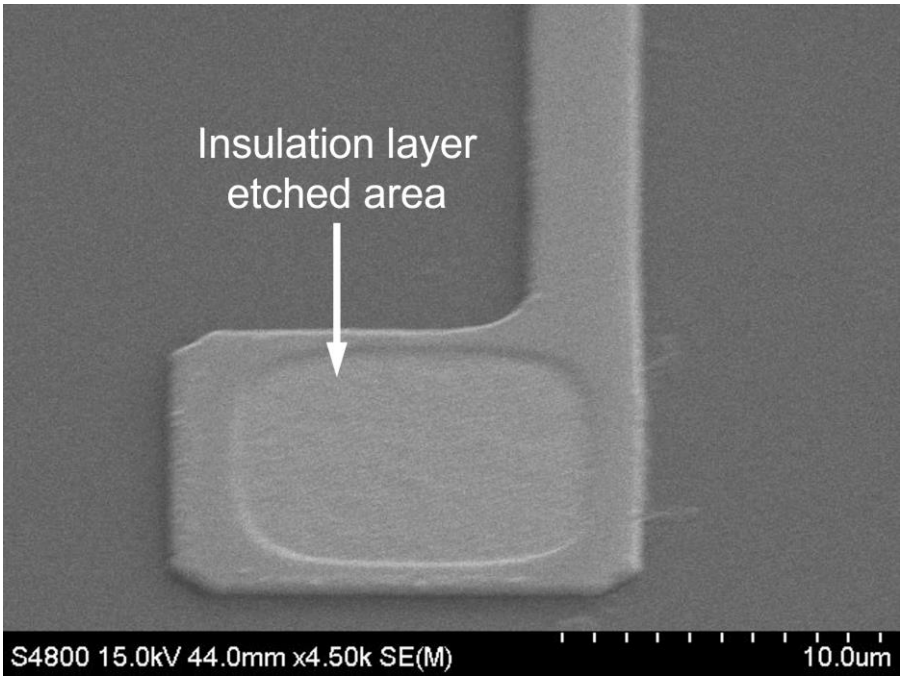

Figure 26. SEM image of etched region above recording electrode metal pattern.

3.1.4. Aluminum pattern on handling layer

On the backside of silicon wafer, AZ5214E 1.4 µm positive photoresist (AZ5214E, Microchemicals GmbH, Germany) is used for 150 nm thickness aluminum (Al) mask layer deposition. Detailed recipe is shown in table 8.

Table 8. AZ5214E positive photoresist 1.4 µm thickness recipe.

Parameter	Value
Spin coating (HMDS)	2500 RPM – 7 s
Spin coating (PR)	4000 RPM – 40 s
Soft bake	95 ℃ – 3 min 30 s
Exposure	120 mJ/cm^2
Develop	AZ300 – 150 s

The aluminum layer is used for silicon deep reactive ion etching (DRIE) hard mask at the probe release fabrication step. Even though etching topside silicon layer is prior to the backside of silicon layer, backside hard mask procedure is earlier than the topside mask layer, because when 40 μm thick SU-8 waveguide is patterned at the topside, it is hard to vacuum the wafer at the later stage. For that reason, backside hard mask formation must be proceeded in this sequence.

To pattern the metal layer, lift-off process is performed. When photolithography is performed on the backside of the wafer, the topside pattern can be scratched. Extra caution is required while handle the wafer. The backside photolithography is carried out using mask aligner (MA6-III, Suss, MicroTec, Germany) with backside alignment (BSA) procedure.

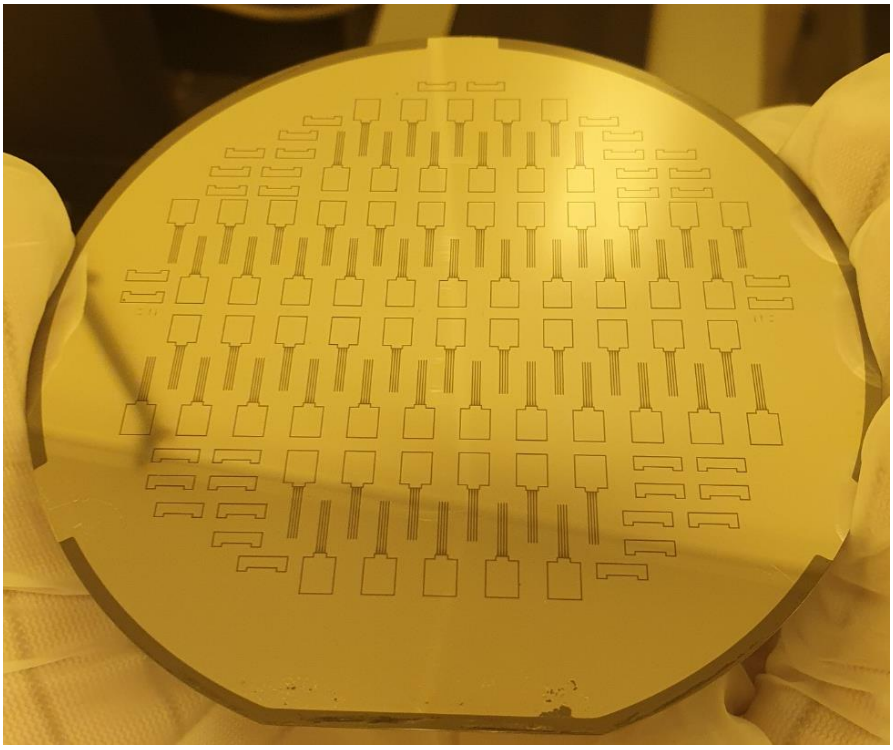

Figure 27. Aluminum hard mask on the handling layer.

After photolithography process, 100 nm thickness aluminum is deposited using thermal evaporator (MHS-1800, Muhan, Korea). The deposition rate of aluminum is kept in 0.5 nm/s for the stable adhesion to the silicon surface. The sonication step needs to be performed carefully to not damage the topside patterns from any micro sized scratch. The sonicated wafer is dipped in acetone tray to remove the unwanted aluminum residue. Figure 27 shows the aluminum hard mask patterned on the handling layer of SOI wafer.

3.1.5. Device layer oxide and silicon etch

Flipping back to the top side, DNR-L300-40 photoresist is patterned for silicon shank etch. 6.5 μm thickness resist mask can endure 1 μm oxide etch and 70 μm silicon etch process. A caution for photolithography step is that developer damages the aluminum on the backside. The oxide etching is processed by plasma etching process (P5000-II, Applied materials, USA). Figure 28 shows topside silicon etch.

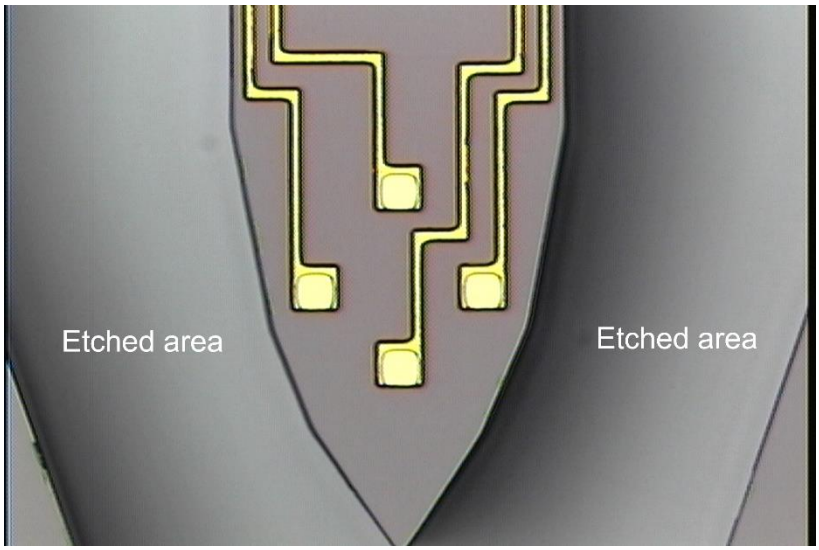

Figure 28. After top side silicon etch process.

3.1.6. SU-8 waveguide fabrication

SU-8 negative photoresist (SU-8 2015, MicroChem, USA) is spin-coated to form 40 µm thickness. Table 9 describes the detailed recipe of SU-8 photoresist.

Table 9. SU-8 photoresist recipe, 40 µm thickness.

Parameter	Value
Spin coating (PR)	800 RPM – 40 s
Soft bake	95 °C – 5 min
Exposure	160 mJ/cm^2
Post exposure bake	95 °C – 6 min
Develop	SU-8 developer – 5 min
Hard bake	200 °C – 10 min

When SU-8 is spin-coated on the wafer, microbubbles are generated. These microbubbles forms void on the pattern which must be avoided. The removing method of microbubbles is poking with sharp material manually. Figure 29 shows microbubbles generated after spin coating process. Generation of microbubbles are due to the uncommon procedure step of the silicon optrode. Usually, resist is spin coated on the flat substrate. However, when high viscosity material is coated on the ununiform thickness surface like this silicon optrode fabrication process, air is trapped and generates bubbles. The reason of reversing silicon trench formation and SU-8 coating process is to keep the transmittance at the best. When silicon DRIE process is performed, ultraviolet (UV) light generated by plasma inside the DRIE chamber severely degrades the SU-8 transparency. The SU-8 transparency

degradation by UV light is well known phenomenon and should be considered thoroughly for optical usage [46], [47].

One useful tip for the SU-8 development process, double dipping of wafer into newly poured developer keeps the clean surface of SU-8 pattern. The hard bake is necessary for reflowing SU-8 photoresist which smooths out the surface of pattern and recovers SU-8 pattern crack due to the stress.

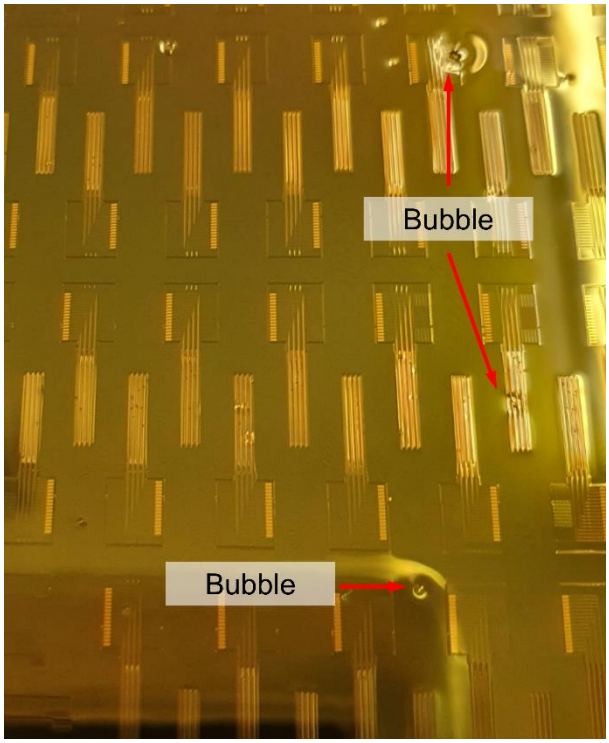

Figure 29. Generated microbubbles after SU-8 spin coating process.

3.1.7. Handling layer silicon etch and buried oxide removal

To separate the silicon optrode from the SOI wafer individually, silicon DRIE process is carried out. This is abnormal process, and usually dicing saw step is used to separate the samples. However, the silicon shanks are too fragile and need to be

handled carefully. Therefore, penetrating silicon wafer using dry etch process is the only option.

There are silicon beams as shown in figure 30 which keeps the device hanging on the wafer. The designed silicon beam width, length, and thickness are 54 µm, 100 µm and 70 µm respectively.

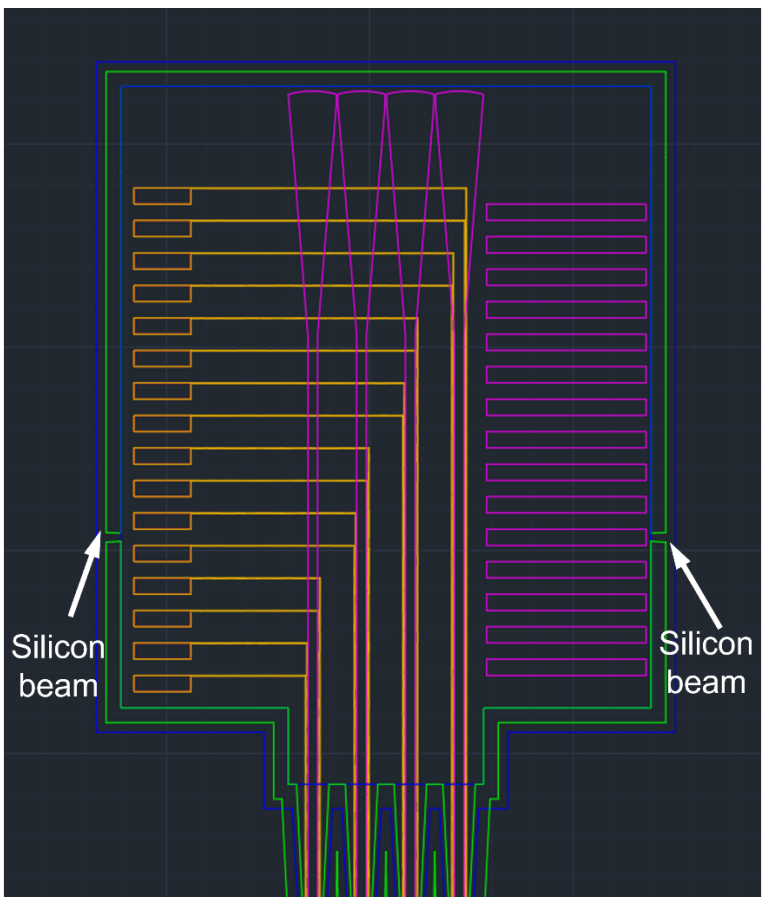

Figure 30. Silicon beams for silicon optrode hanging to the wafer.

At the final stage, backside silicon DRIE process and buried oxide etch are carried out to release the silicon probes. DRIE process is performed using DRIE silicon etcher (SLR-770-10R-B, Plasma Therm). For the 400 µm etch, 2 times of 200 etch loops is done. When the 2nd silicon 200 loop etch is performed, the wafer should

be attached to a dummy wafer. DNR L300-40 photoresist is used to attach the dummy wafer and SOI wafer. The drop of resist is spread shallowly on the edge of the silicon wafer. Then baked at the hot plate to dry the resist.

For the buried oxide removal process, Oxford etcher (PlasmaPro Systems100 Cobra, Oxford instruments, UK) is used. After the step, the MEMS silicon optrode fabrication process is finally done. Figure 31 shows the SEM image of fabrication completed silicon optrode.

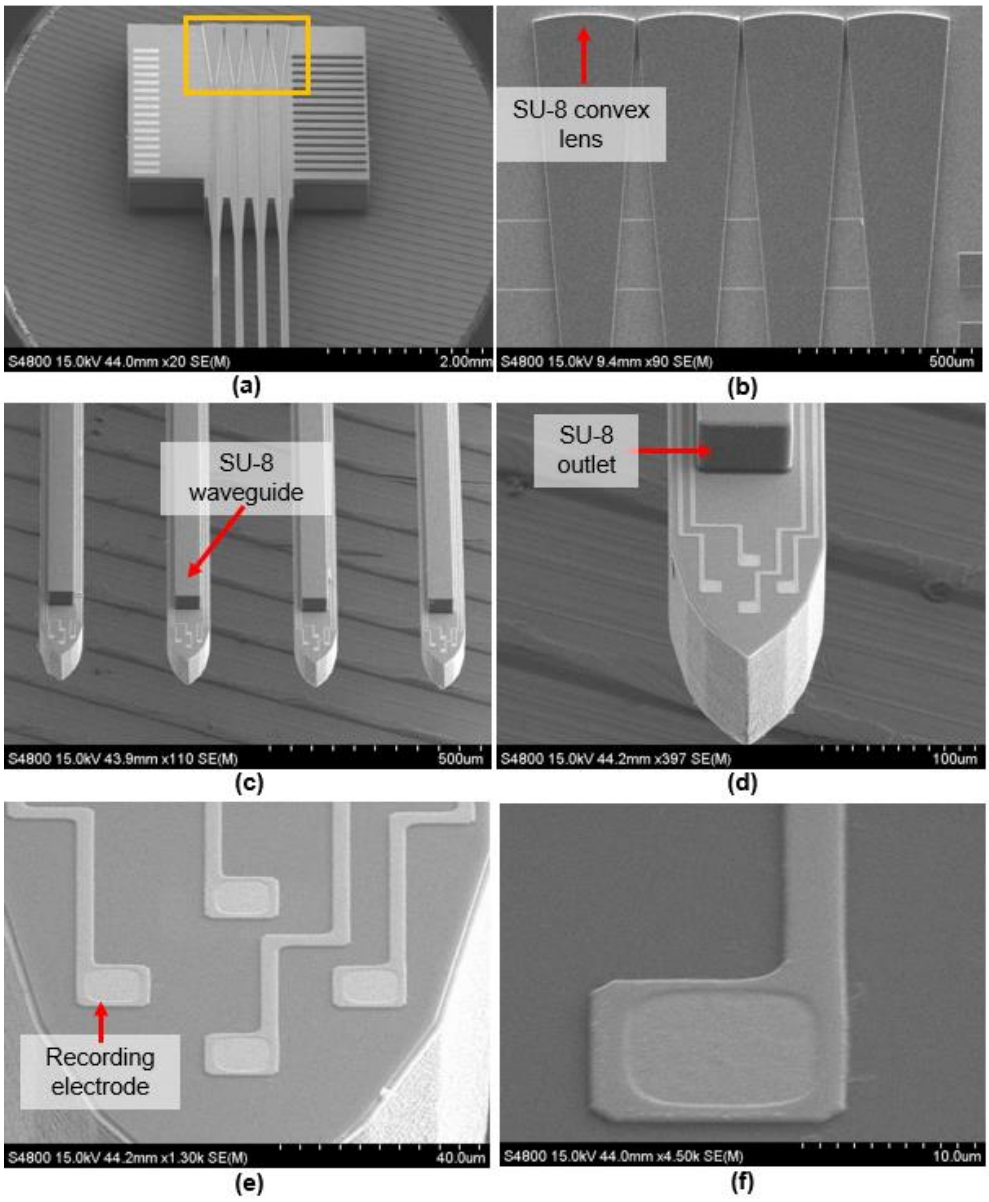

Figure 31. SEM image of fabricated silicon optrode array. (a) Tilted silicon body, (b) SU-8 convex lens shape, (c) 4 silicon shank tip end, (d) single shank tip end showing SU-8 outlet and 4 recording electrodes, I magnified view of recording electrodes, and (f) single electrode image.

3.2. Precision alignment of the cylindrical lens

Cylindrical lens (0.3 mm borosilicate glass rod, Goodfellow, Huntingdon, UK) has diameter deviation which is ±10 %. The difference of the diameter must be handled individually to align the cylindrical lens precisely. In this study, precision aligner of cylindrical lens is proposed. Figure 32 image shows the concept of precise cylindrical lens aligning method.

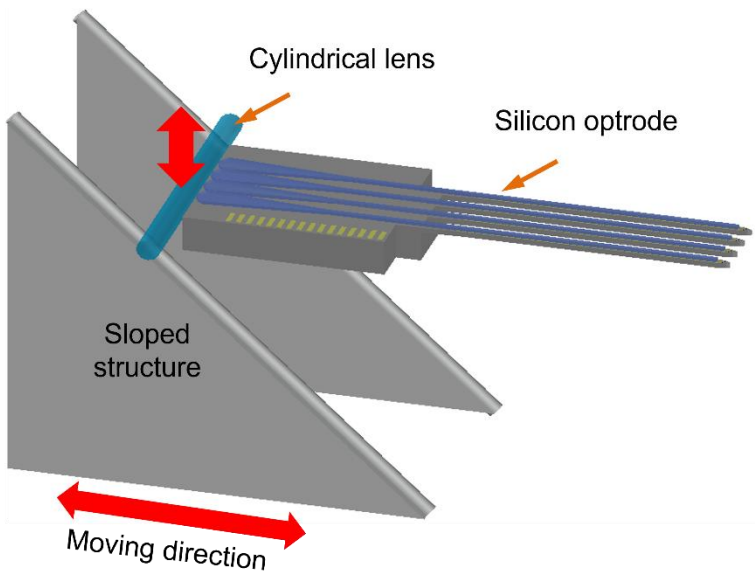

Figure 32. Conceptual image of cylindrical lens precision aligner.

When the sloped structure moves lateral direction, it translates the cylindrical lens movement to vertical direction. By moving sloped structure precisely, the up and down movement is also precise. For the precise movement, M3 hexagonal nuts and bolts were used. Figure 33 image shows the prototype of cylindrical lens precision aligner. The rotational movement makes the sloped bar moves laterally,

and it aligns the cylindrical lens.

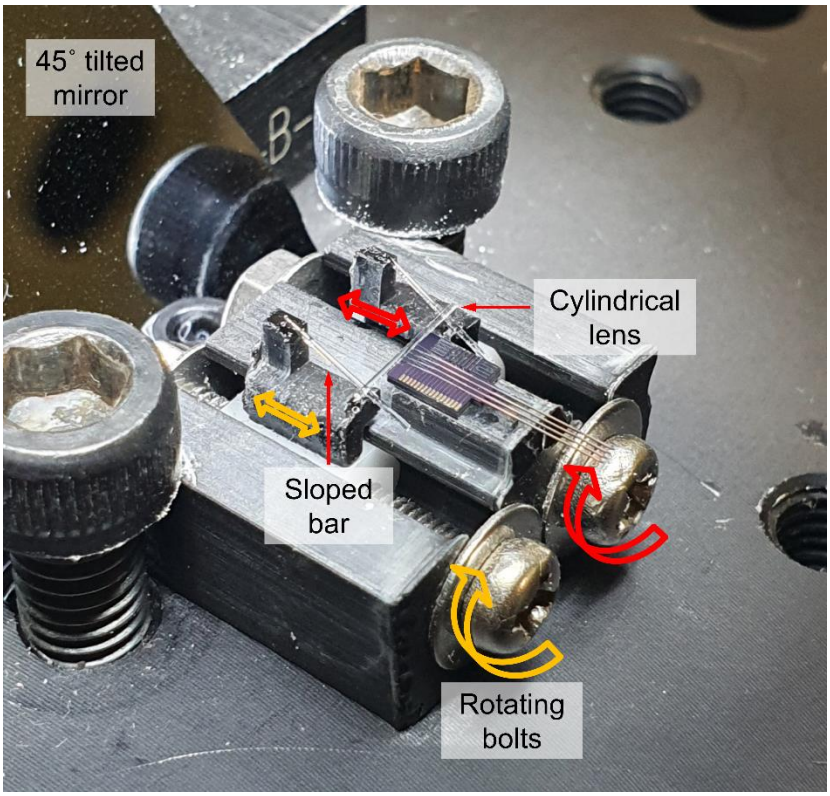

Figure 33. Cylindrical lens precision aligner.

Using 45˚ tilted mirror, SU-8 convex lens light entrance facet is visible through stereo microscope as shown in figure 34 (a). To perform precise alignment, maintaining horizontal placement of optrode is required. When the cylindrical lens is precisely aligned to the silicon optrode, the SU-8 convex lenses entrance facet is magnified as shown in figure 34 (b). In this figure, droplets of the thermally cured epoxy (Water clear epoxy 832WC-A, MG Chemicals, Canada) are shown at the side of silicon optrode which attaches the cylindrical lens to the silicon optrode. The epoxy is hardened in room temperature for 24 hours. Curing at the oven temperature 65 °C which is provided by the epoxy manufacturer instruction is not recommended

because the epoxy viscosity decreases and flows into the gap between cylindrical lens and SU-8 convex lens facet. Also, UV cured epoxy is prohibited for the adhesive material due to the SU-8 transmittance degradation by UV light source.

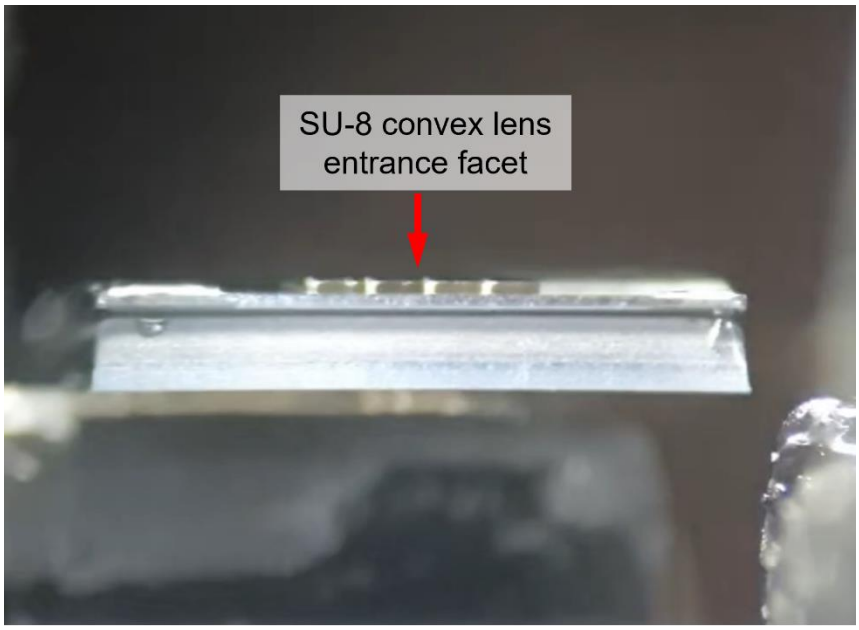

(a)

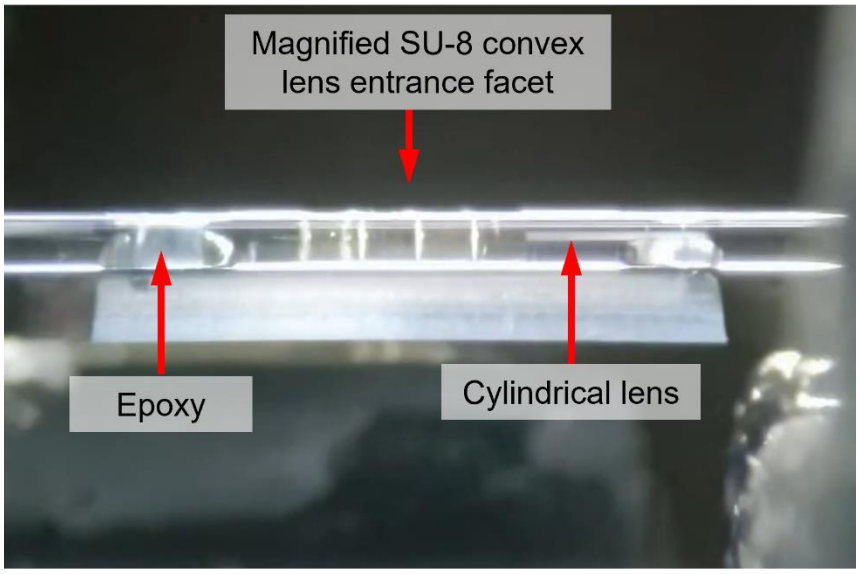

(b)

Figure 34. Cylindrical lens precision alignment (a) before and (b) after.

3.3. Electrical interconnection and impedance improvement

3.3.1. Electrical interconnection

The 16 gold bond pads on the silicon optrode are connected to the flexible PCB using anisotropic conductive film (ACF) bonding. The ACF tape (AC-7206U, Hitachi Chemical Co., Ltd, Japan) is attached to the flexible PCB using hot press bar. After the exact alignment of flexible PCB to the silicon bond pads, 3 MPa pressure, and 190 °C temperature are applied for 10 seconds. Figure 35 shows the image of silicon optrode and FPCB at the ACF bonding stage.

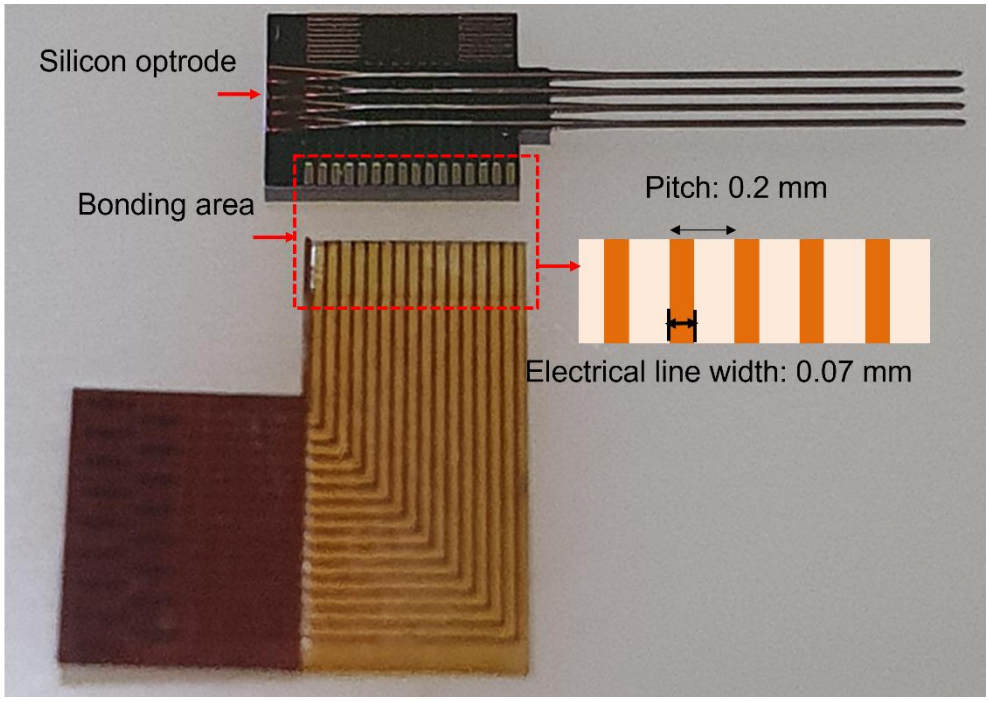

Figure 35. Image of silicon optrode and FPCB for ACF bonding process.

3.3.2. Impedance improvement

To measure the impedance of the recording electrodes, tip of the optrode array is emerged into the phosphate buffered saline (PBS) solution (Life technologies Corp., USA). Electrochemical impedance spectroscopy (EIS) (660E, CH Instrument Inc, South Korea) sweeps the frequency from 100 Hz to 10 kHz and measures the electrode impedance. The average impedance of 10 x 10 μm^2 gold recording electrodes is 2.57 MΩ. Since reducing the impedance increases the signal to noise ratio (SNR), IrOx electroplating is performed with 200 triangular pulses and 1,800 square pulses as shown in figure 36.

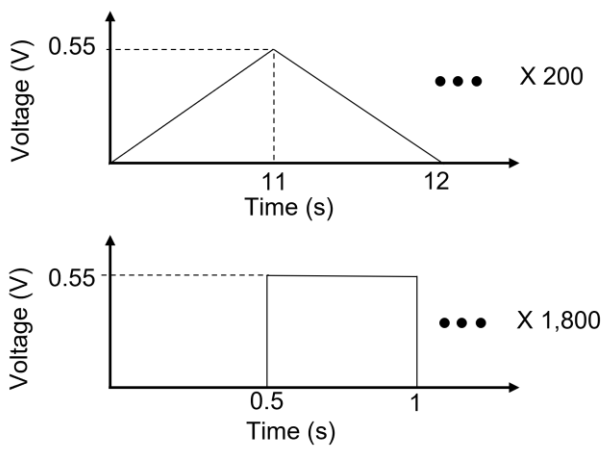

Figure 36. IrOx electroplating parameters of triangular and square pulse.

The Ag/AgCl reference electrode and Pt counter electrode are used and emerged into IrOx electroplating solution. The triangular pulses reduce the impedance, and the rectangular pulses increase the charge storage capacitance [61], [62]. Figure 37 shows the impedance drop after IrOx electroplating and figure 38 shows IrOx electroplated on the gold electrodes. EIS measurement result shows the IrOx electroplating reduces the average impedance to 43.6 kΩ.

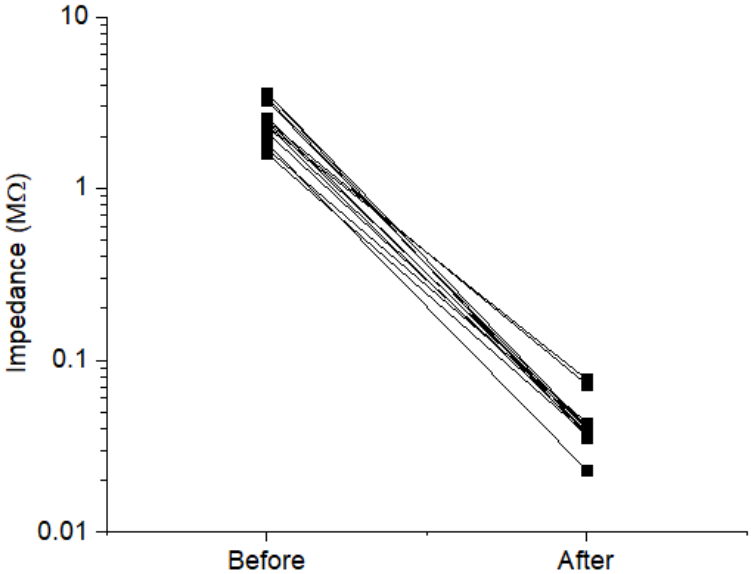

Figure 37. Impedance drop after IrOx electroplating process.

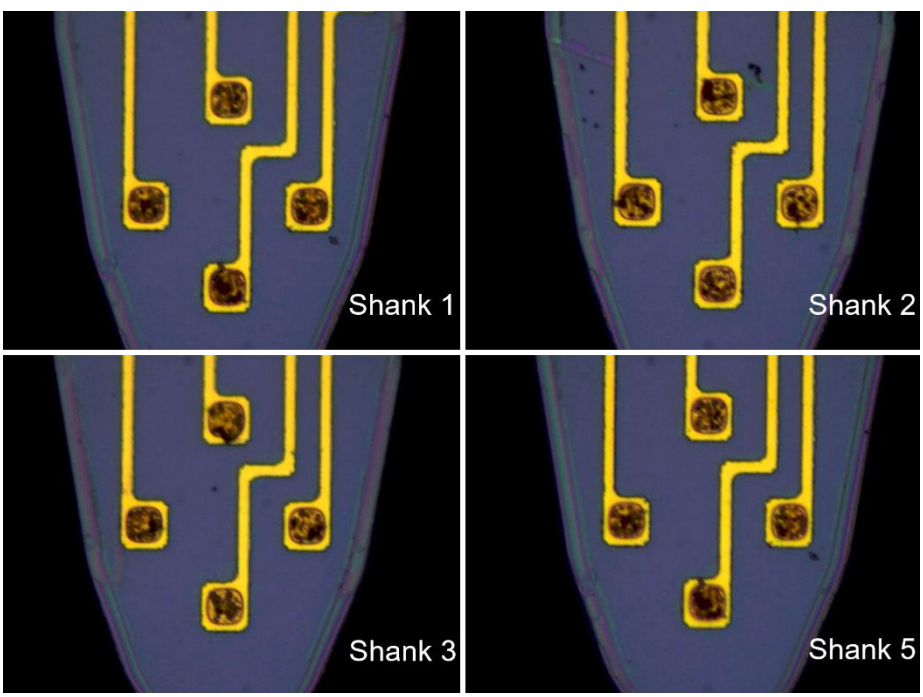

Figure 38. IrOx electroplated on the recording electrodes.

3.4. System integration

3.4.1. LED integration

GB QSSPA1.13-HYJX-35-1 470 nm LED is placed on a 3D printed housing as shown in figure 39. The 3D printed housing aligns the LED and the lenses. At the waveguide tip, transmitted light is visible when LED is on. To block any stray light except from the waveguide tip, 3D printed housing cover is placed on the silicon optrode, and small portion of black epoxy (832B-A, MG Chemicals, Canada) is applied on tiny side corner part of silicon body.

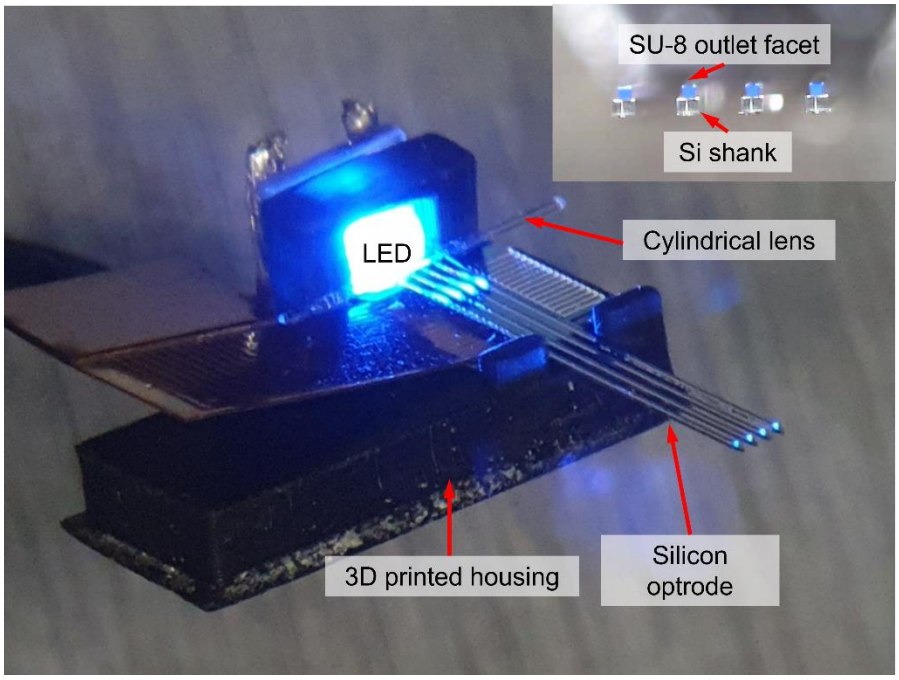

Figure 39. Integration of light source and silicon optrode.

3.4.2. Electrical connections

The flexible PCB is connected to 17 pin FPC connector (502078-1710, Molex

Inc., Japan). On the other side of the PCB, Omnetics connector (A79038-001, OMNETICS Connector Corp, USA) is connected to the electrophysiology recording system (RHD2132 recording system, Intan technologies, USA).

A microcontroller (NRF24LE1, Nordic Semiconductor, Norway) is programmed to adjust period and duration of LED pulses, and 50 mA current from general purpose input output (GPIO) pin is used for an LED illumination. For the electrical circuit power source, lithium polymer battery is attached. Figure 40 shows the integrated silicon optrode system.

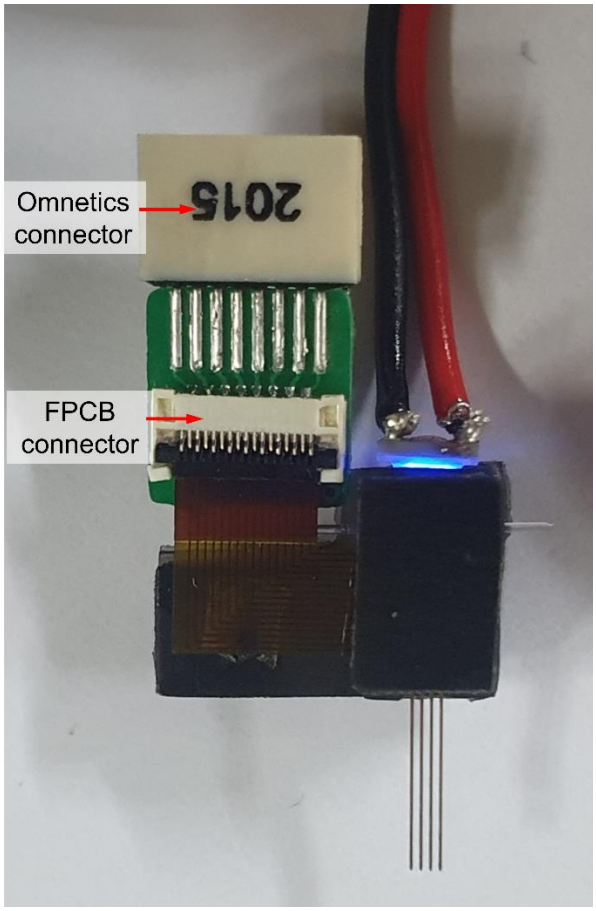

Figure 40. Silicon optrode system with electrical connections.

3.5. In-vivo experiment setup

3.5.1. Transgenic rat preparation

Sprague-Dawley rats (male, 8 months of age, 250 g) were used for the *in-vivo* experiments. The animal care and surgical procedures were approved by the Institutional Animal Care and Use Committee (IACUC) at the Ewha Womans University (No. 20-029). All in-vivo experiment was performed by Youjin Lee at Ewha Womans University. For the optogenetic experiment, AAV-CamKIIa-hChR2(H134R)-EYFP (Enhance Yellow Fluorescent Protein) (1.51×10^{14} GC/ml AAV as genome copies per mL) was used as a viral vector for gene transfection to express channelrhodopsin-2 (ChR2) in Ca^{2+}/calmodulin-dependent protein kinase II-positive neurons in the specific brain area. The rats were anesthetized with a ketamine-xylazine cocktail at an initial dose of 0.15 mL per 100 g using an i.p. (intraperitoneal) injection. Syringe pumps (Pump11 Elite Nanomite, Harvard Apparatus, Holliston, MA, USA) were used to microinject the viral vector into the hippocampus (Anterior-Posterior, AP: -3.8 mm, Medial-Lateral, ML: ±3 mm, Dorsal-Ventral, DV: -3 mm). Figure 41 shows the viral vector injected region. The injection volume was 1.5 μL, and the virus was injected slowly over 15 minutes using a 10 μL syringe (80330-701RN, Hamilton Company, Reno, NV, USA). After injection, an additional 5 minutes was required to stabilize the diffusion of the viral vector, and then the injection needle was taken out slowly.

Four weeks after the delivery of the viral vector, the silicon optrodes were inserted under isoflurane anesthesia (2-5 %). Silicon optrode was placed in hippocampus CA2 and CA1 (hippocampus, AP: -3.8 mm, ML: 2.3-3.3 mm, DV: -

2.8 mm) to simultaneously stimulate ChR2 expressing neurons and recorded evoked neural responses.

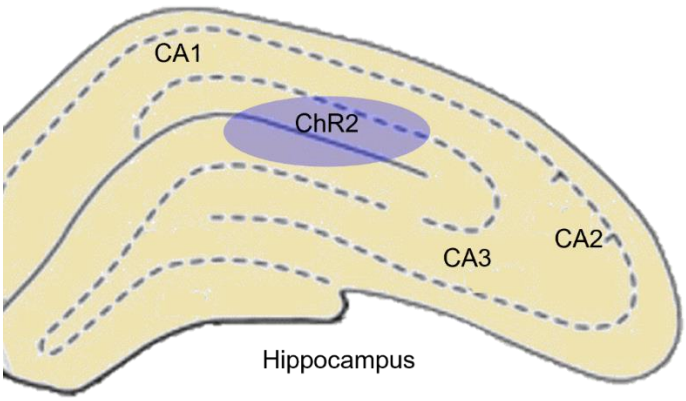

Figure 41. AAV-CamKIIa-hChR2(H134R)-EYFP viral vector injection area.

3.5.2. Electrophysiology recording system setup

The optrode was connected to the electrophysiology recording system (RHD2132 recording system, Intan technologies, Los Angeles, CA, USA). Raw neural signals (0.1-20 kHz bandpass filtered, 60 Hz notch filtered) were recorded at a 25 kHz sampling rate, amplified, and digitized using an Intan RHD2132 headstage. After 5 minutes baseline recording of spontaneous neural activities, optical stimulation with 470 nm LED light was delivered to activate ChR2-expressing excitatory neurons in the hippocampus.

4. Results

4.1. Optical characteristics measurement

4.1.1. Optical power measurement setup

The optical power meter (PM100D, Thorlabs Inc, USA) and a photodiode sensor (S121C, Thorlabs Inc, USA) are used to measure the light power from the silicon optrode tip array. Figure 42 shows the integration of light source with 3D printed housing cover.

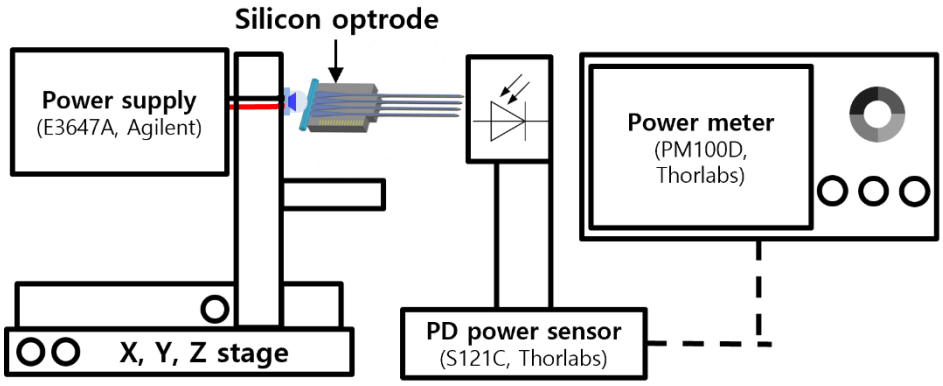

Figure 42. Optical power measurement setup.

4.1.2. Measurement analysis

When 50 mA forward current is applied to the LED, the voltage across the LED is 2.62 V and the electrical power consumption of the light source is 131 mW. Since the measured light power at 50 mA current is 62.5 mW, the LED efficiency is 48 %. The measured power at the end of the 4 optrode shanks P_{out} is 25.9 μW. The coupling

efficiency equation 11 gives η = -33.8 dB, where P_{in} is input power and P_{out} is output power. The light irradiance equation 12 gives 2.7 mW/mm^2, where A_{out} is the area of 4 SU-8 waveguide outlet A_{out} = 4 x 60 μm x 40 μm = 9,600 μm^2. By removing cylindrical lens, the measured P_{out} is 5.6 μW, irradiance I_{out} is 0.6 mW/mm^2 and η is -40.4 dB. Without both cylindrical lens and SU-8 lens gives the measurement of P_{out} = 1.23 μW, I_{out} = 0.13 mW/mm^2 and η = -47.1 dB. Table 10 summarizes the measured power of light at the optrode tip with various lens setup.

$$\eta = 10 \cdot \log \left(\frac{P_{in}}{P_{out}}\right) \quad (11)$$

$$I_{out} = \frac{P_{out}}{A_{out}} \quad (12)$$

Table 10. Measured light power at the SU-8 waveguide tip to see the lens effect.

	Measured power
No lens	1.23 μW
Only SU-8 lens	5.6 μW
Cylindrical & SU-8 lens	25.9 μW

The light experiment data showed the coupling efficiency enhancement of cylindrical lens and SU-8 lens are 6.7 dB and 6.6 dB respectively. The measured coupling efficiency is close to the designed efficiency of cylindrical lens and SU-8 lens which are 6.1 dB and 7 dB respectively. Figure 43 shows the light output irradiance with lenses versus LED current.

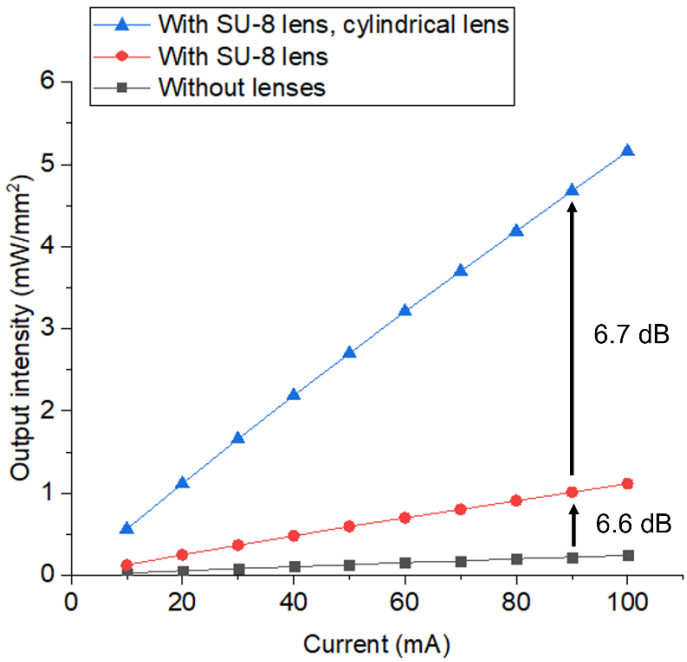

Figure 43. LED forward current vs 470 nm irradiance graph.

Figure 44 shows images of light at the end of waveguide tip with different forward current of LED. When the output power from waveguide tip is measured, stray lights are blocked by 3D printed test zig and rubber clay for the accurate measurement.

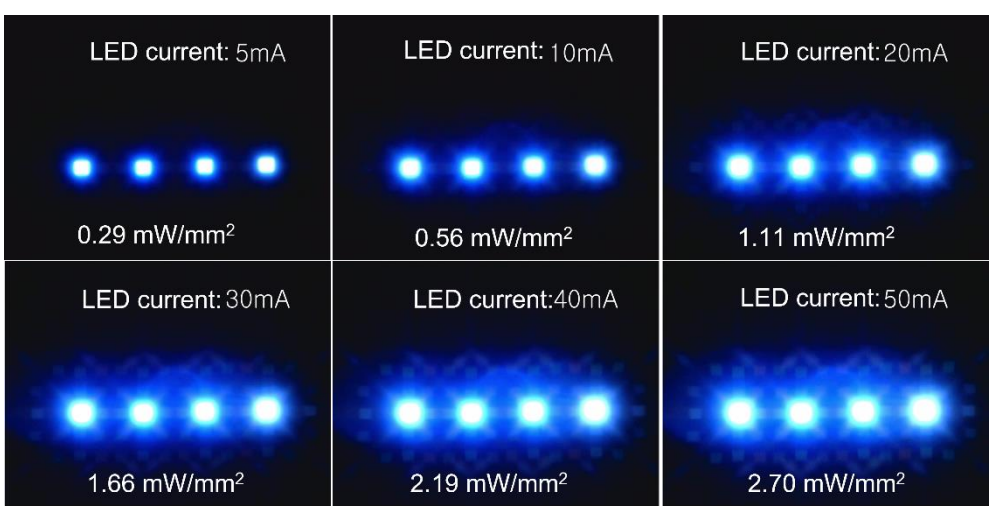

Figure 44. Blue light at the waveguide tip and measured irradiance.

Within the light power measurement at the waveguide outlet, irradiance at the recording electrodes is expectable by the acceptance angle of SU-8 waveguide. From the section 2.1 lens design part, the acceptance angle of air to SU-8 core with SiOx cladding gives θ_i = 26˚. Based on the waveguide acceptance angle θ_i, light dispersion angle at the waveguide tip θ_o = 18.8˚ is calculated by the Snell's law, where refractive index of brain n_o = 1.35. As shown in figure 45, the light geometrical dispersion depends on the distance from the tip of waveguide d. For both height and width of light dispersion increased by equation 13 and 14, where w, h, $w_{dispersion}$ *and* $h_{dispersion}$ are width, height, dispersion width at distance d and dispersion of height at distance d of the SU-8 waveguide, respectively. Within the measured light power at each shank P_{out} = 25.9 μW / 4 = 6.5 μW, irradiance at the distance from waveguide tip is given by equation 14.

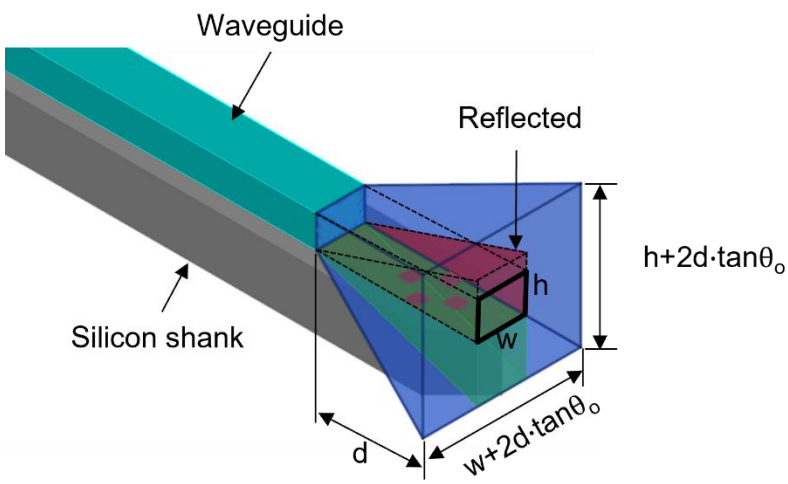

Figure 45. Schematics of light geometrical dispersion.

$$w_{dispersion} = w + 2d \cdot \tan\theta_o \quad (13)$$

$$h_{dispersion} = h + 2d \cdot \tan\theta_o \quad (14)$$

$$I_{dispersion} = \frac{P_{out}}{w_{dispersion} \cdot h_{dispersion}} \quad (15)$$

Since there is reflected light due to the bottom silicon substrate, neurons above the electrodes are illuminated with higher irradiance than $I_{dispersion}$, which is irradiance at the distance from waveguide tip. To calculate the irradiance added by the reflected light power, the reflected light area, $A_{reflected}$ at the distance d is calculated by equation 16, and the power delivered to the neurons above the electrodes is calculated by equation 17, where $A_{SU\text{-}8}$ is SU-8 waveguide outlet facet area. In here, neurons parallel to the SU-8 waveguide region is considered and the maximum $A_{reflected}$ is set to constant value when reflected light passes over the SU-8 outlet height, $h = d \cdot \tan\theta_o$. Then the irradiance on the electrodes $I_{reflected} = P_{reflected} / A_{SU\text{-}8}$ is calculated. Figure 46 shows the irradiance above the light reflection region versus the distance from the waveguide tip, and where the height of reflection beam exceeds the waveguide height $h = d \cdot \tan\theta_o$, light intensity decreases quickly.

$$A_{reflected} = d \cdot \tan\theta_o \cdot w \quad (16)$$

$$P_{reflected} = \left(A_{reflected} + A_{SU-8}\right) \cdot I_{dispersion} \quad (17)$$

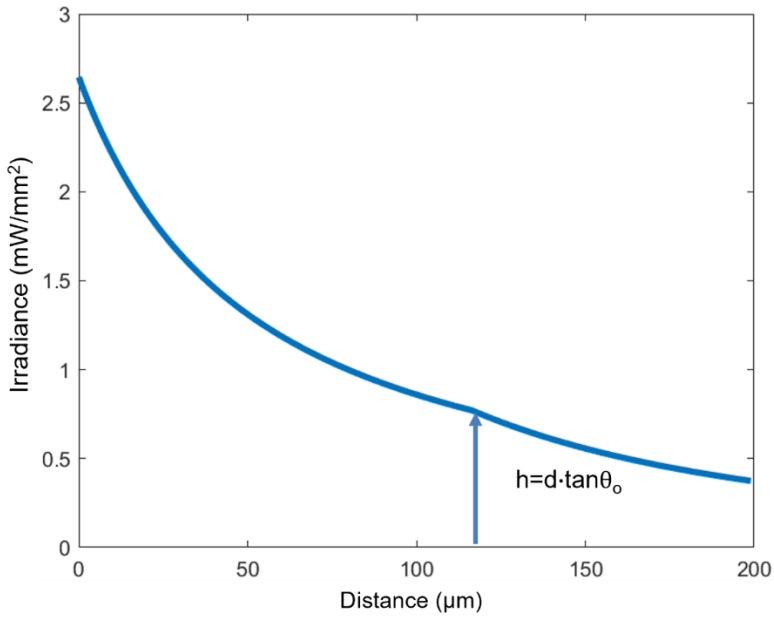

Figure 46. Distance from the waveguide tip vs irradiance graph.

Figure 47 shows the number of illuminated neurons by the distance increasement based on the cell density 20,000 cells/mm^3 [11].

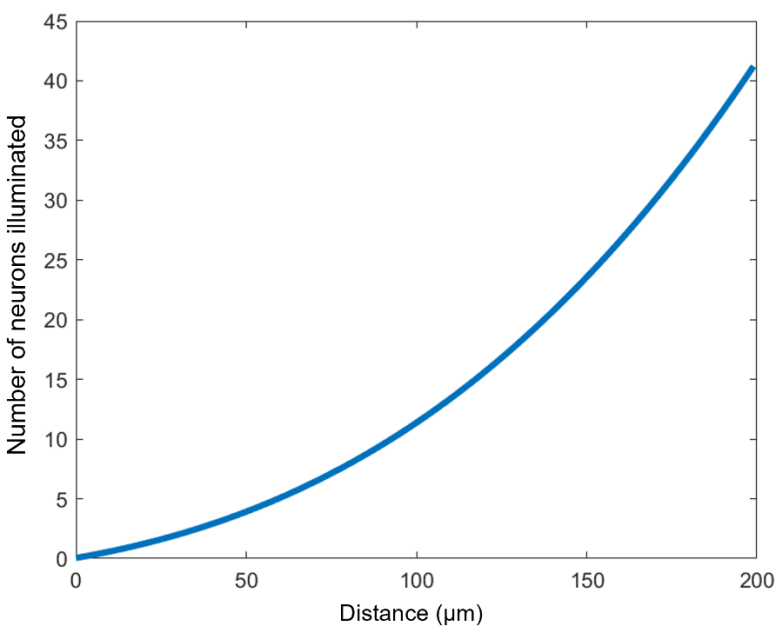

Figure 47. Distance from the waveguide tip vs number of neurons illuminated.

Figure 48 shows the light intensity map of the neurons above 4 electrodes location. The closest electrode to the waveguide tip has approximately 1 mW/mm^2 irradiance, and the rest of the electrodes are below 1 mW/mm^2. From the result, all the electrodes are delivered by greater than 0.5 mW/mm^2 light irradiance. The irradiance map is generated by MATLAB software.

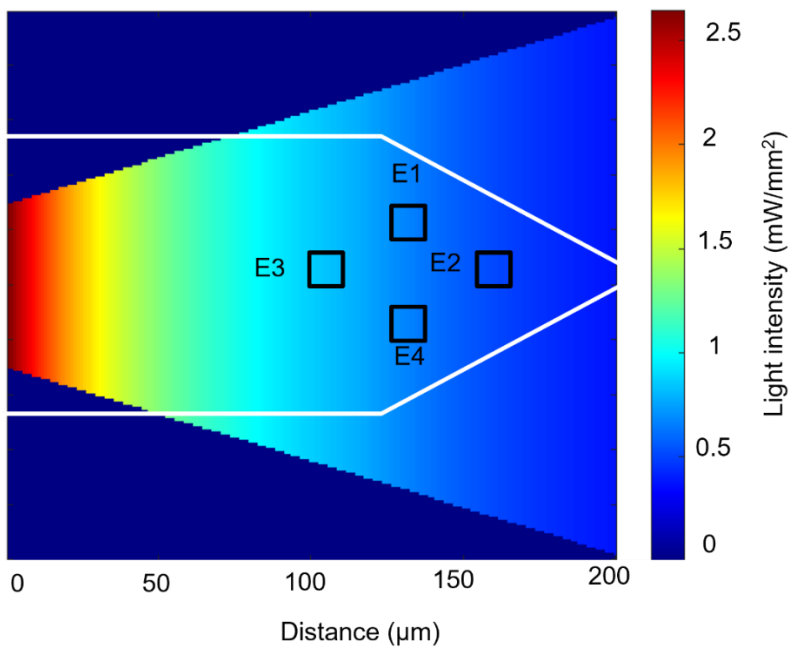

Figure 48. Light intensity map of silicon optrode tip.

To measure the light irradiance differences among the four shanks tip, an image of light illumination at the tip was acquired as figure 49 (a). Using MATLAB program, blue light value of the image was converted to the corresponding intensity map as shown in figure 49 (b). From the result of blue light value at shanks tip end, the light irradiance values measured at the four shanks tip were almost the same.

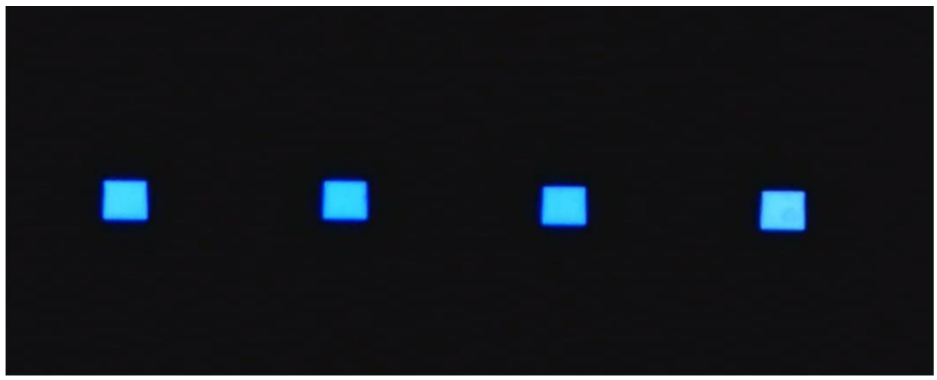

(a)

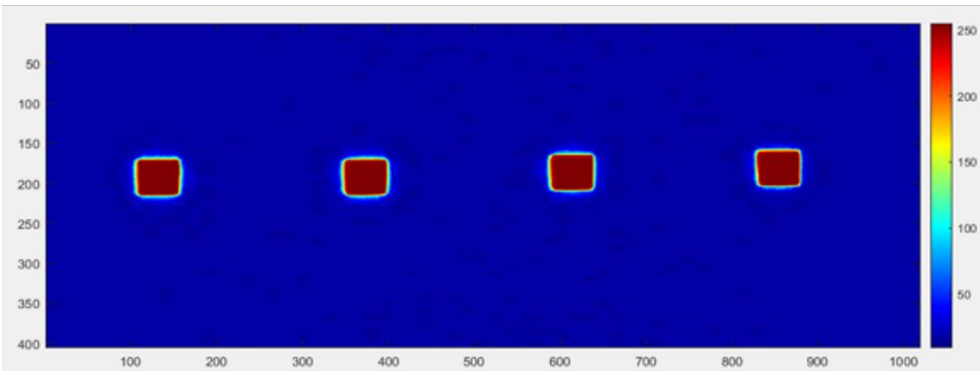

(b)

Figure 49. (a) Light illumination at the four shanks tip and (b) blue light value conversion into light intensity map using MATLAB.

4.2. In-vivo experiment and spike analysis

4.2.1. *In-vivo* insertion location and shank data

The insertion location of the silicon optrode is hippocampus CA1 and CA2 region. The exact location is highlighted in figure 50. The shank 4 is inserted into the dentate gyrus and other shanks are remained at the CA1 region.

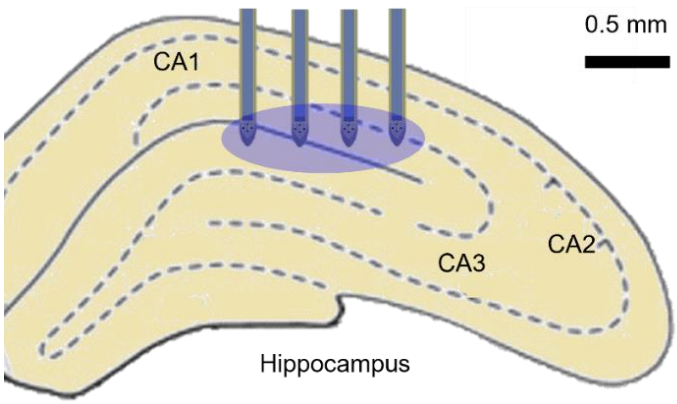

Figure 50. Silicon optrode inserted area of rat brain.

Total 16 electrodes and shank numbers are labeled as shown in figure 51. The shanks are apart from adjacent ones by 300 μm pitch, and the total dimension of array is 1 mm width. There is a 200 μm gap between adjacent shanks.

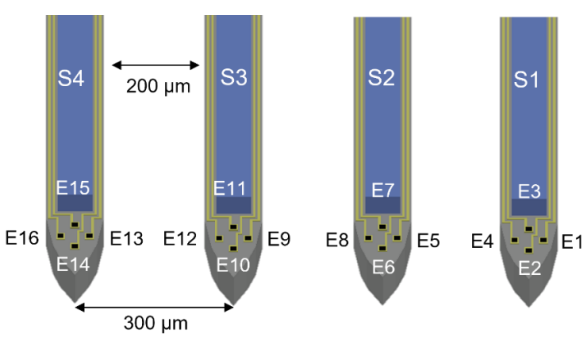

Figure 51. Electrodes and shank numbering of fabricated silicon optrode.

4.2.2. Custom MATLAB spike analyzer program

For the neural spike data analyzation from the law data, MATLAB scripts are made to remove electromagnetic interference (EMI) noise. The raw data contains 4 ~ 6 mV EMI noise, when 50 mA LED forward current is on and off. Figure 52 shows the image of raw data. The sampling rate is set to 25 kHz. Since the noise is much higher than the neural activity voltage, appropriate filters must be applied to the data.

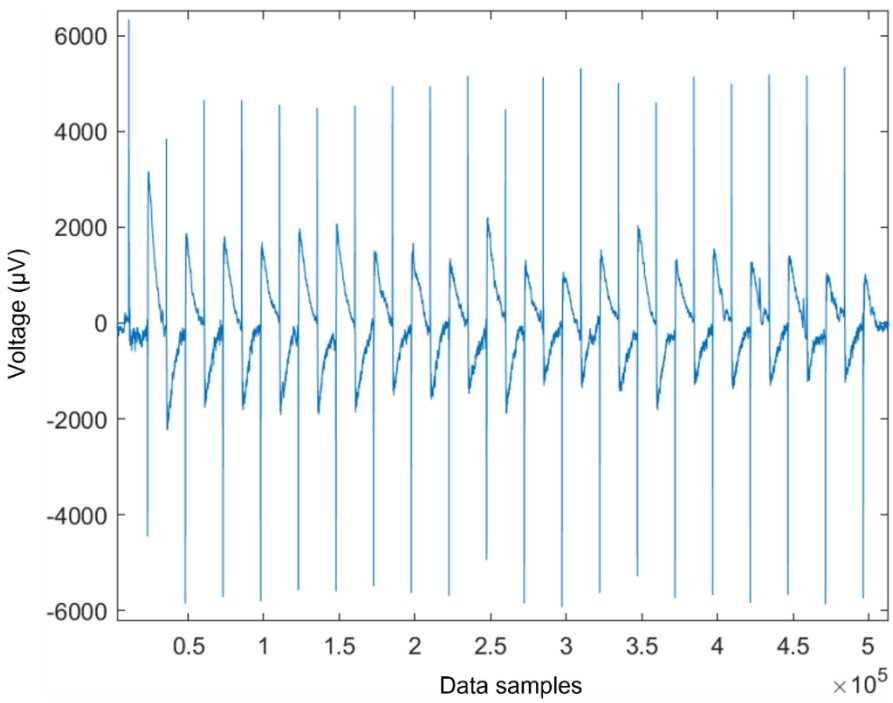

Figure 52. The raw data with EMI noise obtained from Intan recordings.

To suppress the noise, while not losing the spike data, the law data is digital filtered with 2nd order high pass Butterworth filter with cutoff frequency at 500 Hz and low pass with cutoff frequency at 5,000 Hz. Since the spikes have 1,000 Hz frequency, the filters applied above affects the spikes. However, 500 Hz high pass

filter can suppress the EMI noise better than the typical 250 Hz high pass filter. Figure 53 shows the filtered data which suppresses the noise quickly.

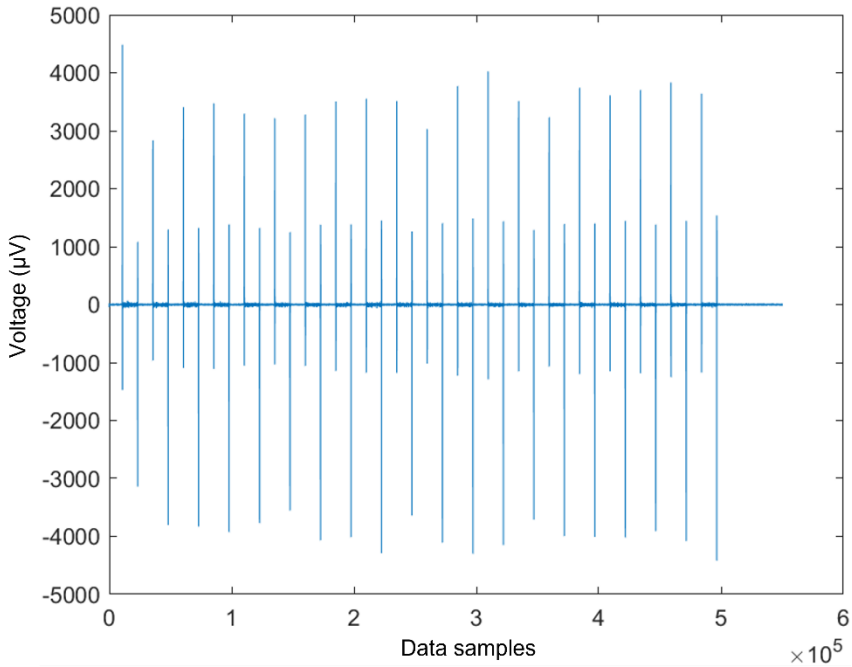

Figure 53. Suppressed noise using 500 Hz high pass and 5,000 Hz low pass.

Then spikes which are synchronized to the optical stimulation is observed with *y*-axis zoom as shown in figure 54.

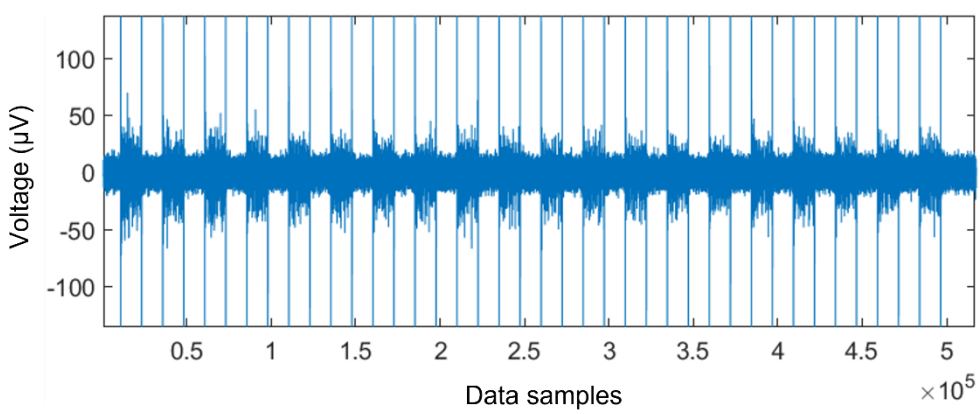

Figure 54. Neural activities synchronized to optical stimulation.

To recognize spikes automatically, the custom MATLAB code sweeps 2 ms duration dataset which is 50 sample points and finds if the difference of local maximum and minimum exceeds the threshold value that user typed. If there exist spikes within the threshold, data point where the local maxima or minima are marked with *x*, as shown in figure 55.

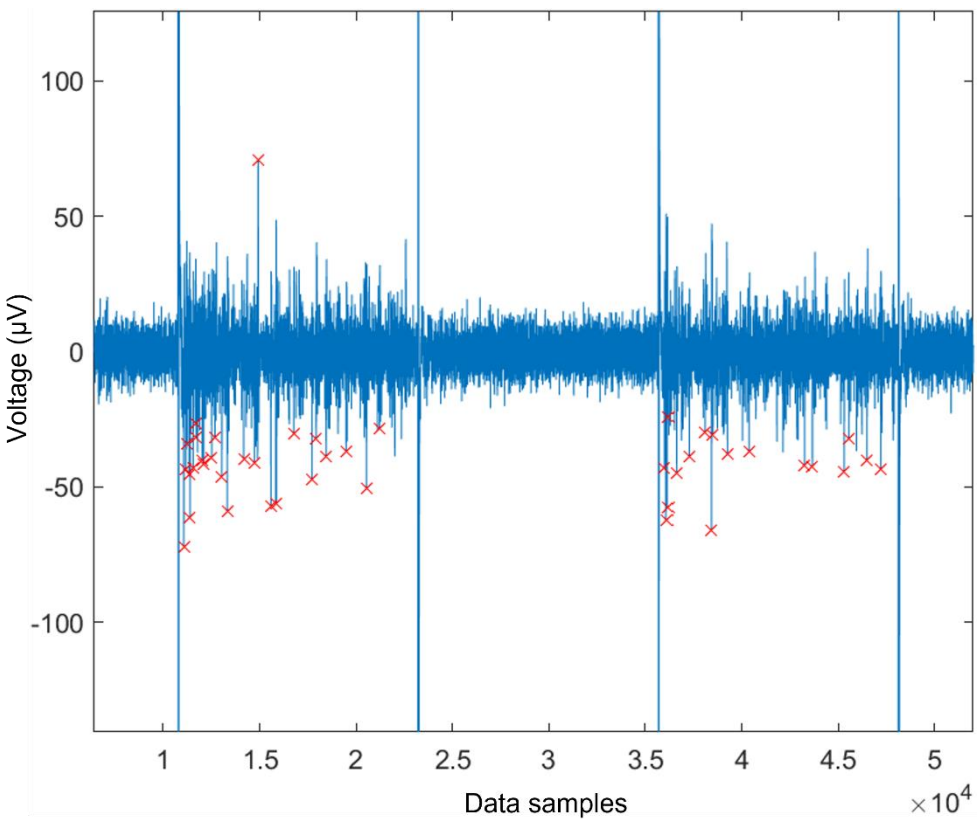

Figure 55. Local minima or maxima are marked on the spike presumed point.

To separate the EMI induced noise from LED, the local maxima, or minima with greater than 500 μV are managed in the separate data bin. The automatically clustered EMI noise from LED on and off are shown in figure 56 (a) and (b). The figure 56 (c) and (d) show the clustered positive peak spikes and negative peak spikes.

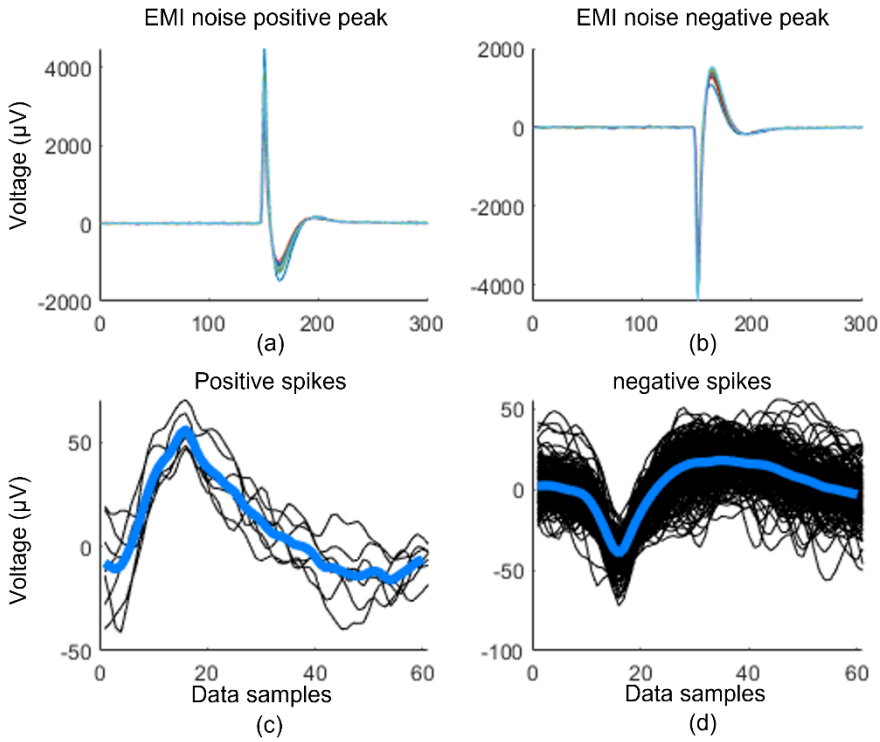

Figure 56. Automatically clustered spikes from the custom MATLAB algorithm, EMI noise from LED on current (a), EMI noise from LED off current (b), positive peak spikes (c), and negative peak spikes (d).

When more than one neuronal activity are observed, the custom MATLAB algorithm separates the spikes. Figure 57 shows the automatically detected spikes from electrode E13. It looks like there are two different neuronal activities, but there are three neuronal activities.

Using K-means clustering algorithm, 3 features of spikes which are peak value, slope before peak (pre) and after peak (post) are compared. Figure 58 shows the result of clustering by 3 features. Two obvious cluster by peak value is observed and two cluster by post slope are also observed even though it is not visible from figure 57 graph.

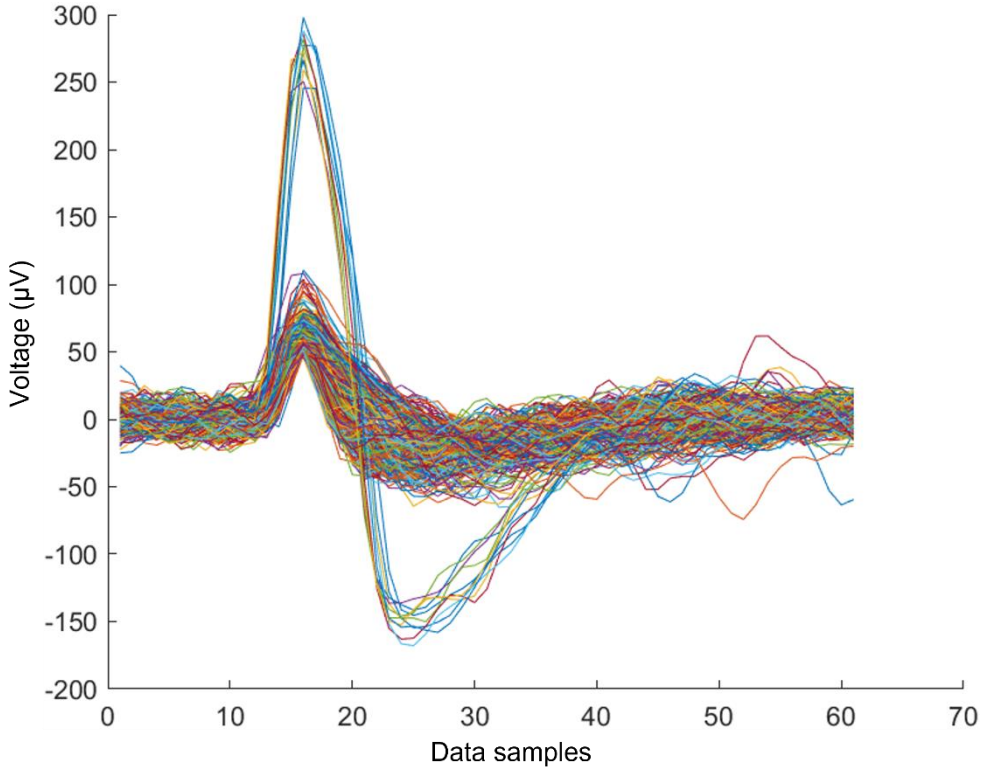

Figure 57. Automatically detected spikes with 3 different neural activities.

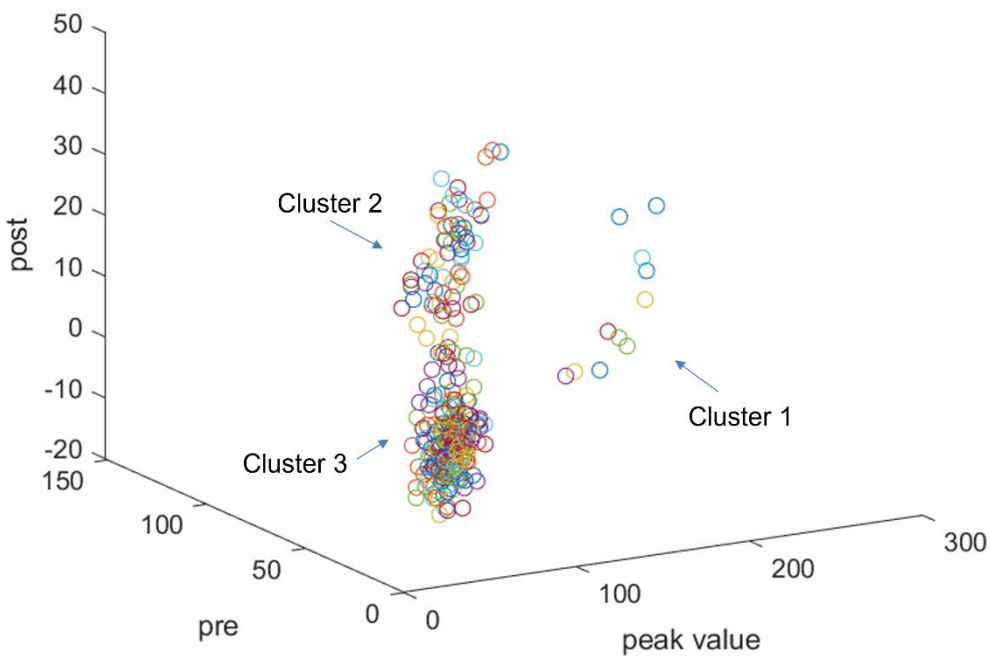

Figure 58. Three neuronal activities clustered by K-means clustering algorithm.

From figure 59, clustered samples are marked in different colors and each centroid is marked in black X marker. Figure 60 shows the result of separated neural activities by custom algorithm.

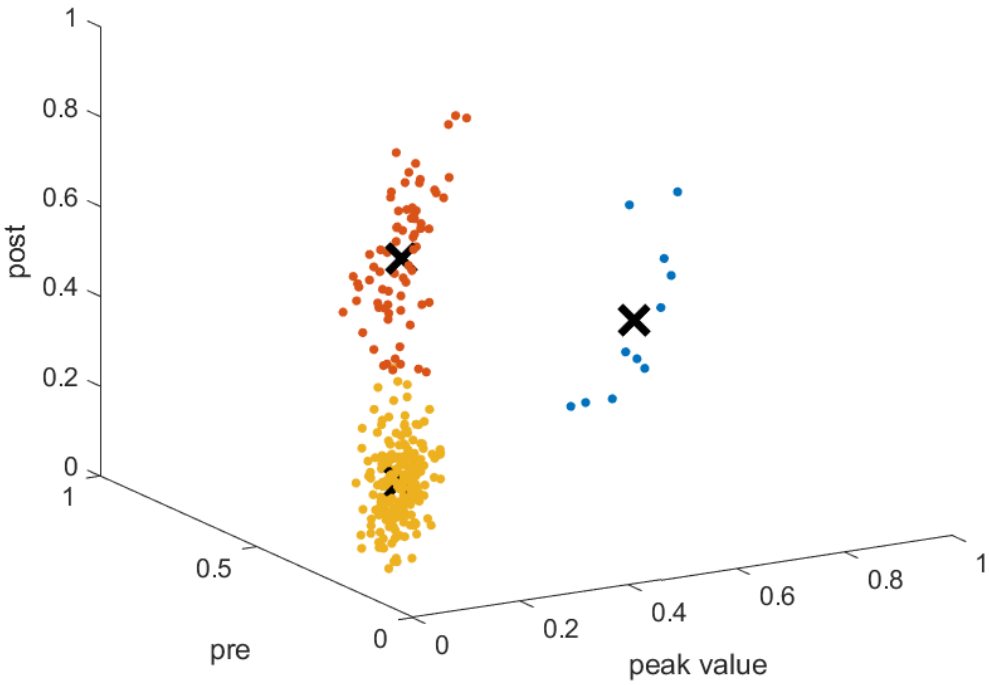

Figure 59. Clustered samples and its centroids marked by black X mark.

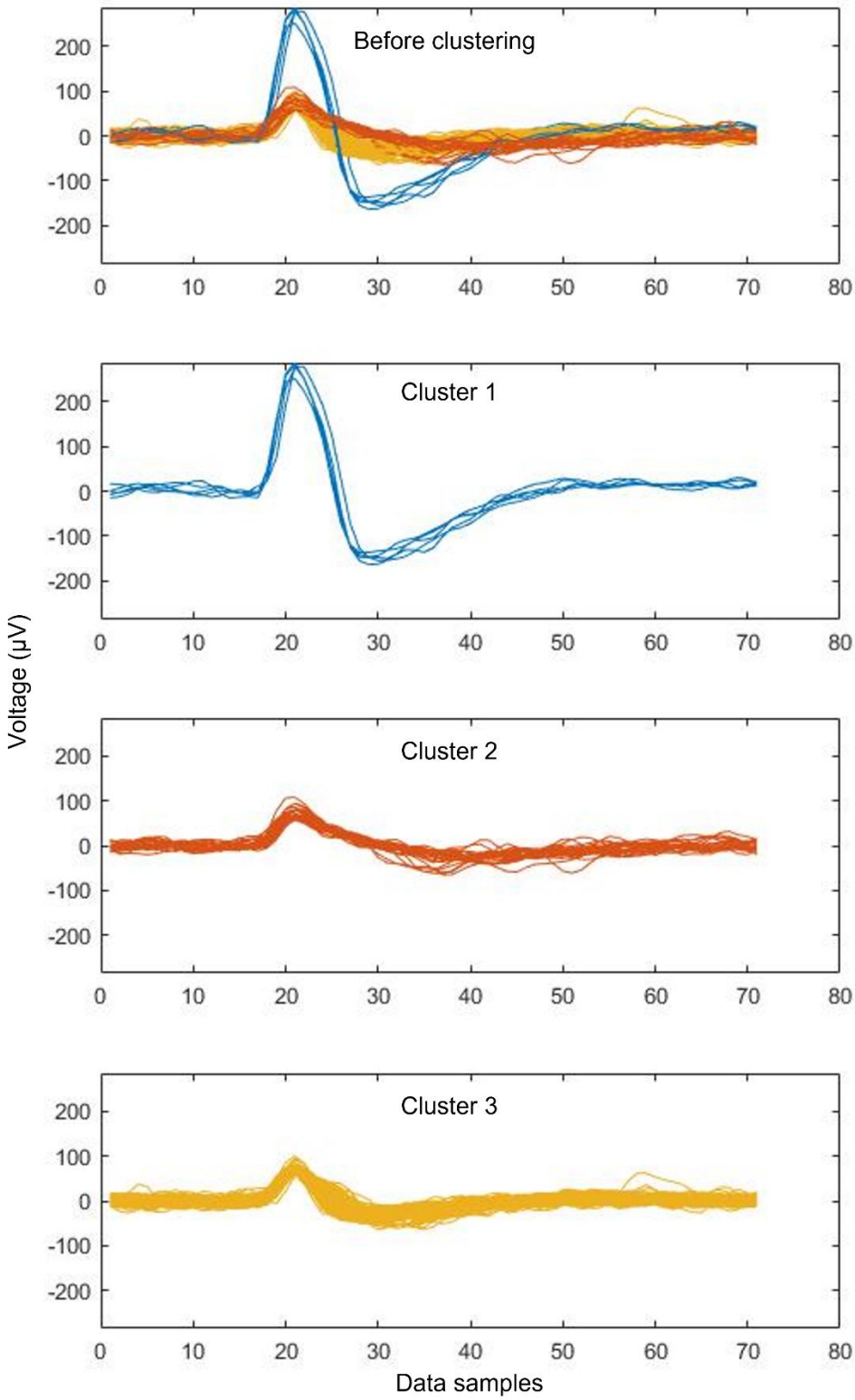

Figure 60. Automatically separated spikes by custom MATLAB algorithm.

4.2.3. In-vivo experiment result

Figure 61 shows the raw data of optogenetic experiment. Spikes at shank S1 to S3 are synchronized to the optical stimulation. Spikes from shank S4 are detected independently to the optical stimulation, and spike bursting is observed. Electrode number 7 data is lost due to the wrong wiring of Intan electrophysiology recording system.

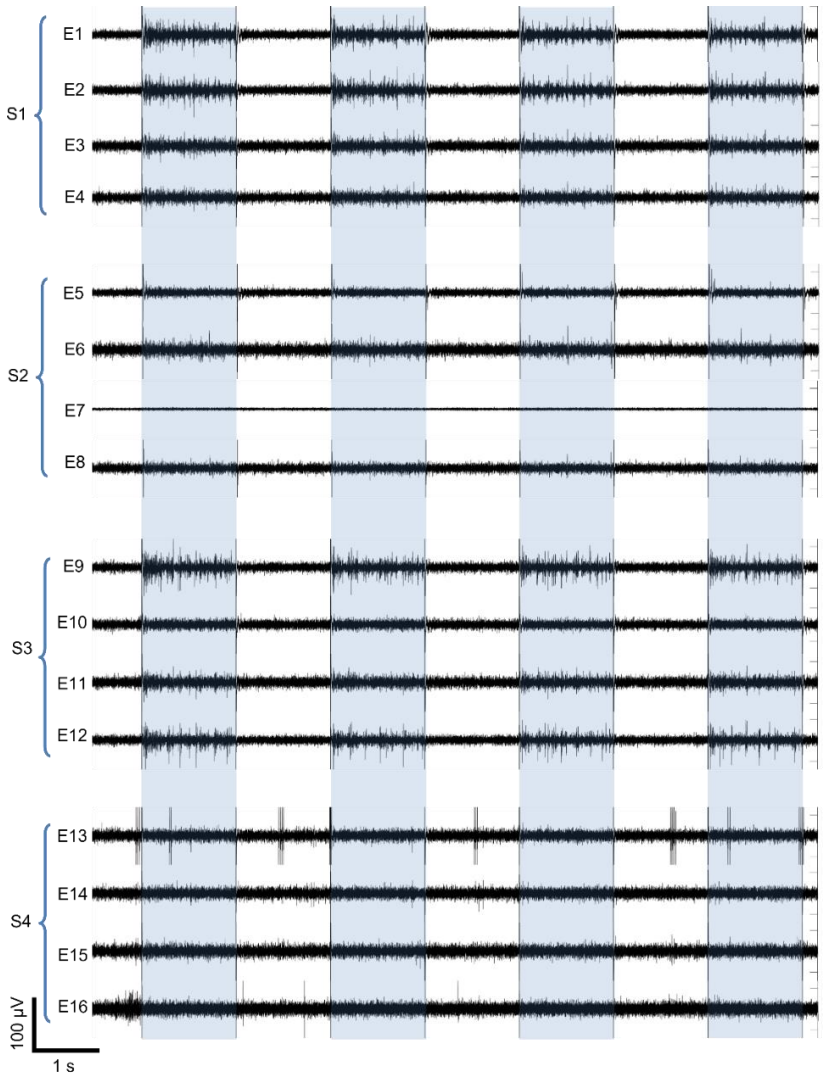

Figure 61. Optogenetics experiment raw data.

Figure 62 (a) shows clustered spikes on each shank. Spikes peak time and optical stimulation time information are saved for raster plot and peristimulus time histogram (PSTH). Figure 62 (b) shows the raster plot and (c) shows the PSTH. The raster plots of S1 and S2 show barely detected spikes until 100th trials, however after 100 trials, spikes increased with optical stimulation. There was 5 minutes break before 100th trial, and 101st trial.

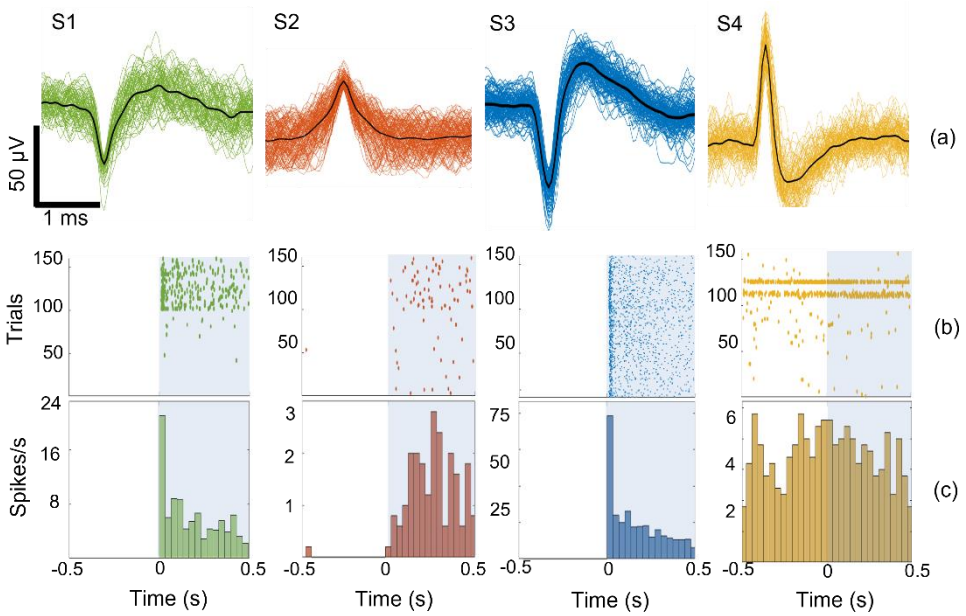

Figure 62. Clustered spikes (a), raster plot (b) and PSTH (c).

Before the optogenetics experiment, baseline recording was performed. There was sporadic neural activities observed at shank S1 and S2. The neurons at shank S3 and S4 showed the active responses as shown in figure 63 (b). When the optogenetic stimulation is performed, neural activities were synchronized.

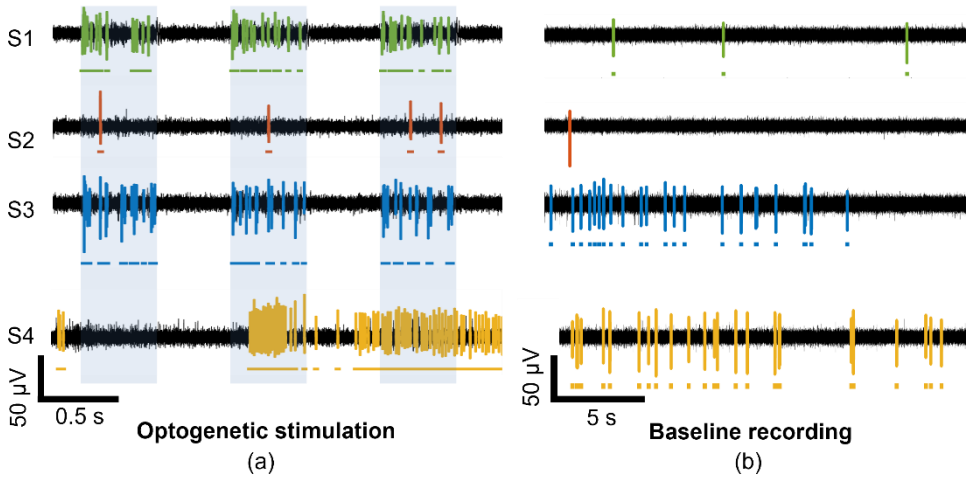

Figure 63. Optogenetic stimulation (a) and baseline recording (b).

4.2.4. Fluorescent image verification

To verify the evoked neural spikes induced by the light stimulation are from the optogenetics response, brain fixation and perfusion is performed by Youjin Lee at Ewha Womans University. After *in-vivo* experiment, transgenic rat perfusion is proceeded with saline solution and paraformaldehyde using Flow Rate Peristaltic Pump (Lab V1, Baoding Shenchen Precision Pump Co., China).

Under anesthesia procedure, 20-gauge blunt-tipped perfusion needle was inserted into the ascending aorta through ventricle. While the saline solution perfuses the rat, liver color should be monitored carefully. When the liver color changes to ivory, pump valve is switched to perfuse paraformaldehyde. The solution flow rate is kept at 20 ml/min for 200 ~ 300 grams body weight. Since the goal of fixation is to preserve tissue in a life-like state, the process should be done as soon as possible. After the rat body become hardened, the brain is extracted, left overnight in paraformaldehyde. Then the brain is emerged into the 30% sucrose PBS solution until brain sinks down to the bottom of tray. The brain is coronal sectioned on a

Cryocut Microtome (CM1850, Leica, Germany) at 40 μm thickness and stored in antifreeze solution at 4 °C. The brain slices are washed with PBS three times and placed on slide glasses. CMOS camera (Zyla 5.5, ANDOR, UK) and inverted microscope (IX71, Olympus, Japan) is used to visualize EYFP-positive neurons. If genes are expressed, ChR2 express green light under 473 nm blue laser light source due to the viral vector contained fluorescent protein such as EYFP. Figure 64 shows fluorescent image of ChR2 expressing neurons at hippocampus area.

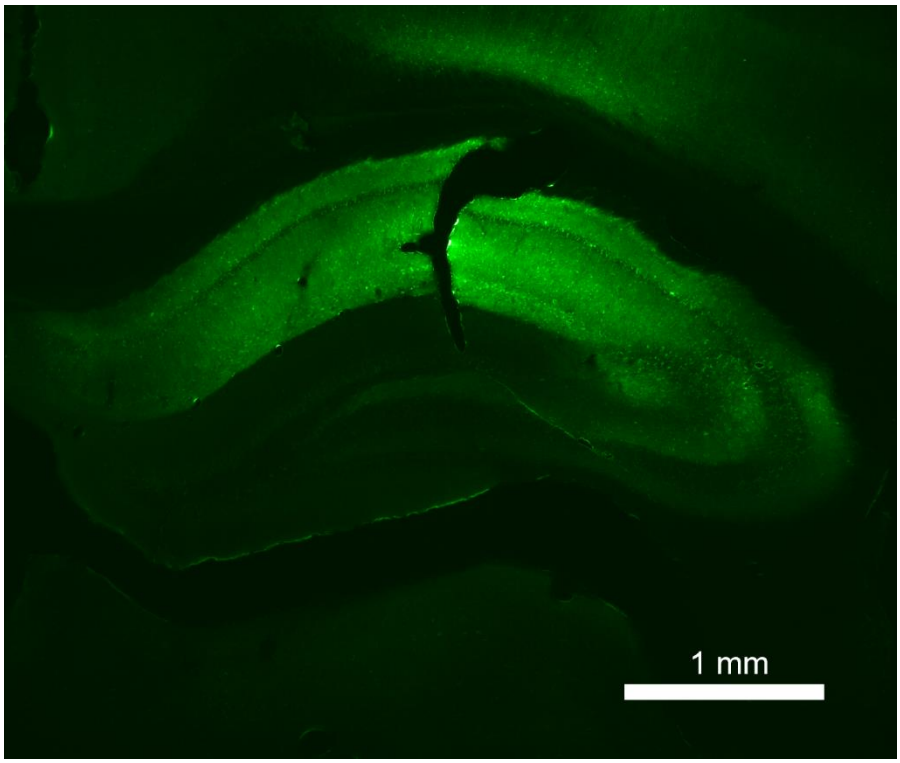

Figure 64. Fluorescent image of ChR2 expressing neurons at hippocampus after in-vivo experiment.

5. Discussion

5.1. Optical output power analysis

5.1.1. Theoretical value and measured data of lens efficiency

According to measured lens coupling efficiency, the light efficiency of the cylindrical lens was higher than expected. The designed and measured coupling efficiency of the cylindrical lens is 6.1 dB and 6.7 dB, respectively. However, as mentioned in design section 2.1.2, 6.1 dB efficiency enhancement is only based on skew ray calculation. There was an assumption that meridional rays are very small portion to the skew rays because of the stiff angle of rays from lenses. Since the numerical aperture calculation of the SU-8 waveguide considering the meridional rays is higher than that of the skew rays, the acceptance angle of the meridional rays (61°) is higher than that of skew rays (26°). The 470 nm LED used in this experiment has a beam divergence angle of 80°, and potentially the meridional rays further increased the light coupling efficiency by 0.6 dB. Table 11 summarizes the theorical and measured efficiency of lenses.

Table 11. Theoretical efficiency and measured deficiency of lenses.

	Theoretical efficiency	Measured efficiency
Cylindrical lens	6.1 dB	6.7 dB
SU-8 lens	7 dB	6.6 dB

5.1.2. Theory and empirical data of irradiance at the waveguide tip

The source-coupled waveguide scheme causes light coupling loss from comparably large LED dimension and small optical fiber cross-sectional area, and a larger beam dispersion angle of LED than that of the laser source is another main cause of light coupling loss. The maximum coupling efficiency (η_{max}) in the Lambertian source-coupled waveguide is given by equation 10 in section 2.1.4, where A_{WG} is the cross-sectional area of the waveguide, A_{source} is the light-emitting area [1], [11]. Since the light-emitting area of the LED is Φ2 mm, A_{source} is 3.14 mm^2, A_{WG} is 0.0096 mm^2, and η_{max} is equal to -36.5 dB. SU-8 waveguide transmittance is decreased by -6.4 dB/cm with 470 nm wavelength [46], [47]. By adding the transmittance of SU-8, which is -7 dB at 11 mm length, -43.5 dB can be obtained, which is comparable to the measured coupling loss of the LED and SU-8 waveguide, which is -47.1 dB when both lenses are not used.

5.2. In-vivo experiment

5.2.1. Silicon optrode validity

The *in-vivo* animal experiment was performed by Youjin Lee at Ewha Womans University. The knowledge about the animal experiment in chapter 5.2 is provided by Youjin Lee. The experiment with transgenic rats validated the feasibility of the proposed optrode system for simultaneous light delivery and electrophysiological recording. For optogenetic modulation, wild-type rats were transfected with the ChR2 virus, whose expressions are restricted to excitatory neurons in the hippocampus. The CaMKII in the viral vector is a gene with expression restricted to excitatory neurons in the hippocampus. As a result, neural activities from the optogenetic stimulation and the spontaneous spikes can be observed. The silicon probe was able to record the changes of neural signals, and further signal processing with custom MATLAB code established the raw data analysis. Moreover, we have validated that the changes in neural activities were from optogenetic stimulation, using fluorescence imaging to visualize the cells expressing ChR2. The ChR2 expression can be estimated from EYFP intensity. As shown in figure 64, ChR2 was well expressed throughout the hippocampus CA2 and CA1.

5.2.2. Analyzation of experiment result from silicon shanks

Twelve channels successfully recorded neural signals, and eight channels detected the synchronized neural signals with optical stimulation. However, the other channels had no significant synchronization in the firing rate during optical

stimulation. The results can be interpreted as the neurons near the channels may not have been the excitatory neurons. The CaMKII is a gene with expression restricted to excitatory neurons in the hippocampus, but the distribution of CaMKIIα expression is known to be approximately 70 % [63]. For instance, in case of S2 with E6 and 8, no significant difference between the on and off period was observed as shown in figure 61. Another potential cause is that the electrode channels could have been inserted near neurons which did not express ChR2. As shown in figure 50, S4 was located where the virus was not expressed. Therefore, the immediate effect of optical stimulation of excitatory neurons could not have been detected.

Hippocampus has an excitatory pathway between CA2 and CA1 pyramidal neurons. It is also known that CaMKII plays a critical role for learning and memory formation in the hippocampal neurons [64], [65]. Accordingly, the responses of each shank can be interpreted based on their locations. Except S4 placed in regions where ChR2 were not expressed, S3 showed the most active firing during optical stimulation than the other shanks. This can be expected that when CA2 was stimulated optically, the evoked neural responses of the CA1 neurons accumulated. Therefore, it can be assumed that S1 showed active firing due to the accumulation of CA2 activation by S2 optical stimulation and CA1 activation by S1 itself. Although S4 was not inserted into the ChR2 expressed area, bursting occurred due to the delivery of the stimulation from CA1 and CA2.

5.2.3. Reinforcement of synaptic connections

Reinforcement of synaptic connections by optical stimulation can be confirmed from the results that S1 and S2 shows spikes increasing after 100th trials. Until the

100th trials, the response to the optical stimulation is insignificant, but after the 100th time, the response tends to increase suddenly. This can be explained by the strengthening of synaptic connections by repeated optical stimulation of excitatory neurons. In this context, the pattern of increased bursting after stimulation is also related to synaptic strength. As shown in figure 63 (a), neuronal signals recorded in S4 increased bursting compared to the baseline recording. It has been known that bursting modulates plasticity in hippocampus [66]. Therefore, the increase in bursting is an important result from the point of view of learning and long-term memory, and it can be verified through various behavioral experiments, which are related to cognitive flexibility in animals.

5.2.4. Advantages of suggested silicon optrode

One of the most significant advantages of the proposed silicon optrode is that the light delivery system is based on LED. Compared to the laser-based system, the developed optrode is compact and suitable for the above-mentioned behavioral *in-vivo* experiments. Even though LED generally has much lower power than laser, the developed LED-based optogenetic system dramatically increased the output optical power using a glass cylindrical lens and SU-8 plano-convex lenses between an LED and SU-8 waveguide. Therefore, it was possible to obtain an appropriate light intensity for optogenetic experiments. Moreover, several advantages of LED-based optogenetic systems can be secured, such as the low system complexity, cost-effectiveness, and high potential for wireless system development. In addition, the recent rapid improvement of LED can increase the output power of LED so that new LEDs can be easily adapted to the developed device by simple replacement. Also,

by utilizing the variety of LEDs with different wavelength, diverse optogenetic experiments can be carried out. For instance, different opsins responding to different wavelength lights can be activated with a single optrode system using a color-switching LED.

5.3. Wireless optogenetics neural interface

5.3.1. Analog front end circuit design

To verify the validity of the suggested silicon optrode to the wireless usage, a wireless optogenetics neural interface has been designed. The method to record electrophysiological signal is utilizing high gain instrumentation amplifiers. MAX4209 from Maxim integrated circuits offer low offset voltages and 100 gain value. It has gain bandwidth product at 750 kHz, and within 100 V/V gains, it acts as 7.5 kHz low pass filter. There is an active low pass filter connected after the instrumentation amplifier. 0.68 μF capacitor and 1 kΩ resistor in series acts as 0.24 kHz high pass filter (HPF). The LTC2052 zero drift op amp from analog devices has been used to establish the 10 V/V gains. The overall gain of the analog front end circuit is 1,000 V/V. There are 4 channels recording system in the wireless neural interface and therefore, 4 analog front end circuits exist. Figure 65 shows the analog front end circuit design.

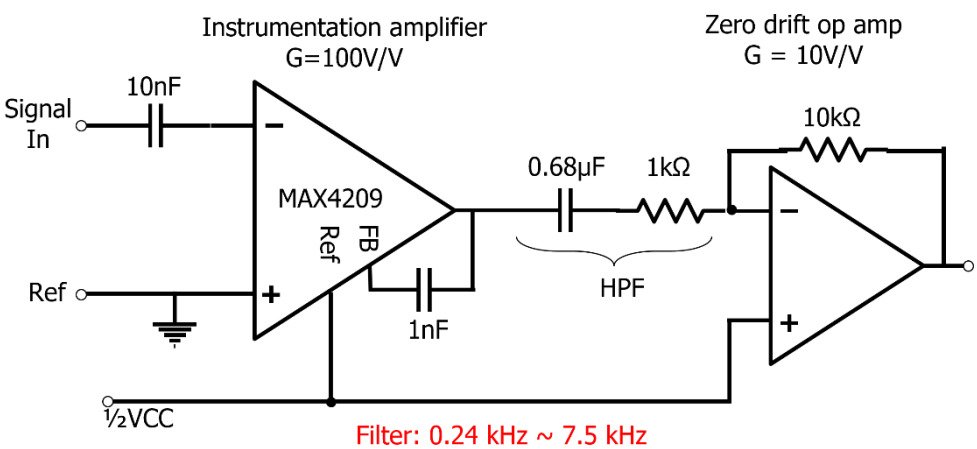

Figure 65. Analog front end circuit design.

5.3.2. Wireless system design

The wireless SoC board consists of nRF24LE1 RF chip, which operates RF frequency at 2.4 GHz. It has 2 Mbps data transfer rate, and the maximum data throughput in can achieve is 0.8 Mbps with no acknowledgement. The chip offers 10 channels 12-bit SARADC (successive approximation analog to digital converter) channels. The RF SoC is widely used in mouse, keyboard, or local wireless devices. Key features of the chip is shown in figure 66. Using a free compiler tool called SDCC (Small Device C Compiler), C language code is written to the chip.

Key Features

- nRF24L01+ 2.4 GHz transceiver (250 kbps, 1 Mbps and 2 Mbps air data rates)
- Fast microcontroller (8051 compatible)
- 16 kB program memory (on-chip Flash)
- 1 kB data memory (on-chip RAM)
- 1 kB NV data memory
- 512 bytes NV data memory (extended endurance)
- AES encryption HW accelerator
- 16-32bit multiplication/division co-processor (MDU)
- 6-12 bit ADC
- High flexibility IOs
- Serves a set of power modes from ultra low power to a power efficient active mode
- Several versions in various QFN packages:
  - 4×4mm QFN24
  - 5×5mm QFN32
  - 7×7mm QFN48
- Support for HW debugger
- HW support for firmware upgrade

Applications

- Computer peripherals
  - Mouse
  - Keyboard
  - Remote control
  - Gaming
- Advanced remote controls
  - Audio/Video
  - Entertainment centers
  - Home appliances
- Goods tracking and monitoring:
  - Active RFID
  - Sensor networks
- Security systems
  - Payment
  - Alarm
  - Access control
- Health, wellness and sports
  - Watches
  - Mini computers
  - Sensors
- Remote control toys

Figure 66. nRF24LE1 RF system on chip key specifications from datasheet.

5.3.3. PCB design

Printed circuit board (PCB) has been designed using Eagle CAD software. Dimension of the board are minimized by separating RF SoC PCB and analog front

end PCB. Two different circuit board are stacked to minimize the device size effectively. The dimension of each PCB is 11 x 11 mm^2 as shown in figure 67.

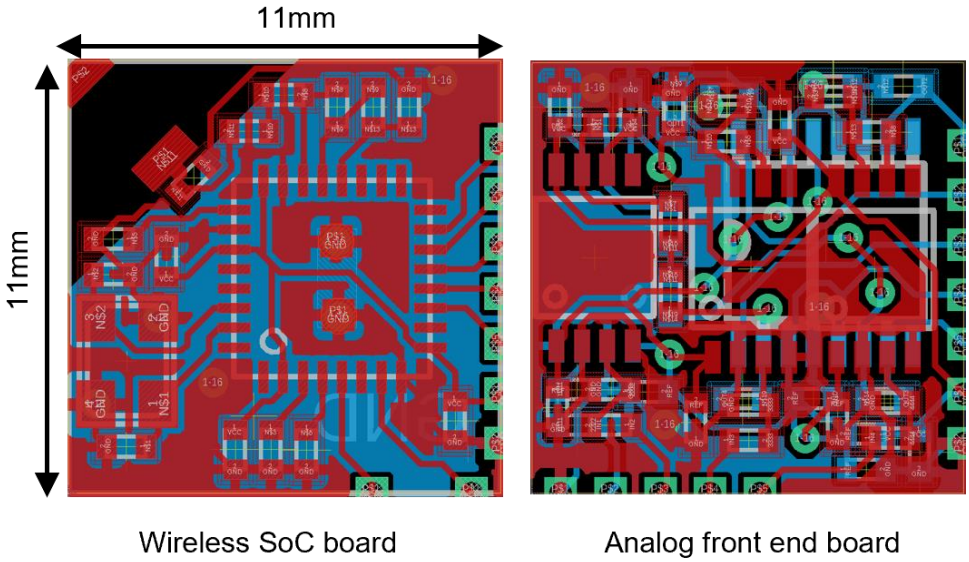

Figure 67. Wireless board and analog board design using EagleCAD.

In the RF SoC PCB board, chip antenna has been installed to minimize the size. The importance of designing wireless board is antenna. Impedance must be matched to maintain the best wireless performance. The 50 Ω impedance matching with transmission line is designed using AppCAD software. It is a free software that provides many RF analysis toolkits. There are two types of widely used transmission lines in PCB design which are coplanar waveguide and microstrip. Microstrip has simple configuration with one wire line, but the transmission line width is wider than the coplanar waveguide. Also, it is vulnerable to the EMI noise. Coplanar waveguide, however, has smaller transmission line width, and more immune to the noise than the microstrip line. Therefore, coplanar waveguide is the best option that meets our requirements. Figure 68 shows the coplanar waveguide design using AppCAD.

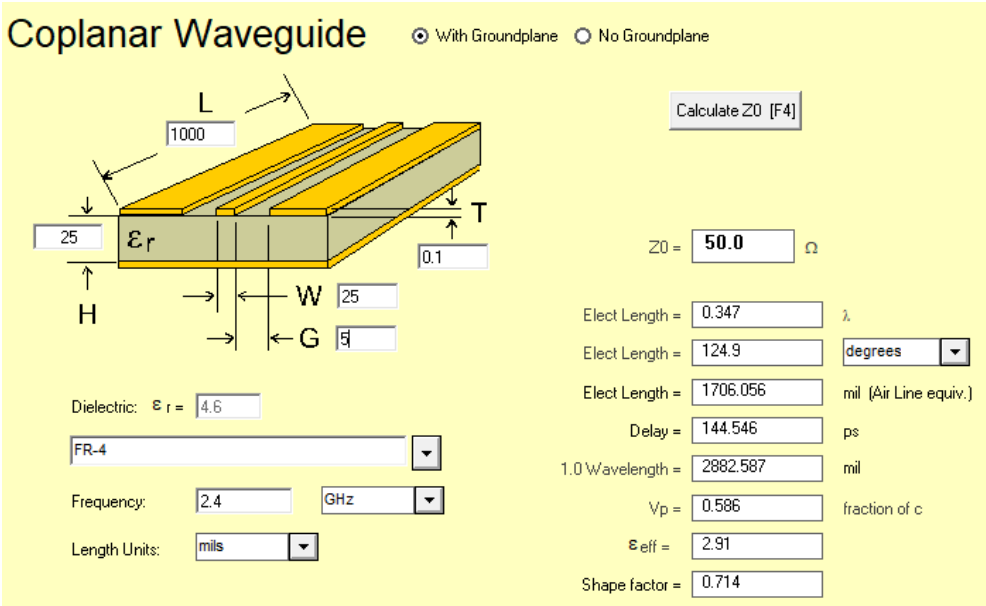

Figure 68. AppCAD coplanar waveguide impedance calculator.

The wireless PCB board has ground plane properly designed at the bottom of PCB. This reduces the interference of noise from high power antenna board and analog front end PCB. The digital circuit ground plane and analog circuit ground planes are maintained separately for unsharring of return current line. Considering return current line is very important for low noise device design.

After two PCBs are stacked together and soldered completely, the 3rd PCB which has flexible PCB sockets are vertically soldered to the analog front end PCB. The suggested silicon optrode is then combined with InGaN (Indium gallium nitride) LED in compact size as figure 69 shows. The white InGaN LED (SPMWH1228MD7WAPMVL, Samsung electronics) has maximum peak wavelength at 450 nm, as shown in figure 70. The LED is too powerful that the 470 nm light irradiance without cylindrical lens is 1.45 mW/mm^2 at the waveguide tip. Also at 589 nm wavelength, 1.13 mW/mm^2 irradiance is obtained.

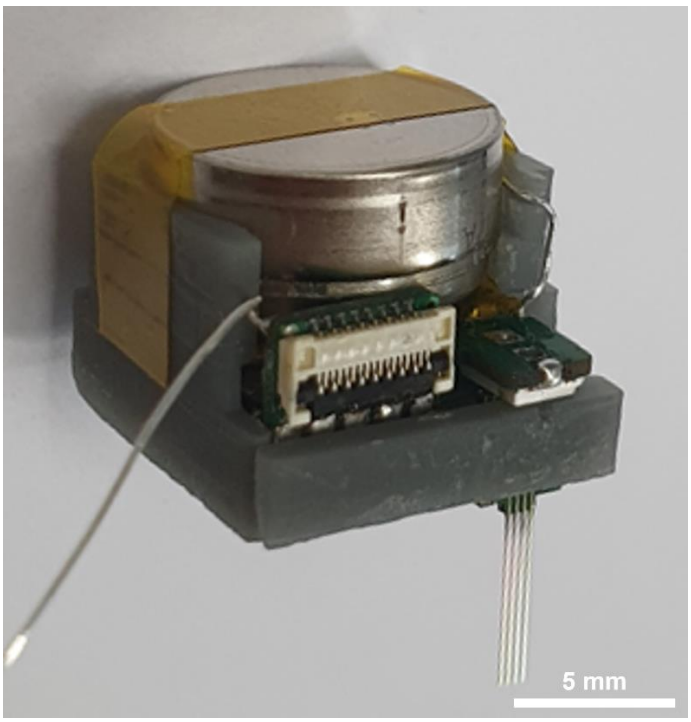

Figure 69. Wireless neural interface with suggested silicon optrode.

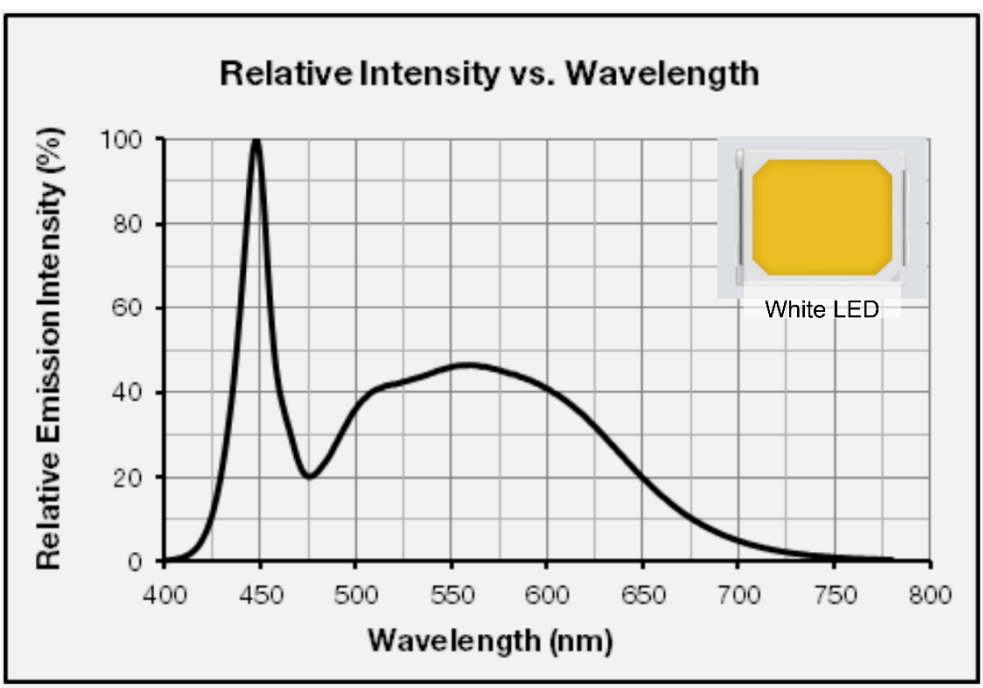

Figure 70. Relative emission intensity spectrum of white LED.

The analog front end circuit board has integrated circuit components at both top and bottom. Figure 71 (a) shows the image of top side and bottom side of the analog front end PCB. Figure 71 (b) shows RF SoC PCB and (c) is whole electric component together. Since there are only 4 recording channels, 4 electrodes at each shank are connected altogether to the 1 wireless neural interface channel.

When the light is turned on, as shown in figure 71, 470 nm light with 50 mA LED forward current is illuminated at the SU-8 waveguide tip. The battery used in the system is LIR1254 lithium-ion battery which has 45 mAh capacity. The battery dimension is ϕ12 mm and 5.4 mm thickness. Specification of wireless optogenetics neural interface is summarized in table 12. Comparison with other wireless optogenetics system for deep brain stimulation is shown in table 13.

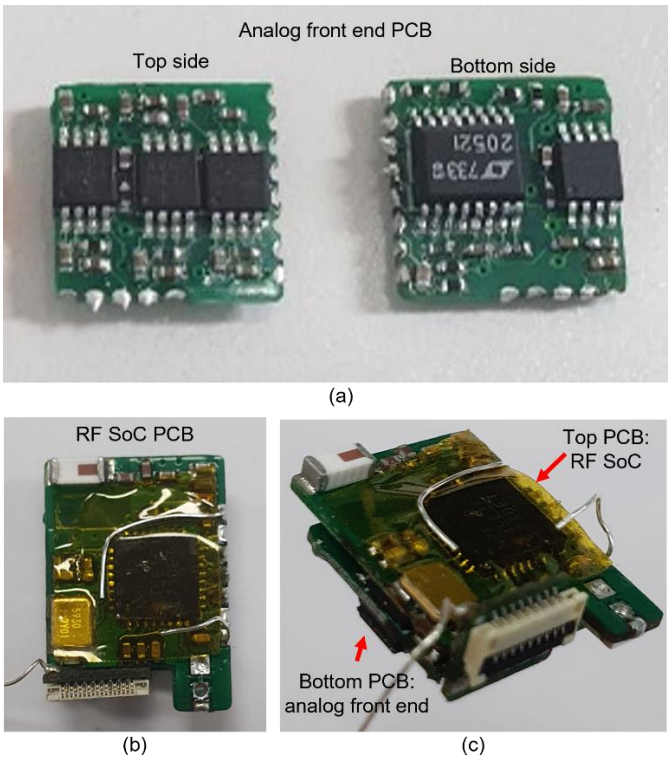

Figure 71. Wireless neural interface circuit boards (a) analog front end PCB, (b) RF SoC PCB and (c) whole electric components.

Figure 71 shows the packaged wireless optogenetics system with LED on.

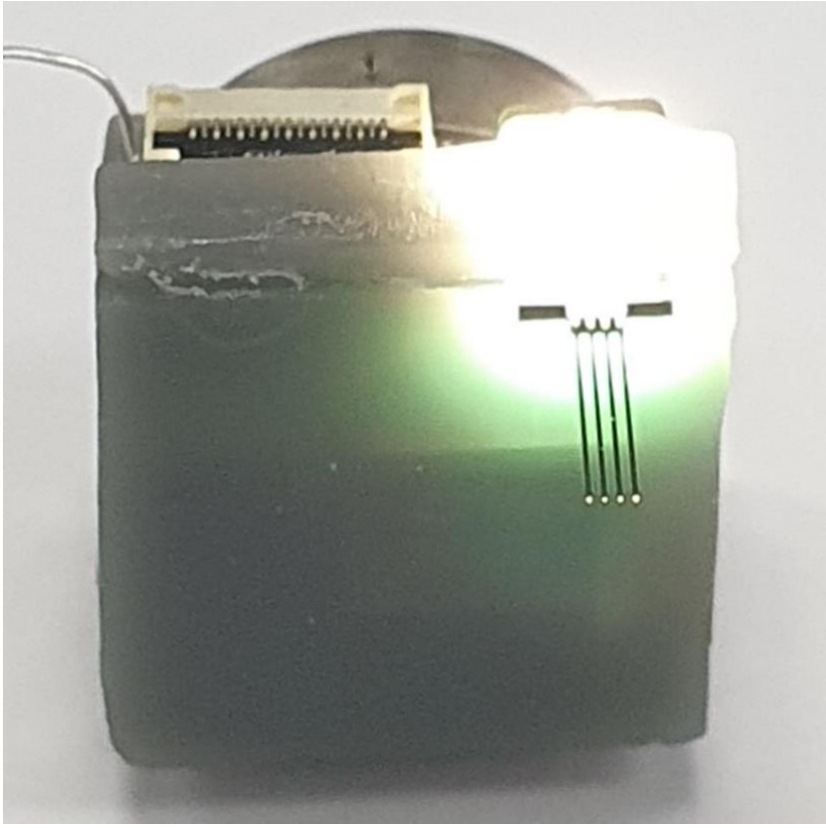

Figure 72. Wireless optogenetics system with light on.

Table 12. Specifications of wireless optogenetics neural interface.

Parameters	Value
System dimension	15 x 13 x 10 mm^3
Weight	3.2 g
Power without stimulation	96.2 mW
Number of recording channels	4
ADC resolution	12
Sampling rate per channel	16 ksps

Table 13. Deep brain stimulation wireless systems comparison.

	[67]	[68]	[69]	[70]	This work
Weight [g]	< 1.6	3.1	2.8	7	3.2
Light source	LED	μLED	LED	LED	LED
Power consumption	Two 50 μAh	5V battery	3.7V, 20 mAh	119 mW	96.2 mW
Recording channels	None	None	None	32	4
ADC resolution	None	None	None	16	12
Sampling rate per channel	None	None	None	20 ksps	16 ksps
Irradiance [mW/mm^2]	None	None	None	70	1.45
Dimensions [mm^3]	12 x 7 x 11	7 x 7 x5	950	17 x 18 x 10	12 x 7 x 11

5.3.4. Receiver programming

The receiver side of the system consists of nRF24LU1P chip which offers both wireless transceiver and the USB 2.0 data transfer. The wireless protocol with nRF24LU1P system on chip is compatible with nRF24LE1 system on chip. Using bulk transfer of USB 2.0, up to 12 Mbps data rate can be transferred to the host PC. Figure 73 shows nRF24LU1P wireless transceiver dongle.

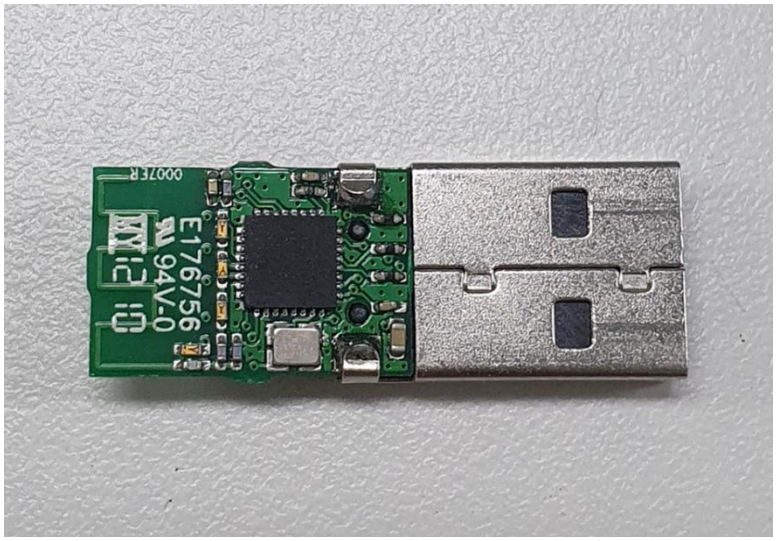

Figure 73. nRF24LU1P dongle.

5.3.5. PC software

The wireless USB device is connected to PC and controlled by PC software written in C# language. When the user sends the recipe information for optogenetics stimulation, the information is sent to the nRF24LU1P through USB, and nRF24LU1P sends these data wirelessly to the nRF24LE1 chip. Then nRF24LE1 illuminates light and sends the 4 channel 12-bit recording electrode data back to nRF24LU1P. When nRF24LU1P chip receives recording electrode data, these data are sent to the PC through USB bulk transfer. Then C# program receives and plot the neural activity graph. Figure 74 shows 1 kHz 1mV_{pp} AC voltage data measured by wireless system and plotted on the custom C# program on host PC. Since gain of the analog front end is 1,000 V/V, the graph peak to peak voltage should be 1 V_{pp}. However due to the bandpass filter, the signal is attenuated to 0.83 V_{pp}. Figure 75 shows the neural activity recording of wireless neural interface on rodent model.

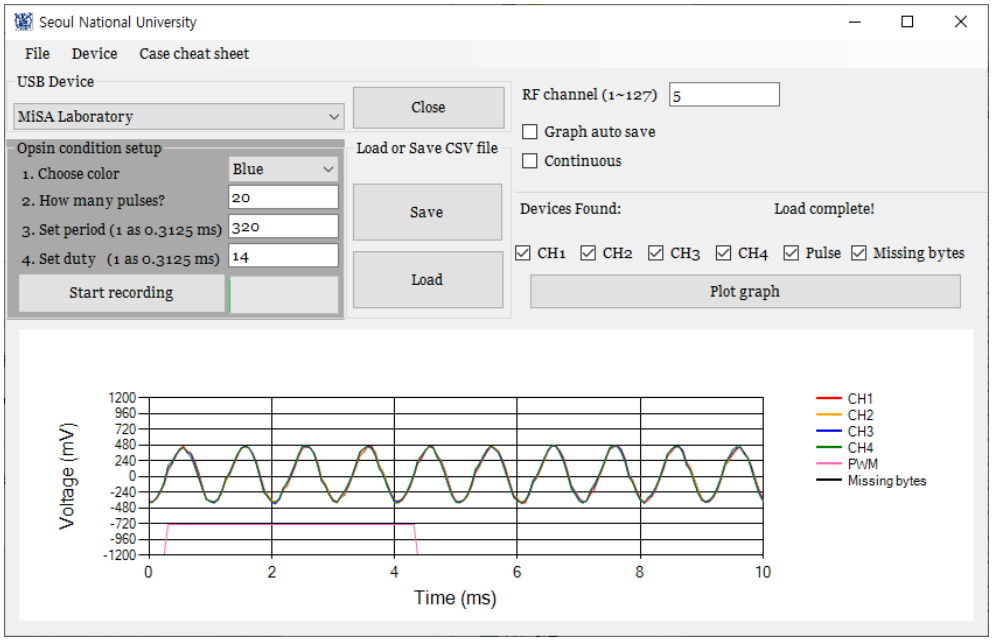

Figure 74. Plotting 1kHz 1mV$_{pp}$ AC voltage data transmitted by wireless neural interface on C# PC software.

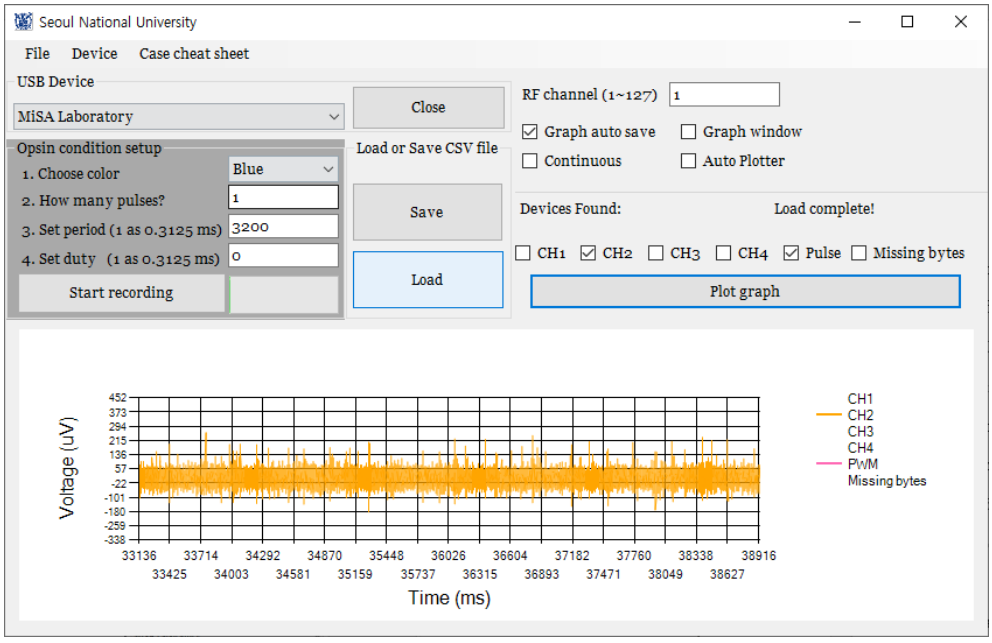

Figure 75. Neural activity recording of wireless neural interface on rodent model.

6. Conclusion

Monolithically integrated LED and SU-8 waveguide coupled silicon optrode is proposed in first time. In this scheme, compatibility of wireless neural interface and heat safety feature are provided. The one huge drawback is low light irradiance at the tip due to the wide dispersion angle of the LED and low coupling efficiency. To enhance the light coupling efficiency between an LED and SU-8 waveguide and to narrow the beam dispersion angle, MEMS fabrication compatible lenses, which are glass cylindrical lens and SU-8 plano-convex lens, are designed and integrated. Since 3-dimensional lens shape is hard to approach within MEMS fabrication process, two lenses are employed to handle vertical light focus and lateral light focus separately.

The designed efficiency of the cylindrical lens and SU-8 convex lens is 6.1 dB and 7 dB, respectively. The measured efficiency of the cylindrical lens and SU-8 convex lens is 6.7 dB and 6.6 dB, respectively. The cylindrical lens has higher empirical measurement of efficiency than the theoretical value, because the assumption of calculation is based on skew rays. The portion of meridional rays are assumed to be less than skew rays, since the LED has large beam dispersion angle, and lenses will also refract the angle precipitously.

When the silicon optrodes are fabricated, one critical issue was observed that the transmittance of SU-8 with 470 nm wavelength is too low to stimulate ChR2. The SU-8 waveguide transmittance degradation due to the silicon DRIE process has been resolved by fabrication sequence optimization. The precision alignment of the cylindrical lens is another serious problem, but it is solved using uniquely employed precision aligner.

When 50 mA LED forward current is applied to the 470 nm LED, the irradiance at the silicon optrode tip is 2.7 mW/mm^2. Through the light dispersion simulation, it has been confirmed that the neurons above the electrodes are illuminated with more than 0.5 mW/mm^2 light intensity.

The silicon optrode is electrically connected to FPCB by ACF bonding to reduce the size of device. The IrO_x electroplating is carried out to reduce the average electrode impedance from 2.57 MΩ to 43.6 kΩ. The optical stimulation part and recording electrodes are integrated into a compact package using custom 3D printed housing structure.

The optrode was inserted into the hippocampus of transgenic rat, and the ChR2 response showed the feasibility of optogenetic stimulation. Spikes from excited neurons were successfully detected from the raw data using custom MATLAB algorithm. 500 Hz to 5,000 Hz bandpass filter was applied to the law data and LED on and off states were detected using local peak detection algorithm. Different neuronal activities at single electrode were separated using K-means clustering algorithm. Optogenetic excitation of neurons were easily visualized by PSTH and raster plot.

Wireless compatibility of suggested optrode has been proven through the development of wireless neural interface. Using nRF24LE1 RF SoC, the system enabled wireless communication between wireless device and a computer through USB wireless dongle. Four channels were designed on the analog front end and the sampling rate of each channel was 16 ksps. The wireless neural interface prototype successfully transmitted $1mV_{pp}$, 1 kHz AC signal to the computer software. Also, neural activities of rodent model have been transmitted wirelessly.

Considering the battery-powered light stimulation method used in the *in-vivo*

experiment and simplicity of the device configuration, fabricated device can potentially be utilized in the wireless optogenetic interface development.

Bibliography

[1] J. P. Seymour, F. Wu, K. D. Wise, and E. Yoon, "State-of-the-art MEMS and microsystem tools for brain research," *Microsystems & Nanoengineering*, vol. 3, no. 1, pp. 1–16, 2017.

[2] K. Deisseroth, G. Feng, A. K. Majewska, G. Miesenböck, A. Ting, and M. J. Schnitzer, "Next-Generation Optical Technologies for Illuminating Genetically Targeted Brain Circuits," *The Journal of Neuroscience*, vol. 26, no. 41, p. 10380, Oct. 2006, doi: 10.1523/JNEUROSCI.3863-06.2006.

[3] K. Deisseroth, "Optogenetics," *Nature Methods*, vol. 8, no. 1, pp. 26–29, 2011, doi: 10.1038/nmeth.f.324.

[4] E. Pastrana, "Optogenetics: controlling cell function with light," *Nature Methods*, vol. 8, no. 1, pp. 24–25, 2011, doi: 10.1038/nmeth.f.323.

[5] E. S. Boyden, F. Zhang, E. Bamberg, G. Nagel, and K. Deisseroth, "Millisecond-timescale, genetically targeted optical control of neural activity," *Nature Neuroscience*, vol. 8, no. 9, pp. 1263–1268, 2005, doi: 10.1038/nn1525.

[6] K. Deisseroth, "Optogenetics," *Nature Methods*, vol. 8, no. 1, pp. 26–29, 2011, doi: 10.1038/nmeth.f.324.

[7] G. Nagel *et al.*, "Channelrhodopsin-2, a directly light-gated cation-selective membrane channel," *Proceedings of the National Academy of Sciences*, vol. 100, no. 24, p. 13940, Nov. 2003, doi: 10.1073/pnas.1936192100.

[8] K. Deisseroth, "Controlling the Brain with Light," *Sci Am*, vol. 303, no. 5, pp. 48–55, 2010, [Online]. Available: http://www.jstor.org/stable/26002255

[9] P. Mahmoudi, H. Veladi, and F. G. Pakdel, "Optogenetics, Tools and Applications in Neurobiology," *J Med Signals Sens*, vol. 7, no. 2, pp. 71–79, 2017, [Online]. Available: https://pubmed.ncbi.nlm.nih.gov/28553579

[10] N. Grossman, V. Simiaki, C. Martinet, C. Toumazou, S. Schultz, and K. Nikolic, "The spatial pattern of light determines the kinetics and modulates backpropagation of optogenetic action potentials," *J Comput Neurosci*, vol. 34, Nov. 2012, doi: 10.1007/s10827-012-0431-7.

[11] E. Stark, T. Koos, and G. Buzsáki, "Diode probes for spatiotemporal optical control of multiple neurons in freely moving animals," *J Neurophysiol*, vol. 108, no. 1, pp. 349–363, 2012.

[12] C. E. Schoonover and A. Rabinowitz, "Control Desk for the Neural Switchboard," *The New York Times*, Manhattan, pp. 1–1, May 17, 2011.

[13] I.-J. Cho, H. W. Baac, and E. Yoon, "A 16-site neural probe integrated with a waveguide for optical stimulation," in *2010 IEEE 23rd*

International Conference on Micro Electro Mechanical Systems (MEMS), 2010, pp. 995–998.

[14] S. Kanno *et al.*, "Multiple optical stimulation to neuron using Si opto-neural probe with multiple optical waveguides and metal-cover for optogenetics," in *2013 35th Annual International Conference of the IEEE Engineering in Medicine and Biology Society (EMBC)*, 2013, pp. 253–256.

[15] H. Shin, S. Kim, N. Choi, H. J. Lee, E.-S. Yoon, and I.-J. Cho, "3D multi-functional neural probe array for mapping functional connectivities in a 3D neuron chip," in *2016 IEEE 29th International Conference on Micro Electro Mechanical Systems (MEMS)*, 2016, pp. 321–324.

[16] F. Wu *et al.*, "An implantable neural probe with monolithically integrated dielectric waveguide and recording electrodes for optogenetics applications," *J Neural Eng*, vol. 10, no. 5, p. 056012, 2013.

[17] Y. Son *et al.*, "In vivo optical modulation of neural signals using monolithically integrated two-dimensional neural probe arrays," *Scientific Reports*, vol. 5, no. 1, p. 15466, 2015, doi: 10.1038/srep15466.

[18] K. Kampasi *et al.*, "Fiberless multicolor neural optoelectrode for in vivo circuit analysis," *Scientific Reports*, vol. 6, no. 1, p. 30961, 2016, doi: 10.1038/srep30961.

[19] M. Schwaerzle, O. Paul, and P. Ruther, "Compact silicon-based optrode with integrated laser diode chips, SU-8 waveguides and platinum electrodes for optogenetic applications," *Journal of Micromechanics and Microengineering*, vol. 27, no. 6, p. 065004, 2017.

[20] H. Shin *et al.*, "Multifunctional multi-shank neural probe for investigating and modulating long-range neural circuits in vivo," *Nature Communications*, vol. 10, no. 1, p. 3777, 2019, doi: 10.1038/s41467-019-11628-5.

[21] L. Wang *et al.*, "An artefact-resist optrode with internal shielding structure for low-noise neural modulation," *Journal of Neural Engineering*, vol. 17, no. 4, p. 046024, 2020.

[22] E. G. R. Kim *et al.*, "3D silicon neural probe with integrated optical fibers for optogenetic modulation," *Lab on a Chip*, vol. 15, no. 14, pp. 2939–2949, 2015.

[23] Y. Son *et al.*, "A new monolithically integrated multi-functional MEMS neural probe for optical stimulation and drug delivery," in *2015 28th IEEE International Conference on Micro Electro Mechanical Systems (MEMS)*, 2015, pp. 158–161.

[24] E. Shim, Y. Chen, S. Masmanidis, and M. Li, "Multisite silicon neural probes with integrated silicon nitride waveguides and gratings for optogenetic applications," *Sci Rep*, vol. 6, no. 1, pp. 1–5, 2016.

[25] K. Kampasi *et al.*, "Dual color optogenetic control of neural populations using low-noise, multishank optoelectrodes," *Microsyst Nanoeng*, vol. 4, no. 1, pp. 1–16, 2018.

[26] S. Libbrecht *et al.*, "Proximal and distal modulation of neural activity

by spatially confined optogenetic activation with an integrated high-density optoelectrode," *Journal of Neurophysiology*, vol. 120, no. 1, pp. 149–161, 2018.

[27] N. McAlinden, E. Gu, M. D. Dawson, S. Sakata, and K. Mathieson, "Optogenetic activation of neocortical neurons in vivo with a sapphire-based micro-scale LED probe," *Front Neural Circuits*, vol. 9, p. 25, 2015.

[28] H. Yasunaga *et al.*, "Development of a neural probe integrated with high-efficiency MicroLEDs for in vivo application," *Japanese Journal of Applied Physics*, vol. 60, no. 1, p. 016503, 2020.

[29] R. Scharf, T. Tsunematsu, N. McAlinden, M. D. Dawson, S. Sakata, and K. Mathieson, "Depth-specific optogenetic control in vivo with a scalable, high-density μLED neural probe," *Sci Rep*, vol. 6, no. 1, pp. 1–10, 2016.

[30] F. Wu, E. Stark, P.-C. Ku, K. D. Wise, G. Buzsáki, and E. Yoon, "Monolithically integrated μLEDs on silicon neural probes for high-resolution optogenetic studies in behaving animals," *Neuron*, vol. 88, no. 6, pp. 1136–1148, 2015.

[31] K. Kim, M. Vöröslakos, J. P. Seymour, K. D. Wise, G. Buzsáki, and E. Yoon, "Artifact-free and high-temporal-resolution in vivo opto-electrophysiology with microLED optoelectrodes," *Nature Communications*, vol. 11, no. 1, p. 2063, 2020, doi: 10.1038/s41467-020-15769-w.

[32] S. Ayub, F. Barz, O. Paul, and P. Ruther, "Heterogeneous 3D optrode with variable spatial resolution for optogenetic stimulation and electrophysiological recording," in *2016 38th Annual International Conference of the IEEE Engineering in Medicine and Biology Society (EMBC)*, 2016, pp. 1762–1765.

[33] B. Fan, K. Y. Kwon, A. J. Weber, and W. Li, "An implantable, miniaturized SU-8 optical probe for optogenetics-based deep brain stimulation," in *2014 36th Annual International Conference of the IEEE Engineering in Medicine and Biology Society*, 2014, pp. 450–453.

[34] K. Kim *et al.*, "GaN-on-Si μLED optoelectrodes for high-spatiotemporal-accuracy optogenetics in freely behaving animals," in *2016 IEEE International Electron Devices Meeting (IEDM)*, 2016, pp. 25–26.

[35] J.-W. Jeong *et al.*, "Wireless optofluidic systems for programmable in vivo pharmacology and optogenetics," *Cell*, vol. 162, no. 3, pp. 662–674, 2015.

[36] R. Scharf, T. Tsunematsu, N. McAlinden, M. D. Dawson, S. Sakata, and K. Mathieson, "Depth-specific optogenetic control in vivo with a scalable, high-density μLED neural probe," *Sci Rep*, vol. 6, no. 1, pp. 1–10, 2016.

[37] K. N. Noh *et al.*, "Miniaturized, battery-free optofluidic systems with potential for wireless pharmacology and optogenetics," *Small*, vol. 14, no. 4, p. 1702479, 2018.

[38] A. E. Mendrela *et al.*, "A high-resolution opto-electrophysiology system with a miniature integrated headstage," *IEEE Trans Biomed*

Circuits Syst, vol. 12, no. 5, pp. 1065–1075, 2018.

[39] Y. Ohta *et al.*, "Micro-LED Array-Based Photo-Stimulation Devices for Optogenetics in Rat and Macaque Monkey Brains," *IEEE Access*, vol. 9, pp. 127937–127949, 2021.

[40] K. Y. Kwon, H.-M. Lee, M. Ghovanloo, A. Weber, and W. Li, "Design, fabrication, and packaging of an integrated, wirelessly-powered optrode array for optogenetics application," *Frontiers in Systems Neuroscience*, vol. 9, 2015, [Online]. Available: https://www.frontiersin.org/article/10.3389/fnsys.2015.00069

[41] J. G. Bernstein, B. D. Allen, A. A. Guerra, and E. S. Boyden, "Processes for design, construction and utilisation of arrays of light-emitting diodes and light-emitting diode-coupled optical fibres for multi-site brain light delivery," *J Eng (Stevenage)*, vol. 2015, p. 10.1049/joe.2014.0304, May 2015, doi: 10.1049/joe.2014.0304.

[42] N. McAlinden *et al.*, "Multisite microLED optrode array for neural interfacing," *Neurophotonics*, vol. 6, no. 3, pp. 1–9, Aug. 2019, doi: 10.1117/1.NPh.6.3.035010.

[43] S. Yoo, H. Lee, S. B. Jun, Y.-K. Kim, and C.-H. Ji, "Disposable MEMS optrode array integrated with single LED for neurostimulation," *Sensors and Actuators A: Physical*, vol. 273, pp. 276–284, 2018.

[44] M. Schwaerzle, O. Paul, and P. Ruther, "Compact silicon-based optrode with integrated laser diode chips, SU-8 waveguides and platinum electrodes for optogenetic applications," *Journal of Micromechanics and Microengineering*, vol. 27, no. 6, p. 065004, 2017, doi: 10.1088/1361-6439/aa6ad4.

[45] Saleh B and Teich MC, "Fundamental of Photonics," *New Jersey: John and Wiley & Sons*, 2007.

[46] J. Sakamoto, T. Hashimoto, H. Kawata, and Y. Hirai, "Single-Mode Polymer Embedded Waveguide for Visible Wavelength using SU-8," *Journal of Photopolymer Science and Technology*, vol. 32, no. 1, pp. 15–19, 2019, doi: 10.2494/photopolymer.32.15.

[47] B. Rubehn, S. B. E. Wolff, P. Tovote, A. Lüthi, and T. Stieglitz, "A polymer-based neural microimplant for optogenetic applications: design and first in vivo study," *Lab on a Chip*, vol. 13, no. 4, pp. 579–588, 2013, doi: 10.1039/C2LC40874K.

[48] K. D. Wise, J. B. Angell, and A. Starr, "An integrated-circuit approach to extracellular microelectrodes," *IEEE transactions on biomedical engineering*, no. 3, pp. 238–247, 1970.

[49] M. W. Varney, D. M. Aslam, A. Janoudi, H.-Y. Chan, and D. H. Wang, "Polycrystalline-diamond MEMS biosensors including neural microelectrode-arrays," *Biosensors (Basel)*, vol. 1, no. 3, pp. 118–133, 2011.

[50] J. Lee, I. Ozden, Y.-K. Song, and A. v Nurmikko, "Transparent intracortical microprobe array for simultaneous spatiotemporal optical stimulation and multichannel electrical recording," *Nat Methods*, vol. 12, no. 12, pp. 1157–1162, 2015.

[51] G. Gabriel *et al.*, "Manufacturing and full characterization of silicon carbide-based multi-sensor micro-probes for biomedical applications,"

Microelectronics Journal, vol. 38, no. 3, pp. 406–415, 2007.
[52] T. D. Y. Kozai *et al.*, "Ultrasmall implantable composite microelectrodes with bioactive surfaces for chronic neural interfaces," *Nat Mater*, vol. 11, no. 12, pp. 1065–1073, 2012.
[53] S. Takeuchi, D. Ziegler, Y. Yoshida, K. Mabuchi, and T. Suzuki, "Parylene flexible neural probes integrated with microfluidic channels," *Lab on a Chip*, vol. 5, no. 5, pp. 519–523, 2005.
[54] J. P. Seymour, N. B. Langhals, D. J. Anderson, and D. R. Kipke, "Novel multi-sided, microelectrode arrays for implantable neural applications," *Biomed Microdevices*, vol. 13, no. 3, pp. 441–451, 2011.
[55] J. Liu, "Syringe injectable electronics," in *Biomimetics Through Nanoelectronics*, Springer, 2018, pp. 65–93.
[56] L. J. Fernández *et al.*, "Study of functional viability of SU-8-based microneedles for neural applications," *Journal of Micromechanics and Microengineering*, vol. 19, no. 2, p. 025007, 2009.
[57] S. Takeuchi, T. Suzuki, K. Mabuchi, and H. Fujita, "3D flexible multichannel neural probe array," *Journal of micromechanics and microengineering*, vol. 14, no. 1, p. 104, 2003.
[58] K. C. Cheung, P. Renaud, H. Tanila, and K. Djupsund, "Flexible polyimide microelectrode array for in vivo recordings and current source density analysis," *Biosensors and Bioelectronics*, vol. 22, no. 8, pp. 1783–1790, 2007.
[59] I. R. Minev *et al.*, "Electronic dura mater for long-term multimodal neural interfaces," *Science (1979)*, vol. 347, no. 6218, pp. 159–163, 2015.
[60] J. Scholvin *et al.*, "Close-Packed Silicon Microelectrodes for Scalable Spatially Oversampled Neural Recording," *IEEE Transactions on Biomedical Engineering*, vol. 63, no. 1, pp. 120–130, 2016, doi: 10.1109/TBME.2015.2406113.
[61] H. S. Jeong, S. Hwang, K. S. Min, and S. B. Jun, "Fabrication of Planar Microelectrode Array Using Laser-Patterned ITO and SU-8," *Micromachines (Basel)*, vol. 12, no. 11, 2021, doi: 10.3390/mi12111347.
[62] S. Shin *et al.*, "High charge storage capacity electrodeposited iridium oxide film on liquid crystal polymer-based neural electrodes," *Sens. Mater*, vol. 28, no. 3, pp. 243–260, 2016.
[63] X. Wang, C. Zhang, G. Szábo, and Q.-Q. Sun, "Distribution of CaMKIIα expression in the brain in vivo, studied by CaMKIIα-GFP mice," *Brain Res*, vol. 1518, pp. 9–25, 2013.
[64] K. P. Giese, N. B. Fedorov, R. K. Filipkowski, and A. J. Silva, "Autophosphorylation at Thr286 of the α calcium-calmodulin kinase II in LTP and learning," *Science (1979)*, vol. 279, no. 5352, pp. 870–873, 1998.
[65] D. J. Poulsen, D. Standing, K. Bullshields, K. Spencer, P. E. Micevych, and A. M. Babcock, "Overexpression of hippocampal Ca2+/calmodulin-dependent protein kinase II improves spatial memory," *Journal of Neuroscience Research*, vol. 85, no. 4, pp. 735–739, 2007.
[66] F. Zeldenrust, W. J. Wadman, and B. Englitz, "Neural coding with

bursts—current state and future perspectives," *Front Comput Neurosci*, vol. 12, p. 48, 2018.

[67] S. T. Lee, P. A. Williams, C. E. Braine, D.-T. Lin, S. W. M. John, and P. P. Irazoqui, "A miniature, fiber-coupled, wireless, deep-brain optogenetic stimulator," *IEEE Transactions on Neural Systems and Rehabilitation Engineering*, vol. 23, no. 4, pp. 655–664, 2015.

[68] Y. Iwai, S. Honda, H. Ozeki, M. Hashimoto, and H. Hirase, "A simple head-mountable LED device for chronic stimulation of optogenetic molecules in freely moving mice," *Neurosci Res*, vol. 70, no. 1, pp. 124–127, 2011.

[69] R. Dagnew *et al.*, "CerebraLux: a low-cost, open-source, wireless probe for optogenetic stimulation," *Neurophotonics*, vol. 4, no. 4, p. 045001, 2017.

[70] G. Gagnon-Turcotte, Y. LeChasseur, C. Bories, Y. Messaddeq, Y. de Koninck, and B. Gosselin, "A wireless headstage for combined optogenetics and multichannel electrophysiological recording," *IEEE Trans Biomed Circuits Syst*, vol. 11, no. 1, pp. 1–14, 2016.

국문 초록

빛을 사용하여 신경세포를 자극하는 광유전학이 수립된 이후, 레이저와 광섬유가 결합된 신경자극 시스템이 빛을 세포에 전달하는 소자로 흔히 사용되고 있다. 하지만, 최근 무선으로 광 자극을 하려는 시도에서 레이저 시스템의 높은 전력소비와 부피가 큰 사이즈는 무선시스템 발전의 장애물이 되고 있다. 이를 해결하기 위해 초소형 발광다이오드를 장착한 실리콘 옵트로드가 각광받고 있으나, 이 또한 광원에서 발생하는 열에 의한 세포손상이 문제가 되고 있다.

본 연구에서는 무선시스템에 호환이 가능하고, 광원에서 발생된 열에 의한 세포 손상을 해결할 수 있는 발광다이오드와 도파관을 결합한 실리콘 옵트로드를 제안한다. 해당 소자가 만들어질 경우 관건은 신경세포 자극을 위한 최소 조도 확보이다. 발광다이오드의 넓은 광 분산 각도와, 광원과 도파관의 낮은 결합효율은 최소 조도 확보를 어렵게 하기 때문에, 이를 해결하기 위해 렌즈를 활용하여 결합효율을 높이고자 한다.

반도체 공정에서 3차원 렌즈를 제작하는 것은 매우 어렵기 때문에, 두 개의 제작가능한 렌즈를 만들어 그 효과를 보완하고자 한다. 실린더 형태의 렌즈와 감광제로 사용되는 다중체 렌즈를 사용하여 수직과 수평방향으로 빛을 모으는 역할을 분담할 수 있다. 실린더 렌즈는 수직으로 빛을 집속하고, 다중체 볼록렌즈는 수평방향으로 빛을

집속한다.

처음으로 실리콘 식각 시 SU-8 투과율이 낮아지는 현상을 보고하였으며, 이는 실리콘 식각 플라즈마로 형성된 자외선에 의해 발생되는 것임을 보고하였다. 낮은 투과율 문제를 회피하기 위해, 공정 순서를 최적화하여 변경하는 방법으로 해결하였다. 실린더 렌즈의 정교한 부착의 경우, 자체적인 정렬 기계를 만들어 해결하였다. 마지막으로 유연한 인쇄회로기판을 소자에 부착하고, 3차원 프린트를 사용하여 소자를 통합했다.

제작된 소자의 광 세기 측정을 한 결과 실린더 렌즈와 SU-8 렌즈의 광 결합효율이 각각 6.7 dB, 6.6 dB 증가하는 것을 확인하였다. 이론적으로 계산한 광효율이 각각 6.1 dB, 7 dB 인 것을 봤을 때, 실린더 렌즈의 측정된 광 효율이 0.6 dB 높은 것을 확인할 수 있었다. 이는 발광다이오드의 넓은 분산각도와 렌즈를 사용한 광선의 높은 기울기로 인해 skew ray가 meridional ray에 비해 훨씬 더 많을 것이라는 가정에 의해 이론이 계산되었기 때문이다. 발광다이오드에 약 50 mA의 전압이 주어졌을 때, 도파관 끝의 조도는 약 2.7 mW/mm^2로 측정되었다. 이를 바탕으로 빛 확산에 의한 전극 위의 조도는 0.5 mW/mm^2 이상이 될 것으로 계산이 되었다.

실리콘 옵트로드는 1x4 어레이 형태로 쉥크가 형성되어 있으며, 각 쉥크마다 4개의 기록전극이 배치되어 있다. 기록전극들은 전극 임피던스를 낮추고 노이즈 대비 높은 신호를 얻기 위해 산화 이리듐을 도금하였다. 임피던스는 기존 2.57 MΩ에서 43.6 kΩ으로 낮아졌다.

제작된 실리콘 옵트로드는 형질전환된 쥐의 해마에 삽입되었다. 기록된 생체신호는 광 자극에 동기화되어 반응하는 것을 측정하였다. 따라서 본 연구에서 고안된 실리콘 옵트로드의 광유전학 사용가능성이 확인되었으며, 옵트로드 장치의 무선시스템의 적용 가능성 또한 증명되었다.